Title

Mechanical Instability in Soft Materials

Author

Liang, Xudong

Publication Date

2018

UNIVERSITY OF CALIFORNIA, SAN DIEGO

Mechanical Instability in Soft Materials

A dissertation submitted in partial satisfaction of the
requirements for the degree
Doctor of Philosophy

in

Engineering Science (Mechanical Engineering)

by

Xudong Liang

Committee in charge:

Professor Shengqiang Cai, Chair
Professor Xanthippi Markenscoff
Professor Robert Sah
Professor Michael Tolley
Professor Sheng Xu

2018

The Dissertation of Xudong Liang is approved, and it is acceptable in quality and form for publication on microfilm and electronically:

Chair

University of California, San Diego

2018

TABLE OF CONTENTS

LIST OF FIGURES

ACKNOWLEDGEMENTS

This work would never have been finished without the supporting from many people. I would like to give my sincere appreciation to all of them.

First and foremost, I would like to give sincere appreciation and bring my heartiest gratitude to my Ph.D. advisor Professor Shengqiang Cai for his guidance and support during my Ph.D. study. In the past five years, I learned a lot from every discussion with Prof. Cai. He has extremely deep understanding in mechanics and always has a magic way to guide me out of the complex mathematics and find out the correct physical explanation. His vision on mechanics and encouragement on developing a clear understanding on the science that I did is a treasure in my career. So, it is with great humbleness and appreciation that I first give thanks to my Ph.D. advisor Professor Shengqiang Cai.

I am also deeply grateful to Professor Xanthippi Markenscoff during my Ph.D. study. I was the teaching assistant in her classes of "Fundamentals of Solid Mechanics". I learned a lot from her classes though I have taken the same course in different universities for several times. I gained a deeper understandings of fundamental concepts in elasticity, like Saint-Venant's principle from her. Prof. Markenscoff is always supportive and inspiring. I enjoyed the discussion with her about my research and she always provides me with valuable suggestions for my academic career. I would like to express gratitude and respect to Professor Xanthippi Markenscoff.

I also want to thank my committee members, Professor Robert Sah, Professor Michael Tolley and Professor Sheng Xu for their suggestions, comments and kind assistances to my research.

I am thankful to Professor Nicholas Boechler and Professor Prabhakar Bandaru for the inspiring and interesting collaborations. Lots of ideas were brought together and achievements were realized through the interactions with them. Prof. Boechler introduced me to the area of high impact in polymer, which is an interesting and unexplored area that is full of new phenomenon. Prof. Bandaru introduced me to the study of photo-active materials, which greatly expand my knowledge in polymer composites. Working with both of you has been a wonderful and enlightening experience, and I look forward to future work together.

I also want to thank my other collaborators. They are Dr. Zhijian Wang, Dr. Maroun Ghanem, Chihyung Ahn, Wei Fan, Qiguang He, Yang Wang, Zichen Zhang, Abhishek Sathisha and Fieyu Tao. Working with you all are interesting and inspiring, and I look forward to collaboration in the future.

I thank all the members in Prof. Cai's group, both past and present members. Lab would be much more boring place without your presence. I also would like to thank the visiting scholars in the group, Professor Kai Li, Professor Hongmiao Tian and Professor Zhongliang Lu. Thanks for sharing all your experiences and providing me the guidance in research.

I am very grateful to the Jacobs fellowship of the Jacobs School of Engineering in UCSD for providing me the opportunity to purse my Ph.D. study in UCSD.

Finally, I would like to give my gratitude to my parents for putting up with me and giving me all the unconditional love and understanding. I am terrible at keeping in touch at a distance, and it is only through your tireless care that I still feel that I have a family.

Chapter 2, in full appears in the paper “Shape Bifurcation of a Spherical Dielectric Elastomer Balloon under the Actions of Internal Pressure and Electric Voltage”, *Journal of Applied Mechanics* 82, no. 10 (2015): 101002, by X. Liang and S. Cai. The dissertation author was the primary investigator and author of this paper.

Chapter 3, in full appears in the paper “New electromechanical instability modes in dielectric elastomer balloons”, *International Journal of Solids and Structures* (2017), by X. Liang and S. Cai. The dissertation author was the primary investigator and author of this paper.

Chapter 4, in full appears in the paper “Creasing of an everted elastomer tube”, *Soft matter* 12, no. 37 (2016): 7726-7730, by X. Liang; F. Tao and S. Cai. The dissertation author was the primary investigator and author of this paper.

Chapter 5, in full appears in the paper “Gravity induced crease-to-wrinkle transition in soft materials”, *Applied Physics Letters*106, no. 4 (2015): 041907, by X. Liang and S. Cai. The dissertation author was the primary investigator and author of this paper.

VITA

2006-2010	B.S. in Theoretical and applied mechanics, Sun Yat-Sen University, China
2010-2013	M.S. in Engineering mechanics, Tsinghua University, China
2013-2018	Ph.D. in Engineering Science (Mechanical Engineering), University of California, San Diego, USA

PUBLICATIONS

1. **X. Liang**, S. Cai, Gravity induced crease-to-wrinkle transition in soft materials, *Applied Physics Letters* 106(4) (2015) 041907.
2. **X. Liang**, S. Cai, Shape bifurcation of a spherical dielectric elastomer balloon under the actions of internal pressure and electric voltage, *Journal of Applied Mechanics* 82(10) (2015) 101002.
3. **X. Liang**, F. Tao, S. Cai, Creasing of an everted elastomer tube, *Soft matter* 12(37) (2016) 7726-7730
4. **X. Liang**, S. Cai, New electromechanical instability modes in dielectric elastomer balloons, *International Journal of Solids and Structures* (2017).
5. **X. Liang**, Z. Zhang, A. Sathisha, S. Cai, P.R. Bandaru, Light induced reversible and irreversible mechanical responses in nanotube-polymer composites, *Composites Part B: Engineering* 134 (2018) 39-45.
6. Y. Jiang, **X. Liang**, M. Guo, Y.P. Cao and S. Cai, Fracture Mechanics Modelling of Popping Event during Daughter Cell Separation, *Biomechanics and modeling in mechanobiology* (2018): 1-7.
7. C. Ahn, **X. Liang**, S. Cai, Inhomogeneous stretch induced patterning of molecular orientation in liquid crystal elastomers, *Extreme Mechanics Letters* 5 (2015) 30-36.
8. Y. Zu, **X. Liang**, J. Du, S. Zhou, C. Yang, Binding of integrin α1 to bone morphogenetic protein receptor IA suggests a novel role of integrin α1β1 in bone morphogenetic protein 2 signalling, *Journal of biomechanics* 48(14) (2015) 3950-3954.

9. Z. Wang, W. Fan, Q. He, Y. Wang, **X. Liang**, S. Cai, A simple and robust way towards reversible mechanochromism: Using liquid crystal elastomer as a mask, *Extreme Mechanics Letters* 11 (2017) 42-48.
10. M. AbiGhanem, **X. Liang**, B. Lydon, L. Potocsnak, T. Wehr, M. Ghanem, S. Cai, and N. Boechler, Wrinkles riding waves in soft layered materials, submitted.

ABSTRACT OF THE DISSERTATION

Mechanical Instability in Soft Materials

by

Xudong Liang

Doctor of Philosophy in Engineering Science (Mechanical Engineering)

University of California, San Diego, 2018

Professor Shengqiang Cai, Chair

We are surrounded by soft materials in a variety of physical and chemical states, which can be easily deformed under external stimuli. When subjected to sufficiently large compression, electric voltage, gravity or impact, soft materials may undergo mechanical instabilities of various types. The instability modes can be either linear or nonlinear, depending on the form of perturbation when the instability set in. When the material is a pressurized dielectric elastomeric film under high voltage, snap-through instability is linear with finite change of volume, while the bulge-out mode is nonlinear with a localized deformation. In terms of surface instability, wrinkles are linear instability mode with undulations finite in space with infinitesimal strain deviating from the smooth state, while creases are localized nonlinear modes with large strain deviating from smooth state. If a soft material is subjected to high speed impact, both the viscoelastic behaviors

of the material and inertial effect are involved, and the mechanical instability is coupled with the wave propagation, finally leading to highly nonlinear instability mode.

We start with the instability analysis of a pressurized dielectric elastomeric film subjected to high voltage. By adopting ideal dielectric elastomer (DE) constitutive model, we show that linear perturbation analysis can capture the shape bifurcation in a spherical DE balloon. However, nonlinear bulge-out shape with a highly localized deformation appears as constraints of the boundaries of the film is applied. A competition between the surface instability modes between the wrinkle and crease is studied in both experiment and theoretical analysis under a deformation mode called eversion, and crease is shown to form prior to wrinkle with lower critical strain to set in. A transition between the wrinkle and crease instability happens when gravity becomes important. We measure the dynamics of soft elastomeric blocks with stiff surface films subjected to high-speed impact, and observe wrinkles forming along with, and riding upon, waves propagating through the system.

Chapter 1 Introduction

1.1 Mechanical instability in Soft materials

We are surrounded by soft materials in a variety of physical and chemical states, which can be easily deformed under external stimuli. Soft materials prevail in the animal world [1], which are essential for the living beings to adapt to the fast changing and complex natural environments. A vast majority of the animals are fully soft-bodied without stiff skeletons [2], including animals like jellyfish, inchworms, octopus [3] (Fig. 1.1a-c). Even animals with stiff exoskeletons (e.g. insects) or endoskeletons (e.g. human) are either spending a long-lived lifetime stages with a completely soft body (maggots, grubs, and caterpillars) or are mainly composted of soft tissues. For example, the human skeleton typically contributes only 11% of the body mass of an adult male, whereas soft muscle contributes an average 42% of body mass [1].

In the engineering applications, the recent rapid developments in soft materials have inspired a new wave of researches that aims at using soft materials in the complex environments and handling the unexpected interactions with human [1, 4-8]. Soft robotics [4-6, 9-13] built with soft materials permit more adaptive and flexible interactions than traditional robots composed of rigid materials like alloys, metals and magnets. (Fig. 1.1d). The application of soft materials in electronics [14-17] is revolutionizing the traditional stiff, silicon-based electronic circuits and transforming them into a more conformable, biodegradable system (Fig. 1.1e). Soft materials also open up new prospects for bioengineered and biohybrid devices [7, 8, 18-20], by interfacing living cells with highly organized, stimuli-responsive soft materials that are able to mimic the natural living systems (Fig. 1.1f).

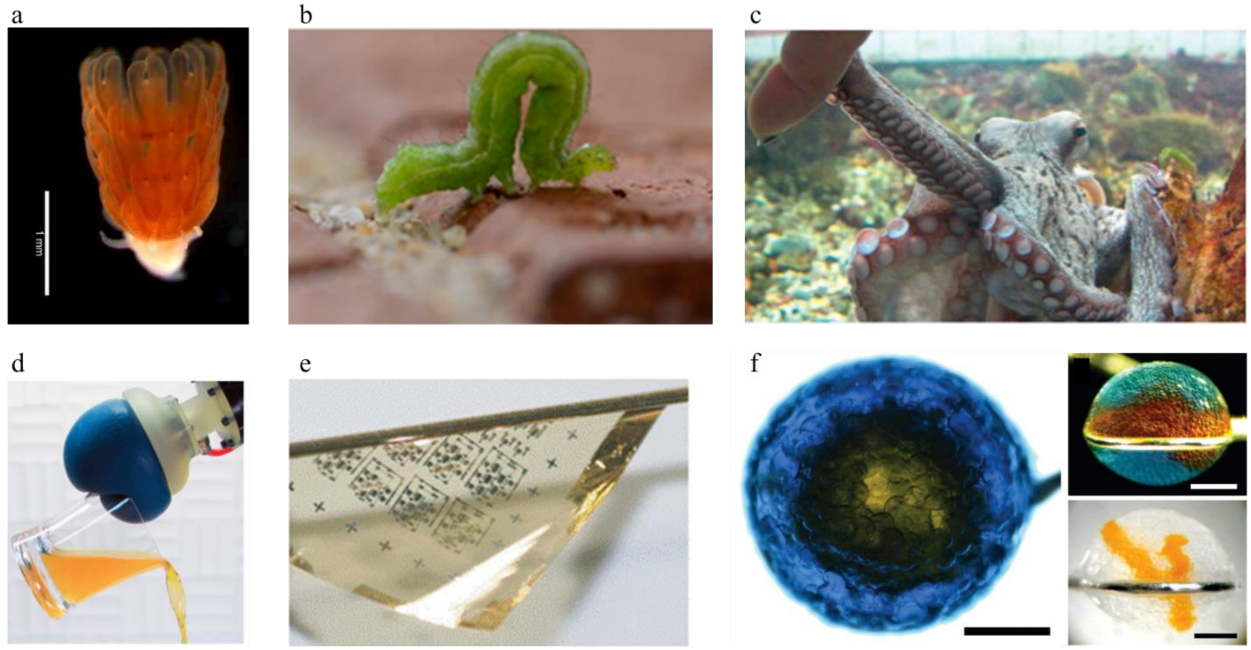

Figure 1.1: Soft materials in nature and engineering applications. They are major components in animals of (a) jellyfish [3], (b) inchworm and (c) octopus [1], in engineering applications of (d) soft robotics [1], (e) soft electronics [21] and (f) 3D printing soft tissues [20].

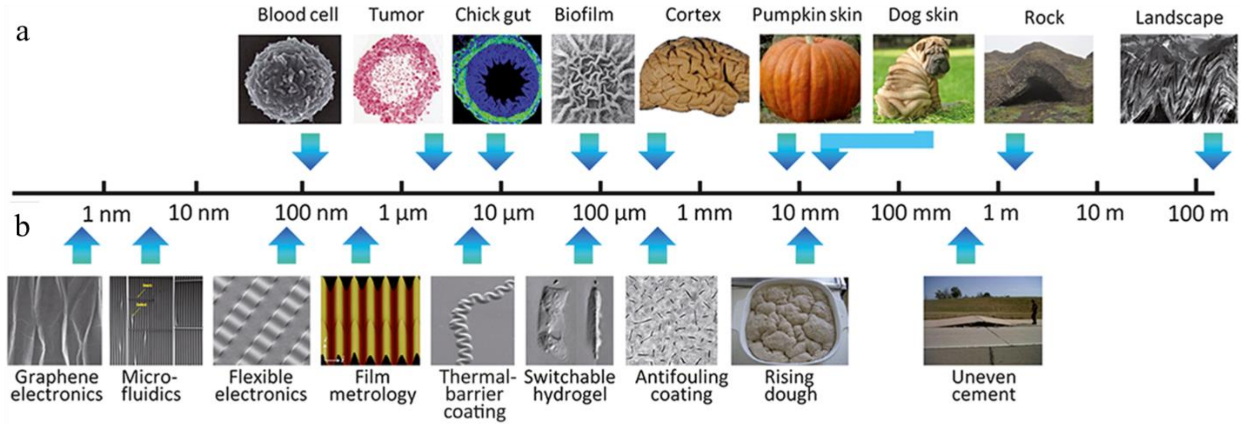

Figure 1.2: Mechanical instability in soft materials in nature (a) and in engineering applications (b) across multiple length scales [22].

Recent progress in soft technologies embodied in different areas have greatly inspired the researches of the mechanics of soft materials [23-40]. Compared to the traditional materials, the outstanding capacities of undergoing large deformation and multiple-field actuations in soft materials endorse them great advantages in engineering applications. However, great challenges, like the mechanical instability of soft materials, are also met during their applications [41, 42]. Different types of mechanical instabilities have been identified in both natural and engineering systems, from nano- to macro scale as shown in Fig. 1.2 [22]. Mechanical instabilities can occur at the surface or interior of soft materials, form due to various loadings, such as compression or eversion and are induced by multiple external fields, like gravity force or electrical field. The mechanical instabilities phenomenon not only manifest the beauty of nature [43, 44], being critical to the survival and well-being of the living organisms [45-52], but also have recently been harnessed to give tunable topographic features in engineered systems [53-58].

This dissertation studies the mechanical instability in soft materials under various loading conditions and interactions with multiple fields. Soft materials are usually much more deformable than the stiff materials and highly sensitive to the external stimuli, making them accessible to new and various modes of instabilities easily. The mechanical instability can be either linear or nonlinear, depending on the form of the perturbations when the instabilities set in. The wrinkle and the snap-through instability have been identified for a long time via linear stability analysis, while the crease and the localized bulge-out instability are highly nonlinear, which were recently identified experimentally. The following sections provide an introduction to both the linear and nonlinear analysis of the mechanical instabilities.

1.2 Linear analysis of mechanical instability

The linear mechanical instability mode is an equilibrium state predicted via linearization of the complex incremental deformation in the neighborhood of a known equilibrium state [59-61]. For example, wrinkle is assumed to be a periodic undulation with infinitesimal strain deviating from a smooth state (Fig. 1.3a) [62-65]. Therefore, by assuming an incremental periodic deformation over the smooth state is also an equilibrium state, the linear perturbation analysis is able to predict the critical loadings and wavelength of the wrinkle instability. The linear perturbation analysis formulates an incremental boundary value problem with the smooth state as a reference state, and the onset of wrinkles corresponds to the non-trivial solution to the incremental boundary value problem, which is an eigenvalue problem [61, 62]. The smallest eigenvalue is the critical loading for the onset of the mechanical instability, while the correspondent eigenvector represents the wrinkle wavelength. Such a instability is also known as a bifurcation instability, with multiple equilibrium states that exists in a neighborhood of a known equilibrium state (Fig. 3b) [66]. Biot has used this method to study the surface instability of a hyperelastic half space and interfacial instability of two hyperelastic half spaces [67, 68]. Ogden further studied the problem of the incremental deformation superposed on an underlying finite deformation [61]. By considering the thin film as a von Karman plate under the assumption that the film thickness is much smaller than wavelength of wrinkles and modeling both the film and substrate as linear elastic materials, people further developed nonlinear theories of wrinkles, which can not only predict the initiation of wrinkles, but also study the growth of the amplitude of the wrinkles under small strains [69-77].

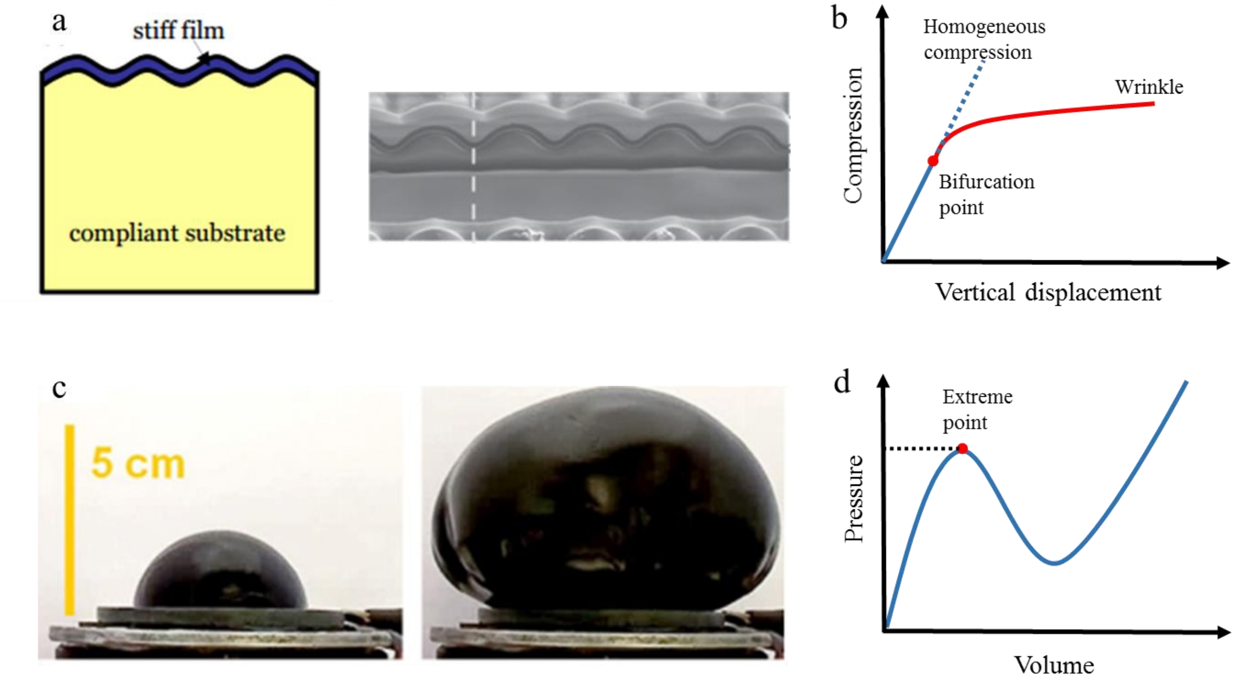

Figure 1.3: Linear mode of mechanical instability in soft materials. (a) Wrinkle instability in film-substrate system [78]. (b) Phase diagram of the bifurcation instability. (c) Snap-through instability in balloon structure [79]. (d) Phase diagram of the limit point instability.

The snap-through instability in a pressurized elastomeric balloon represents a different type of linear mechanical instability mode in soft materials [80-89]. Instead of bifurcating from an equilibrium state with infinitesimal deformation, finite deformation is found when the mechanical instability happens at the extreme points of loadings (Fig. 1.3c) [80, 82-84]. The snap-through instability is also known as the ‘limit-point’ instability [66]. For example, when an elastomeric balloon is pressurized, it is difficult to inflate at first, and then its radius may increase dramatically and rapidly, with little or no effort to produce after the snap-through instability (Fig. 1.3d). Although the deformation is finite, the linearized incremental deformation is proved to be able to capture the deformation during the snap-through instability. The linear mechanical instability predicted through linear perturbation analysis are widely adopted to explain the snap-though phenomenon observed experimentally in elastomeric balloon [80, 83, 84]. Gent was first one to relate the snap-through instability with the stiffening in rubber-like material [90]. Ben Amar further studied the inflation jump instability for the development and rupture of intracranial aneurysms [91]. Suo *et. al* recently has recently achieved a giant voltage-induced deformation with area expansion by 1692% by placing a dielectric elastomer membrane near the verge of the snap-through instability, triggered the instability with voltage and bent the snap-through path to avert electric breakdown. [79, 92].

1.3 Nonlinear analysis of mechanical instability

The theoretical analyses carried out by Biot about five decades ago predicted that the surface of an incompressible neo-Hookean elastic material would become unstable, where a sinusoidal wave was formed when a compressive strain of 0.46 was applied to the free surface under a plane strain condition [67, 68]. However, Biot's prediction of smooth wavy surface instability in a large block of elastomeric material has not been observed experimentally. Instead of forming wrinkles, creases have been observed routinely on elastic blocks under compression [93, 94]. Gent and Cho observed a sharp crease occurred on the surface with a compression strain of 0.35 when bending a rubber blocks [93]. Ghatak and Lal Das further showed that crease was an elastic response of material, which resulted in extreme localization of curvature and was mediated by dual effects of local defects and inter- and intramolecular interactions [94]. Hohlfeld and Mahadevan [49] used numerical methods to simulate the formation of crease and showed that it was a scale-free, subcritical nonlinear mechanical instability different from Biot's solution. The numerical method was further explored by Hong [95] and Cai [96-98], who discovered that the critical strain for the onset of creases was 0.35, which agrees well with the experimental observation of Gent and Cho [93].

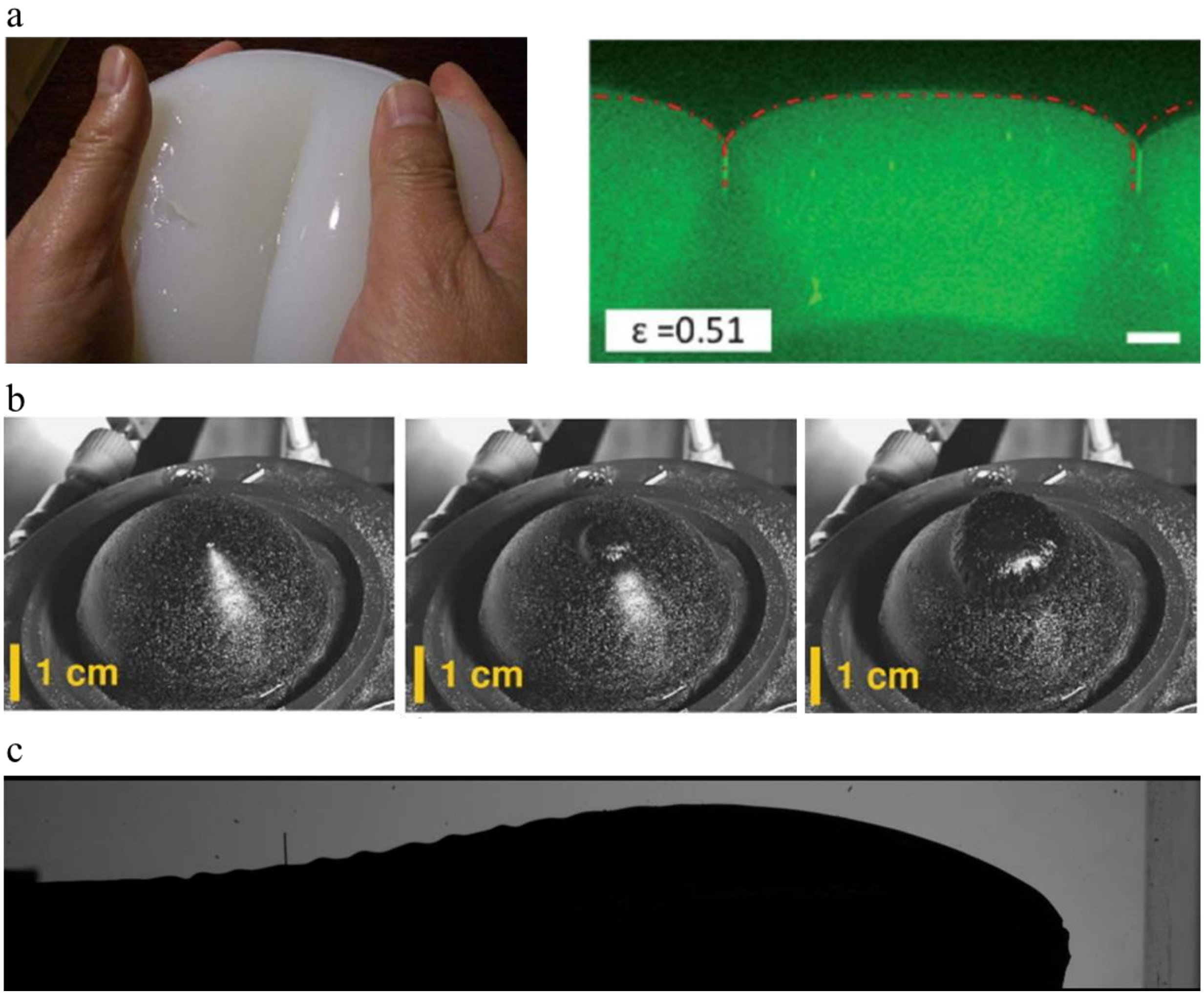

Figure 1.4: Nonlinear instability mode in soft materials. (a) Crease of Liangfen (a starch gel) due to bending (left) [95], and cross-section view of creases (right) [98]. (b) Localized bulge-out in planar balloon under electric field [79]. (c) Dynamic wrinkle formation under high speed impact (courtesy of Prof. Nicolas Boechler).

The difference is due to the fact that Biot linearized the boundary value problem around a state of finite deformation with a linear incremental deformation, and predicted the solution of a smooth, wavy surface of infinitesimal strain deviated from the surface. By contrast, crease nucleates at a point with an upper critical strain and is an essential singularity out of the linearized spectrum [49, 95]. Creasing and wrinkling instability are two distinct surface instability modes characterized by localized singular folds and continuous smooth undulations, respectively. The sharp localized crease tip, and the self-contact cross-section of crease (Fig. 1.4a) is very different from a wrinkle [98]. Recent researches on creases have shown that the strain for the onset of creases cannot be predicted by linear perturbation analysis [49, 95-98]. Instead, a combination of numerical calculations and energetic analysis, adopted in the previous studies [49, 95, 98], precisely predicted the strain for the onset of the crease.

Nonlinear mechanical instability also appears when soft materials are stimulated by external fields [99-101]. For example, when a dielectric elastomer membrane is loaded with both internal pressure and electric voltage, in addition to the linear instability mode of snap-through instability, an unusual deformation of the dielectric elastomer membrane with a localized bulge-out that expand significantly more than its neighboring area emerges as a nonlinear mechanical instability mode as shown in Fig. 1.4b [79]. The localized bulge-out instability mode is different from the snap-through instability mode predicted from linear perturbation analysis, as the highly localized and nonlinear deformation cannot be captured by solving the linearized incremental boundary value problem [99]. Nonlinear field theory for elastic dielectric accounting for the coupling between mechanics and electricity was originally proposed by Toupin [102]. Relevant studies of elastic dielectric were further developed by Landau and Lifshitz [103], Eringen [104] and Tiersten [105]. The theory has been re-examined in recent years due to the rapidly growing applications of dielectric elastomer. Constitutive models of dielectric elastomer accounting for large deformation have been developed to explain diverse experimental observations and also provide guidelines for designing new dielectric elastomer devices [26, 27, 106].

In addition, the dynamic loading can also lead to a nonlinear mechanical instability in soft materials [107-110]. When a soft elastomer block containing a stiff surface film that is subjected to high speed plate impact, the impact launches a large deformation, high strain rate compression wave that induced localized surface wrinkle formation as a result of elastic surface instabilities [108, 109]. Such dynamically evolving morphologies of surface instability resemble wrinkle "ride" the wave propagation through the substrate as shown in Fig. 4c. While the quasi-static wrinkling commonly observed in a stiff film over soft substrates and successfully predicted via linear perturbation analysis, wherein inertial effects are ignored, the dynamic formation and propagation of such surface wrinkle subjected to high-speed impact can be highly nonlinear and cannot be predicted through linearized stability analysis. The viscoelastic behaviors of the soft elastomers under high speed impact and the wrinkles formation alongside with the wave propagation through the substrate induce the nonlinear mechanical instability mode. Recent studies of mechanical instability in soft materials have explored the dynamics of viscoelastic matrices subject to dynamic loadings [111, 112]. In contexts directly related to wrinkling of stiff films on viscoleastomeric bases, recent studies have also theoretically explored the dynamics of wrinkle growth and coarsening, as well as experimentally studied the slow dynamic growth and reorganization of folds under biaxial compression, slip dynamics of ripple dislocation, and evaporation driven wrinkle growth [113-115].

1.4 Outline of this dissertation

This dissertation studies mechanical instability in soft materials under different loading conditions and interactions with multiple fields. In Chapter 2, we study the deformation of a dielectric elastomeric balloon under the action of an internal pressure and an electric voltage. A linear perturbation method is adopted to predict the linear mechanical instability mode of the dielectric elastomeric balloon under homogeneous deformation. In Chapter 3, we perform numerical simulations to examine the nonlinear mechanical instability mode of a dielectric elastomeric balloon under inhomogeneous deformation. In Chapter 4, we studied the instability of elastomeric tube under a finite deformation of eversion. The nonlinear mechanical instability mode of crease is shown to form prior to the formation of wrinkle instability. In Chapter 5, we study the effect of gravity (body force) in the transition between the mechanical instabilities of crease and wrinkle. The conditions for the transition between the wrinkling and creasing instability are determined. Chapter 6 concludes the study in this dissertation.

Chapter 2 Shape Bifurcation of a Spherical Dielectric Elastomer Balloon under the Actions of Internal Pressure and Electric Voltage

Under the actions of internal pressure and electric voltage, a spherical dielectric elastomer balloon usually keeps a sphere during its deformation, which has also been assumed in many previous studies. In this article, using linear perturbation analysis, we demonstrate that a spherical dielectric elastomer balloon may bifurcate to a non-spherical shape under certain electromechanical loading conditions. We also show that with a non-spherical shape, the dielectric elastomer balloon may have highly inhomogeneous electric field and stress/stretch distributions, which can lead to the failure of the system. In addition, we conduct stability analysis of the dielectric elastomer balloon in different equilibrium configurations by evaluating its second variation of free energy under arbitrary perturbations. Our analyses indicate that under pressure-control and voltage-control mode, non-spherical deformation of the dielectric elastomer balloon is energetically unstable. However, under charge-control or ideal gas mass-control mode, non-spherical deformation of the balloon is energetically stable.

2.1 Introduction

A soft dielectric membrane can deform by mechanical stretching or applying electric voltage across its thickness. Experiments are abundant showing the interplay between electric field and mechanics in dielectric elastomers [116-119]. For instance, voltage-induced deformation in a free standing dielectric elastomer membrane can hardly exceed 40% due to electromechanical pull-in instability [120], while a prestretched dielectric elastomer membrane or the membrane subjected to a dead load can deform as large as several hundred percent by voltage without failure [79, 121].

Due to the electromechanical coupling, high energy density, easy fabrication and relatively low cost, dielectric elastomers have been recently explored intensively in diverse applications, including artificial muscles [122-125], haptic devices [126, 127], micro-pumps [128-131] and adaptive lens[132-135] to name a few. Among all dielectric elastomer devices, spherical balloon is one of the most frequently used geometries. For example, dielectric elastomer balloons have been proposed to make reciprocating or peristaltic pumps by Goulbourne [129, 130]. Dielectric elastomer balloons have also been developed into tactile devices [4] and spherical actuators and generators.

The wide applications of dielectric elastomer balloon have motivated recent studies of their deformation under different electromechanical loading conditions. Zhu et al. [117] formulated nonlinear vibrations of a spherical dielectric elastomer balloon subjected to a constant internal pressure and an AC voltage. Rudykh et al. [136] predicted snap-through actuation of a thick-walled dielectric elastomer balloon. Li et al. [79] successfully harnessed electromechanical instabilities of a dielectric elastomer balloon to achieve giant voltage-induced expansion of area.

While the deformation of a dielectric elastomer balloon subjected to a voltage and internal pressure has been intensively studied, in most previous studies, spherical deformation is assumed if the dielectric elastomer balloon is initially a sphere. Little efforts have been made, if any, in studying possible non-spherical deformation in a spherical dielectric elastomer balloon subjected to electromechanical loading. However, on the other hand, non-spherical shape bifurcation has been observed in experiments and predicted in theories for a spherical elastomer balloon only subjected to internal pressure. For example, Alexander [80] has reported the observation of non-spherical deformation mode in a neoprene spherical balloon in the inflation process. Linear perturbation analyses, conducted by different researchers [81, 83, 137], predicted the existence of non-spherical deformation mode in a spherical elastomer balloon subjected to internal pressure. Moreover, Fu et al. [84] have recently conducted stability analyses on the non-spherical deformation mode and shown that in certain loading conditions, the non-spherical configuration of the balloon can be stable.

Additionally, in the experiments conducted by Li et al. [79], a region on the top of the dielectric elastomer balloon bulged out significantly when the voltage was high. This phenomenon cannot be predicted by their theoretical model. This experimental observation, combined with the previous studies of the elastomer balloon only subjected to internal pressure, indicates the possible shape bifurcation of dielectric elastomer balloon subjected to a combination of internal pressure and electric voltage. In this article, we study the shape bifurcation in a spherical dielectric elastomer balloon subjected to internal pressure and electric voltage. We will also conduct stability analyses for different modes of deformation under different electromechanical loading conditions.

The chapter is organized as follows. Section 2 derives the field equations of a spherical balloon subject to internal pressure and electric voltage. Section 3 describes the homogeneous deformation solution of the balloon. We conduct linear perturbation analyses in Section 4 and calculate inhomogeneous deformation of the balloon in Section 5. Finally, in section 6, we conduct stability analyses on different deformation mode of the dielectric elastomer balloon.

2.2 Axisymmetric deformation of a spherical dielectric elastomer balloon subjected to internal pressure and electric voltage

We investigate the deformation of a spherical balloon made by a dielectric elastomer under the actions of internal pressure p and electric potential φ, as shown in Fig. 2.1a. The radius of the balloon in the undeformed state is assumed to be R. We assume the deformation of the balloon is axisymmetric. A Cartesian coordinate x-z is introduced, with the origin located at the center of the undeformed balloon, to describe the deformation (Fig. 2.1b). The coordinates of a material point A in the undeformed state can be written as,

$$X = R\sin\theta, \tag{2.1}$$

$$Z = -R\cos\theta. \tag{2.2}$$

After deformation, as shown in Fig.1b, point A moves to A' with the coordinate,

$$x = x(\theta),\ z = z(\theta). \tag{2.3}$$

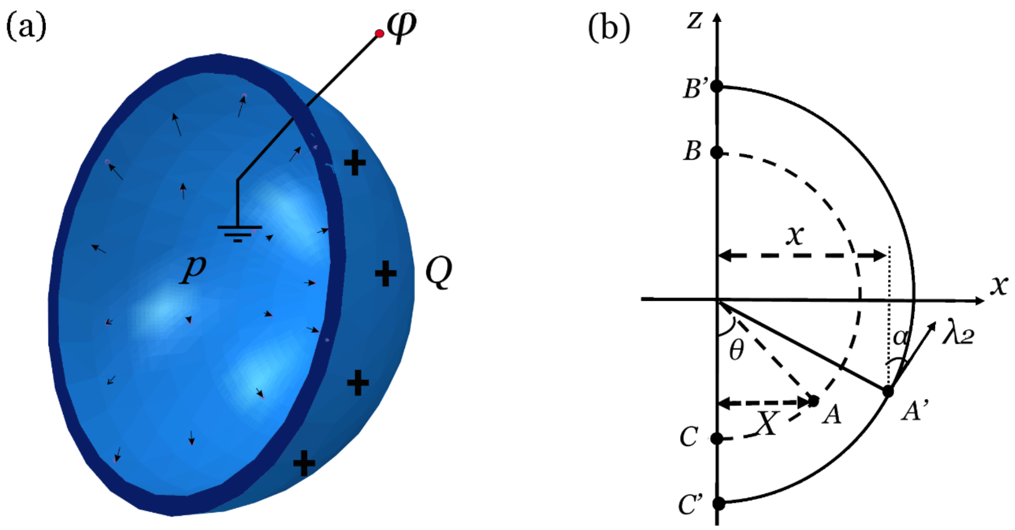

Figure 2.1: (a) Schematics of a dielectric elastomer balloon subjected to internal pressure and electric voltage. (b) The balloon with axisymmetric deformation. Dash line represents the undeformed spherical balloon and solid line represents shape of the balloon after deformation.

Let λ_1 and λ_2 denote the principle stretches of the membrane in the latitudinal direction and the longitudinal direction, so we have

$$\lambda_1 = x / X, \tag{2.4}$$

$$\lambda_2 = \frac{1}{R}\sqrt{\left(\frac{dx}{d\theta}\right)^2 + \left(\frac{dz}{d\theta}\right)^2}. \tag{2.5}$$

The force balance in the z direction and the direction normal to the z axis of the balloon can be written as,

$$2S_2 H \sin\theta \frac{dz}{d\theta} = p\lambda_2 x^2, \tag{2.6}$$

$$S_1 \frac{dx}{d\theta} = R\lambda_2 \frac{d}{d\theta}\left(S_2 \sin\theta\right), \tag{2.7}$$

where S_1 and S_2 are the nominal stresses in latitudinal direction and longitudinal direction, H is the thickness of the balloon in undeformed state, which is a constant. Using the definition of λ_1 and λ_2, and the geometrical relationship $dx/d\theta=R\lambda_2 sin\alpha$ and $dz/d\theta=R\lambda_2 cos\alpha$, where α is the angle between the tangential direction of the deformed balloon and the z axis (Fig. 2.1b), the force balance equations (2.6) and (2.7) can be rewritten as,

$$\frac{d\lambda_1}{d\theta}=\lambda_2\frac{\sin\alpha}{\sin\theta}-\lambda_1\cot\theta, \tag{2.8}$$

$$\frac{d\lambda_2}{d\theta}=\left(S_1-\lambda_2\frac{\partial S_2}{\partial\lambda_1}\right)\left(\frac{\partial S_2}{\partial\lambda_2}\right)^{-1}\frac{\sin\alpha}{\sin\theta}-\left(S_2-\lambda_1\frac{\partial S_2}{\partial\lambda_1}\right)\left(\frac{\partial S_2}{\partial\lambda_2}\right)^{-1}\cot\theta, \tag{2.9}$$

$$\frac{d\alpha}{d\theta}=\frac{S_1\cos\alpha}{S_2\sin\theta}-\frac{p\lambda_1\lambda_2R}{S_2H}. \tag{2.10}$$

The elastomer is assumed to be incompressible, namely,

$$\lambda_1\lambda_2\lambda_3=1, \tag{2.11}$$

where λ_3 is the stretch in the thickness direction of the membrane.

Constitutive model of ideal dielectric elastomer is adopted here to describe the electromechanical behaviors of the balloon membrane [120]. The electric field E and the electric displacement D is related by the linear equation,

$$D=\varepsilon E, \tag{2.12}$$

where ε is permittivity of the elastomer, independent of the deformation and electric field. The electric field in the membrane can be calculated by $E=\varphi/h$, where φ is the electric potential difference between the two surfaces of the membrane and h is the thickness of the membrane in the deformed state which may vary from point to point. The electric displacement is equal to the charge density, namely, $D=\mathrm{d}Q/\mathrm{d}a$, where d$a$ is the area of an element of the membrane in deformed state and dQ is the amount of charge on each side of the element.

The relation between the nominal stresses and the stretches are,

$$S_1 = \frac{\partial W_s(\lambda_1,\lambda_2)}{\partial \lambda_1} - \frac{\varepsilon E^2}{\lambda_1}, \tag{2.13}$$

$$S_2 = \frac{\partial W_s(\lambda_1,\lambda_2)}{\partial \lambda_2} - \frac{\varepsilon E^2}{\lambda_2}, \tag{2.14}$$

where the first terms in both equations are elastic stress and the second terms are Maxwell stress. $W_s(\lambda_1, \lambda_2)$ is the stretching free energy of the elastomer, for which we adopt Ogden model [138],

$$W_s(\lambda_1,\lambda_2) = \sum_{r=1}^{3} \frac{\mu\mu_r}{\alpha_r}\left(\lambda_1^{\alpha_r} + \lambda_2^{\alpha_r} + (\lambda_1\lambda_2)^{-\alpha_r} - 3\right), \tag{2.15}$$

where μ is the shear modulus for infinitesimal deformation, α_r and μ_r are the material constants. In this article, we use the following material parameters: α_1=1.3, α_2=5.0, α_3=-2.0 and μ_1=1.491, μ_2=0.003, μ_3=-0.023. Inserting Eq. (2.15) into Eqs. (2.13) and (2.14), we obtain that

$$S_1 = \sum_{r=1}^{3} \mu\mu_r \left(\lambda_1^{\alpha_r - 1} - \frac{1}{\lambda_1^{\alpha_r+1}\lambda_2^{\alpha_r}} \right) - \frac{\varepsilon E^2}{\lambda_1}, \tag{2.16}$$

$$S_2=\sum_{r=1}^{3}\mu\mu_r\left(\lambda_2^{\alpha_r-1}-\frac{1}{\lambda_1^{\alpha_r}\lambda_2^{\alpha_r+1}}\right)-\frac{\varepsilon E^2}{\lambda_2}. \tag{2.17}$$

In the southern and northern poles of the balloon, we have the following boundary conditions:

$$\lambda_1(0)=\lambda_2(0), \tag{2.18}$$

$$\lambda_1(\pi)=\lambda_2(\pi), \tag{2.19}$$

$$\alpha(0)=\frac{\pi}{2},\ \alpha(\pi)=-\frac{\pi}{2}. \tag{2.20}$$

Using constitutive Eqs. (2.12), (2.16) and (2.17), the right hand side of the Eqs. (2.8)~ (2.10) can be expressed as functions of $\lambda_1(\theta)$, $\lambda_2(\theta)$ and $\alpha(\theta)$. Together with the boundary conditions (2.18)~(2.20), the deformation of the dielectric elastomer balloon under different eletromechanical loadings can be calculated.

2.3 Homogeneous deformation

Apparently, homogeneous deformation of the spherical balloon is a solution to the equations in sec.2, i.e,

$$\lambda_1=\lambda_2=\lambda_0, \tag{2.21}$$

$$S_1=S_2=S_0, \tag{2.22}$$

$$E = E_0. \tag{2.23}$$

The value λ_0, S_0 and E_0 depend on the loading conditions, namely, the magnitude of electric potential φ and internal pressure p. Because the deformation in the balloon is homogeneous, the electric field and stress in the balloon are also homogeneous. As a consequence, a combination of Eqs. (2.8)~(2.10) results in a single nonlinear algebra equation for determining stretch λ_0:

$$\frac{pR}{\mu H}\lambda_0^2 + 2\left(\frac{\varphi}{H\sqrt{\mu/\varepsilon}}\right)^2 \lambda_0^3 - 2\sum_{r=1}^{3}\mu_r(\lambda_0^{\alpha_r-1} - \lambda_0^{-2\alpha_r-1}) = 0, \tag{2.24}$$

where $pR/\mu H$ is the dimensionless pressure and $\varphi/\left(H\sqrt{\mu/\varepsilon}\right)$ is the dimensionless electric potential. With knowing the homogenous stretch λ_0, the volume of the balloon can be easily calculated. Fig. 2.2 plots the volume of the balloon as a function of internal pressure for three different electric voltages. All the three *p-V* curves have a N shape, which are consistent with the results reported previously [84, 137]. Due to the N shaped *p-V* curve, it is known that under pressure control, snap through instability in the balloon can happen when the pressure exceeds the peak value in the *p-V* curve.

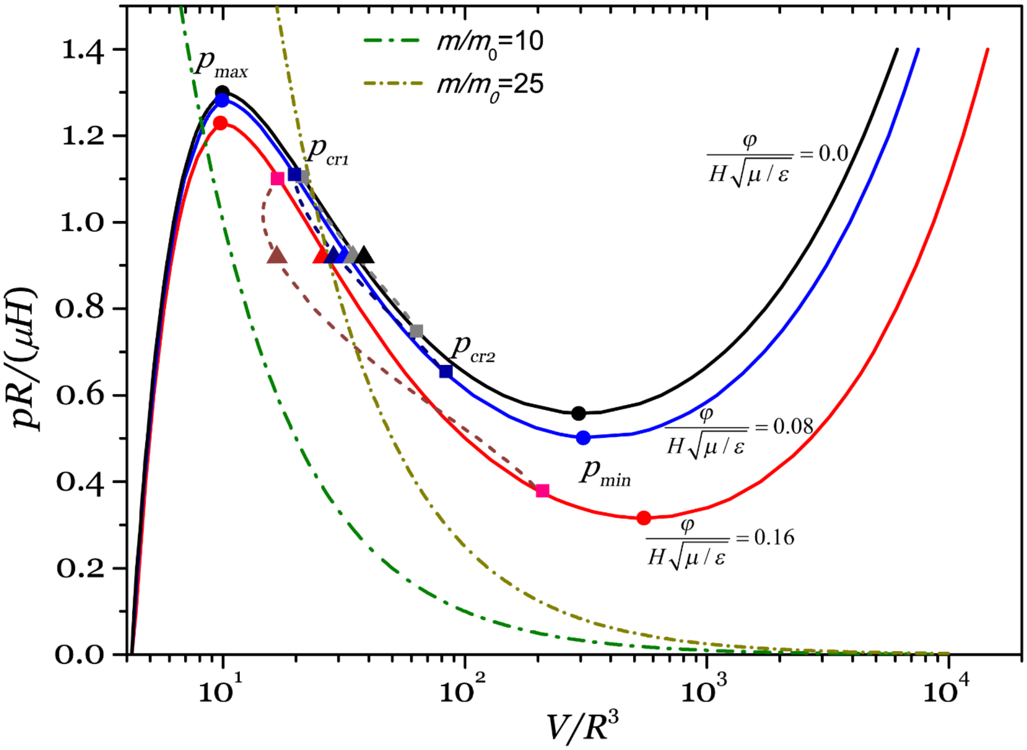

Figure 2.2: The pressure-volume (p-V) relation of a spherical dielectric elastomer balloon subjected to three different voltages. During the deformation, the balloon may keep a sphere which is represented by the solid curves or become non-spherical which is represented by dash curves. The circle and square dots stand for the bifurcation points predicted from the linear perturbation analysis for spherical and pear-shaped mode respectively. Two adjacent deformation modes with pressure of $pR/(\mu H)=0.9$ and three different voltages are marked by triangles. The dash-dot lines represent ideal gas law for two different mass of ideal gas, where m_0 is the mass of gas molecules when pressure and volume are unity.

2.4 Linear perturbation analysis

With homogeneous deformation, the dielectric elastomer balloon keeps spherical shape. However, as discussed in the introduction, non-spherical deformation in the balloon may also happen. We next conduct linear perturbation analysis to investigate the dielectric elastomer balloon bifurcating from spherical deformation to non-spherical deformation.

Linear perturbation is performed on the state of homogeneous deformation with equal-biaxial stretches λ_0. The radial and tangential displacement perturbation $\delta_r(\theta)$ and $\delta_t(\theta)$ are assumed to be axisymmetric. So, the coordinates of any material point after perturbation can be written as,

$$x(\theta) = \lambda_0 R \sin\theta + \delta_r(\theta)\sin\theta + \delta_t(\theta)\cos\theta, \tag{2.25}$$

$$z(\theta) = -\lambda_0 R \cos\theta - \delta_r(\theta)\cos\theta + \delta_t(\theta)\sin\theta. \tag{2.26}$$

Generally speaking, the perturbations of the displacement may result in perturbations of stretches $\delta\lambda_1$ and $\delta\lambda_2$, the nominal stresses δS_1 and δS_2 and the internal pressure δp. Consequently, the force balance equations (2.6) and (2.7) can be rewritten as,

$$2H(S_2^0 + \delta S_2)\left(\frac{dz^0}{d\theta} + \frac{d\delta z}{d\theta}\right)\sin\theta = (p^0 + \delta p)(\lambda_2^0 + \delta\lambda_2)(x^0 + \delta x)^2, \tag{2.27}$$

$$(S_1^0 + \delta S_1)\left(\frac{dx^0}{d\theta} + \frac{d\delta x}{d\theta}\right) = R(\lambda_2^0 + \delta\lambda_2)\frac{d}{d\theta}\Big((S_2^0 + \delta S_2)\sin\theta\Big), \tag{2.28}$$

The upper index "0" represents the variables in the homogeneous deformation state. All the perturbations in Eqs. (2.27) and (2.28) can be expressed by power series of $\delta_r(\theta)$ and $\delta_t(\theta)$. To investigate the critical conditions of the bifurcation, we only keep the linear order terms of $\delta_r(\theta)$ and $\delta_t(\theta)$. Finally, we obtain the following eigenvalue equation of δ_r,

$$\begin{aligned}&\lambda_0 S_1^0 \frac{\partial S_1^0}{\partial\lambda_1}\left((1-t^2)\frac{d^2\delta_r}{dt^2} - 2t\frac{d\delta_r}{dt}\right) + \left(S_1^0 + \lambda_0\frac{\partial S_1^0}{\partial\lambda_1} - \lambda_0\frac{\partial S_1^0}{\partial\lambda_2}\right)\left(2S_1^0 - \lambda_0\frac{\partial S_1^0}{\partial\lambda_1} - \lambda_0\frac{\partial S_1^0}{\partial\lambda_2}\right)\\ &= C\left(S_1^0 - \lambda_0\frac{\partial S_1^0}{\partial\lambda_1} - \lambda_0\frac{\partial S_1^0}{\partial\lambda_2}\right)t - \frac{\pi R^4\lambda_0^5}{H}\frac{\partial p}{\partial V}\left(S_1^0 + \lambda_0\frac{\partial S_1^0}{\partial\lambda_1} - \lambda_0\frac{\partial S_1^0}{\partial\lambda_2}\right)\int_{-1}^{1}\delta_r dt,\end{aligned} \tag{2.29}$$

where t=cosθ, C is a constant of the integration [83], and R is the radius of the balloon in the reference state. Boundary conditions for δ_r are $\delta'_r(0)=0$ and $\delta'_r(\pi)=0$. Under pressure-control mode, the last term in Eq. (2.29) is zero. Eq. (2.29) is consistent with the equation given in [83, 86], and it is also known as the Legendre's equation and the bounded solution is,

$$\delta_r(t) = DP_n(t) + At + B, \tag{2.30}$$

where A, B and D are constants, and $P_n(t)$ is the Legendre polynomial of order n. For each eigen mode, there is one eigenvalue which corresponds to the critical condition for the bifurcation.

Detailed calculations show that the critical loading conditions for the eigen modes of δ_r with $n \geq 2$ is physically unrealistic, which is consistent with the conclusion given by Shield et al [87]. So we next only focus on the first two eigen modes in the balloon.

For n=0, the eigen mode is a constant which corresponds to a homogeneous perturbation,

$$\delta_r(\theta) = 1, \ \delta_t(\theta) = 0, \tag{2.31}$$

and the critical condition for the bifurcation is given by,

$$2S_1^0 - \lambda_0 \frac{\partial S_1^0}{\partial \lambda_1} - \lambda_0 \frac{\partial S_1^0}{\partial \lambda_2} + \frac{2\pi R^4 \lambda_0^5}{H} \frac{\partial p}{\partial V} = 0. \tag{2.32}$$

For n=1, the eigen mode represents an inhomogeneous perturbation,

$$\delta_r(\theta) = \cos\theta, \ \delta_t(\theta) = 0, \tag{2.33}$$

and the critical condition for the bifurcation is given by,

$$S_1^0 - \lambda_0 \frac{\partial S_1^0}{\partial \lambda_1} - \lambda_0 \frac{\partial S_1^0}{\partial \lambda_2} = 0. \qquad (2.34)$$

A combination of Eqs. (2.16), (2.17) and (2.32) or (2.34) gives a nonlinear algebra equation with single unknown λ_0, which corresponds to the critical conditions of bifurcation for the mode of *n=0* or *n=1*.

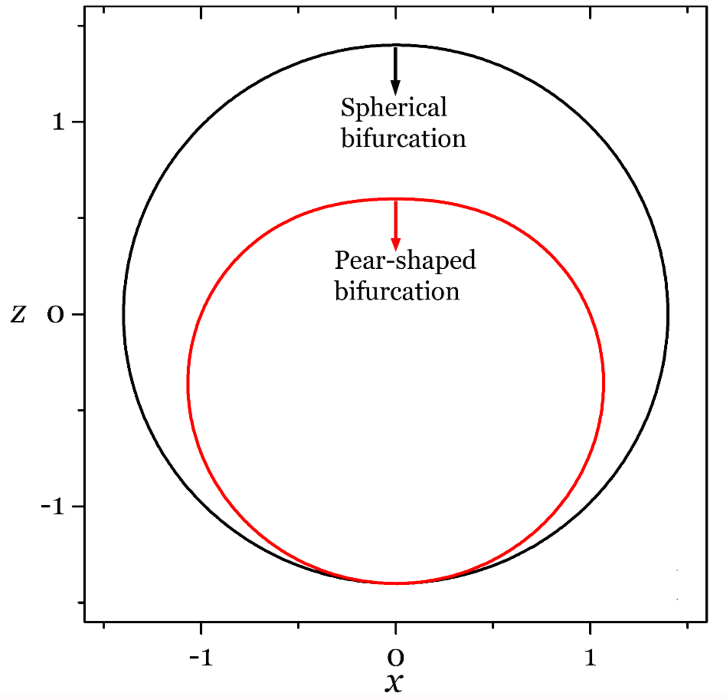

Figure 2.3: Spherical and pear-shaped bifurcation modes calculated from the linear perturbation analysis.

The bifurcation modes for *n=0* and *n=1* are both plotted in Fig. 2.3. Following literature, we name *n=0* as spherical bifurcation mode and *n=1* as pear-shaped bifurcation mode. The critical conditions for the bifurcation are also calculated and plotted in Fig. 2.2. The circle and square dots represent the critical conditions for the spherical and pear-shaped bifurcation mode, respectively. As expected, for the spherical bifurcation mode, the critical conditions coincide with the extreme points in the *p*-*V* curve of the balloon with homogenous deformation.

2.5 Inhomogeneous deformation

The bifurcation analysis conducted in sec. 4 predicts that inhomogeneous deformation mode can exist in a spherical dielectric elastomer balloon subjected to internal pressure and electric voltage. In this section, we conduct post-bifurcation analysis of the dielectric elastomer balloon by numerically solving the governing equations of the balloon formulated in sec.2.

We use shooting method to numerically solve Eqs. (2.8)~(2.10). Specifically, the values of the three variables in the southern pole of the balloon are set to be $\lambda_1(0)=\lambda_2(0)=\lambda_a$ and $\alpha(0)=\pi/2$. Those values are used as the initial conditions and Eqs. (2.8)~(2.10) can be numerically integrated to obtain $\lambda_1(\theta)$, $\lambda_2(\theta)$ and $\alpha(\theta)$. We continuously vary the value of λ_a until the boundary conditions in the northern pole: $\lambda_1(\pi)=\lambda_2(\pi)$ and $\alpha(\pi)=-\pi/2$ are all satisfied.

With a given pressure and electric voltage, we can obtain the solutions for homogeneous deformation of the balloon, which agree with the solution described by Eq. (2.24). As expected, in addition to the homogeneous deformation, for a certain range of pressure with different voltages, we can also obtain the solution describing inhomogeneous deformation of the balloon, which is also plotted in Fig. 2.2 by dash curves.

To quantitatively describe Fig. 2.2, we mark several key pressures for three different voltages, which are maximum pressure $p_{\max}$, minimum pressure $p_{\min}$ obtained from the homogeneous deformation and critical pressures for the pear-shaped bifurcations predicted from the linear perturbation analysis: p_{cr1} and p_{cr2}. All the four pressures depend on the magnitude of the voltage. For a given voltage, when $p<p_{\min}$ (or $p>p_{\min}$), the balloon has one equilibrium solution, corresponding to spherical deformation. For $p_{\min}<p<p_{\max}$, three equilibrium solutions of spherical

deformation can be obtained, and a pear-shaped deformation mode exists if the pressure is between the two critical pressures, namely, $p_{cr2}<p<p_{cr1}$. It is also shown in Fig. 2.2 that the electric field applied to the dielectric elastomer leads to a lower critical pressure for the bifurcation.

Fig. 2.2 also shows that as the voltage is increased, the difference of the p-V curve between the homogeneous deformation and inhomogeneous deformation increases. The results can be qualitatively understood as follows: when the balloon bifurcates from a spherical shape with homogeneous deformation to a non-spherical shape, the thickness of the balloon membrane becomes inhomogeneous, which results in inhomogeneous electric field since the voltage across the membrane is a constant. The inhomogeneous electric filed will induce inhomogeneous Maxwell stress which in-turn further increases the deviation of the non-spherical bifurcated shape from the spherical shape.

Fig. 2.4 plots the shapes and electric field of the dielectric elastomer balloon in two adjacent deformation modes marked in Fig. 2.2. When the electric potential is zero, the differences of the volume and the geometry between the spherical and non-spherical modes are almost negligible. As the voltage increases, the volume and the geometrical difference between the two modes become more and more obvious. For the non-spherical deformation mode, the electric field in the balloon membrane is highly inhomogeneous.

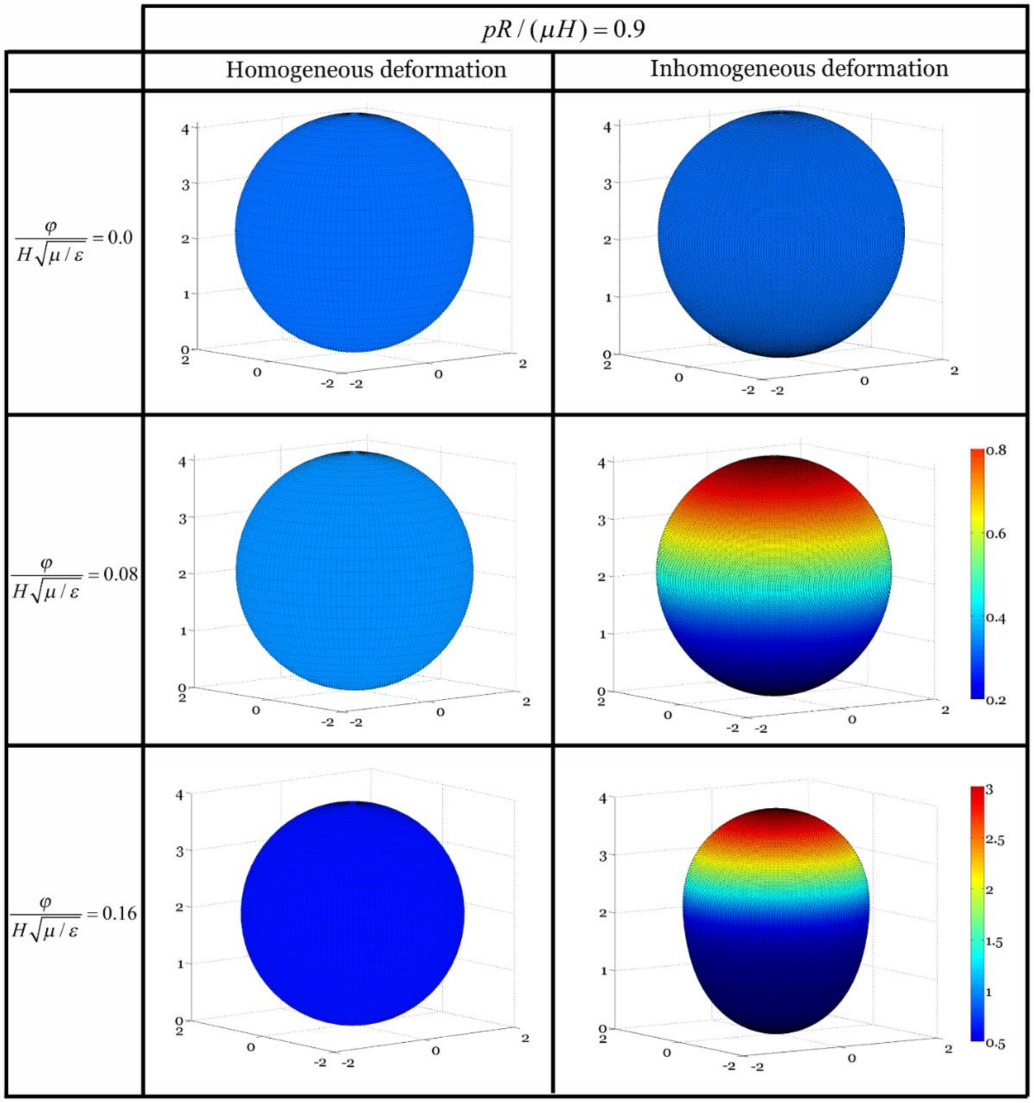

Figure 2.4: Calculated shapes and electric field in a spherical dielectric elastomer balloon in two adjacent deformation modes (spherical mode and pear-shaped mode) marked by triangles in Fig.2. When the electric voltage is high, large electric field concentration can be observed in the pear-shaped mode (right column).

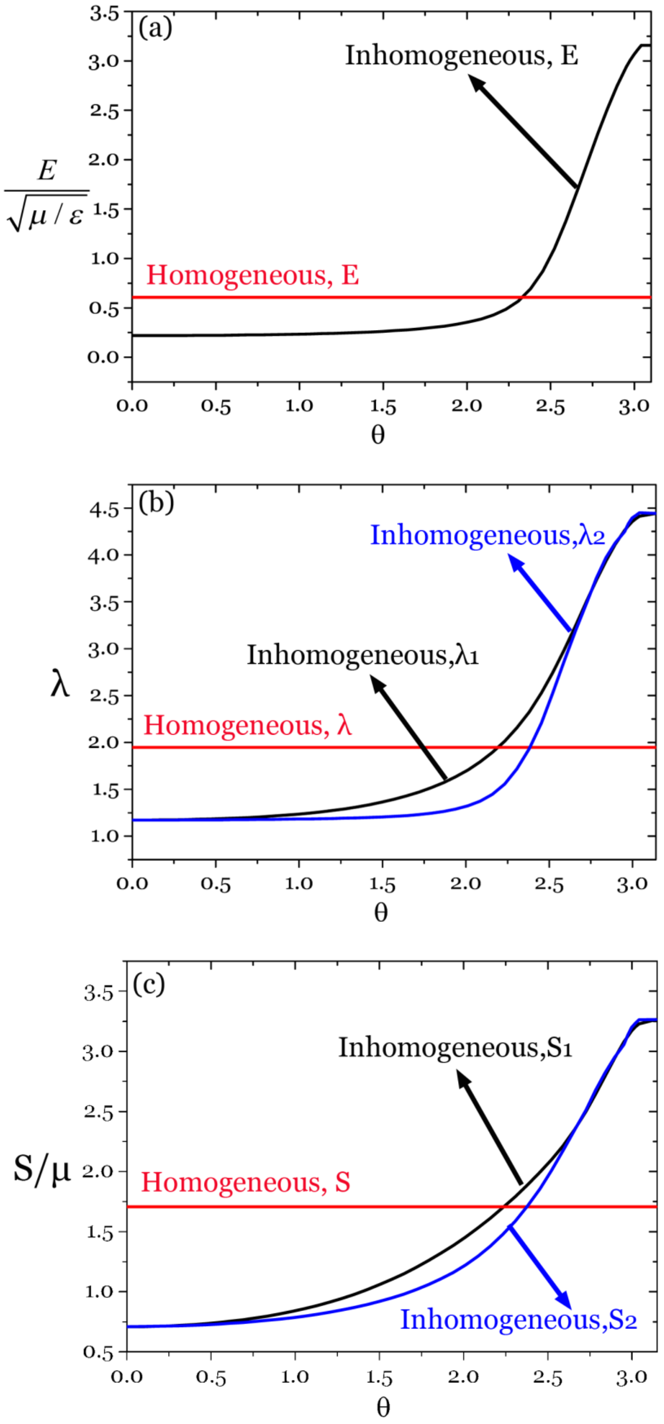

Figure 2.5: Distribution of the electric field, stretch and nominal stress in the dielectric elastomer balloon for homogenous and inhomogeneous deformation modes for $\varphi/\left(H\sqrt{\mu/\varepsilon}\right)=0.16$ as shown in Fig.4.

Fig. 2.5 plots the electric field, stretch and stress distribution in the dielectric elastomer balloon with the deformation modes as shown in Fig. 2.4 for $\varphi / \left(H\sqrt{\mu / \varepsilon} \right) = 0.16$. Compared to the homogeneously deformed state, the concentration factor of the electric field can be as large as 500% and the concentration factor of stresses and stretches can be as large as 200%. The high concentration factor explains the experimental observations by Li et al. [79] that localized bulging out in the dielectric elastomer balloon usually immediately leads to electric breakdown of the dielectric membrane.

2.6 Stability analysis

In the previous sections, we have demonstrated that both spherically and non-spherically deformed dielectric elastomer balloons can be in equilibrium states. However, it is still unclear whether the equilibrium states we obtained are stable or not. In this section, we will conduct stability analysis.

Following the energetic method adopted by different researchers [84, 88, 139], we first derive second variation of the free energy of the dielectric elastomer balloon system. If the second variation of the free energy of an equilibrium state is positive definite, the state is energetically stable. On the other hand, if there is any perturbation which can lead to negative second variation of the free energy of an equilibrium state, the state is regarded as energetically unstable.

It is also known that the stability of a structure depends on its loading method. In this article, we focus on four different ways of applying electromechanical loadings onto the dielectric elastomer balloon. In terms of the mechanical loading, we consider either gradually increasing the internal pressure or the number of ideal gas molecules inside the balloon, for which we call pressure-control mode or ideal gas mass-control mode respectively. In terms of electrical loading, we consider either gradually increasing the voltage across the thickness of the dielectric membrane or the total amount of charge on its surface, for which we call voltage-control mode or charge-control mode respectively. Consequently, we have four different combinations of electomechanical loading method. We next derive the second variation of the free energy for the four different cases.

In the pressure-control and voltage-control mode, the balloon, together with the pressure and electric voltage forms a thermodynamic system with the free energy given by,

$$F = \int (W_s(\lambda_1, \lambda_2) + W_e(\lambda_1, \lambda_2))dV_m - pV - \varphi Q, \tag{2.35}$$

where $W_s(\lambda_1, \lambda_2)$ and $W_e(\lambda_1, \lambda_2)$ are strain energy density and electrostatic energy density of the membrane, $\mathrm{d}V_m=2\pi HR^2 sin\theta \mathrm{d}\theta$ is the volume element of the dielectric membrane, and $V = \int_0^\pi \pi x^2 z' d\theta$ is volume of the balloon. The relationship between electric displacement and electric field in the dielectric membrane is assumed to be linear, the electrostatic energy is,

$$\int W_e(\lambda_1, \lambda_2)dV_m = \int_0^\pi \left(\frac{\varepsilon E^2}{2}\right) 2\pi HR^2 \sin\theta d\theta, \tag{2.36}$$

where $W_e(\lambda_1, \lambda_2)=\varepsilon E^2/2$ is the electrostatic energy density. Adopting the assumption of ideal dielectric elastomer, $D=\varepsilon E$, and the definition of the electric displacement, $D=\mathrm{d}Q/\mathrm{d}a$, we have,

$$Q=\int_0^\pi (\varepsilon E)\,2\pi\lambda_1\lambda_2 R^2\sin\theta d\theta, \tag{2.37}$$

where $da=2\pi\lambda_1\lambda_2 R^2 \sin\theta d\theta$ is the area of the surface element of the membrane in the deformed state. Putting Eqs. (2.36) and (2.37) into Eq. (2.35), with the definition $E=\varphi/h=\lambda_1\lambda_2\varphi/H$, the free energy is in the pressure-control and voltage-control mode,

$$F=2\pi R^2 H\int_0^\pi\left(W_s(\lambda_1,\lambda_2)-\frac{\varepsilon\varphi^2}{2H^2}(\lambda_1\lambda_2)^2\right)\sin\theta d\theta-p\int_0^\pi \pi x^2 z' d\theta. \tag{2.38}$$

Define the first two terms in Eq. (2.38) as,

$$W(\lambda_1,\lambda_2)=W_s(\lambda_1,\lambda_2)-\frac{\varepsilon\varphi^2}{2H^2}(\lambda_1\lambda_2)^2. \tag{2.39}$$

For simplicity, R is taken to be unity in the following analysis. Following [84] ,the second variation of the free energy can be expressed as,

$$\delta^2 F=2\pi HR^2\int_0^\pi\left(\mathbf{v}\cdot\mathbf{S}\mathbf{v}+2\mathbf{v}\cdot\mathbf{L}\mathbf{v}'+\mathbf{v}'\cdot\mathbf{K}\mathbf{v}'\right)d\theta \tag{2.40}$$

where,

$$\mathbf{S}=\begin{bmatrix}\dfrac{W_{11}}{R^2\sin\theta}-\left(\dfrac{W_{12}}{R^3\lambda_2}x'\right)'-\dfrac{pz'}{HR^2} & 0\\ 0 & 0\end{bmatrix}=\begin{bmatrix}\alpha_1 & 0\\ 0 & 0\end{bmatrix}, \tag{2.41}$$

$$\mathbf{L}=\begin{bmatrix}0 & \dfrac{W_{12}z'}{R^3\lambda_2}-\dfrac{px}{HR^2}\\ 0 & 0\end{bmatrix}=\begin{bmatrix}0 & \alpha_2\\ 0 & 0\end{bmatrix}, \tag{2.42}$$

$$\mathbf{K}=\begin{bmatrix}\dfrac{(\lambda_2 W_{22}x'^2+W_2 z'^2)\sin\theta}{R^4\lambda_2^3} & \dfrac{(\lambda_2 W_{22}-W_2)\sin\theta}{R^4\lambda_2^3}x'z' \\ \dfrac{(\lambda_2 W_{22}-W_2)\sin\theta}{R^4\lambda_2^3}x'z' & \dfrac{(\lambda_2 W_{22}z'^2+W_2 x'^2)\sin\theta}{R^4\lambda_2^3}\end{bmatrix}=\begin{bmatrix}\alpha_4 & \alpha_5 \\ \alpha_5 & \alpha_3\end{bmatrix} \tag{2.43}$$

where $W_1=\partial W/\partial\lambda_1, W_{12}=\partial^2 W/\partial\lambda_1\partial\lambda_2$, etc. **v** is a vector of displacement perturbation in the *x* and *z* direction, with $\mathbf{v}=[\delta x, \delta z]^{\mathrm{T}}$ and $\mathbf{v}'=[\delta x', \delta z']^{\mathrm{T}}$.

Next, we derive the second variation of the free energy $\delta^2 F$ of the dielectric elastomer balloon under ideal gas mass-control and voltage-control mode. So, the enclosed ideal gas, the balloon and the electric voltage form a thermodynamic system with the free energy given by,

$$F=\int (W_s(\lambda_1,\lambda_2)+W_e(\lambda_1,\lambda_2))dV_m+\Phi(V,N)-\varphi Q, \tag{2.44}$$

where $\Phi(V, N)$ is the gas potential energy,

$$\Phi(V,N)=-kTN\ln\frac{V}{V_0}, \tag{2.45}$$

where T is the temperature of the gas, V and V_0 are the current and initial volume of the gas, N is the number of the gas molecules and k is the Boltzmann constant. Pressure is defined by $p=-\partial\Phi/\partial V=kTN/V$. The second variation Eq. (2.44) is,

$$\delta^2 F-\frac{kTN}{V^2}(\delta V)^2=2\pi HR^2\int_0^\pi\left(\mathbf{v}\cdot\mathbf{S}\mathbf{v}+2\mathbf{v}\cdot\mathbf{L}\mathbf{v}'+\mathbf{v}'\cdot\mathbf{K}\mathbf{v}'\right)d\theta, \tag{2.46}$$

In the following, we study pressure-control and charge-control mode. When the total amount of charge on the surface of dielectric elastomer membrane is given, the voltage φ is an unknown constant. According to Eq. (2.37) and the definition $E=\lambda_1\lambda_2\varphi/H$,

$$E=\frac{Q}{2\varepsilon R^2\Lambda}\lambda_1\lambda_2, \tag{2.47}$$

where $\Lambda=\int_0^{\pi}\pi(\lambda_1\lambda_2)^2\sin\theta d\theta$.

The thermodynamic system under the pressure-control and charge-control mode is formed by the balloon and the pressure, and the free energy of the system is,

$$F=\int(W_s(\lambda_1,\lambda_2)+W_e(\lambda_1,\lambda_2))dV_m-pV. \tag{2.48}$$

The electrostatic energy of the dielectric membrane is obtained by putting Eq. (2.47) into (2.36), and it is expressed as,

$$\int W_e(\lambda_1,\lambda_2)dV_m=\frac{Q^2H}{4\varepsilon R^2\Lambda}, \tag{2.49}$$

The second variation of the free energy is,

$$\delta^2F-\frac{Q^2H}{2\varepsilon R^2\Lambda^3}(\delta\Lambda)^2=2\pi HR^2\int_0^{\pi}\left(\mathbf{v}\cdot\mathbf{Sv}+2\mathbf{v}\cdot\mathbf{Lv'}+\mathbf{v'}\cdot\mathbf{Kv'}\right)d\theta, \tag{2.50}$$

where $\delta\Lambda$ is the first variation of Λ.

For ideal gas mass-control and charge-control mode, the dielectric membrane balloon and the enclosed ideal gas form a thermodynamic system with the free energy,

$$F=\int (W_s(\lambda_1,\lambda_2)+W_e(\lambda_1,\lambda_2))dV_m-kTN\ln\frac{V}{V_0}. \tag{2.51}$$

Based on the previous derivations, it is easy to show that the second variation of the free energy,

$$\delta^2 F-\frac{Q^2H}{2\varepsilon R^2\Lambda^3}(\delta\Lambda)^2-\frac{kTN}{V^2}(\delta V)^2=2\pi HR^2\int_0^{\pi}\left(\mathbf{v}\cdot\mathbf{Sv}+2\mathbf{v}\cdot\mathbf{Lv}'+\mathbf{v}'\cdot\mathbf{Kv}'\right)d\theta. \tag{2.52}$$

Without further calculations, by comparing Eqs (2.40), (2.46), (2.50) and (2.52), we can conclude that for the same equilibrium state, the second variation of the free energy is the smallest for pressure-control and voltage-control mode but the largest for mass-control and charge-control mode, which indicates that pressure-control and voltage-control mode is the least stable while the mass-control and charge-control mode is the most stable.

It can be further proved that second variation of free energy for all four different loading cases can be evaluated by solving the following eigenvalue equation [84]:

$$\mathbf{Sv}+\mathbf{Lv}'-(\mathbf{L^T v}+\mathbf{Kv}')'-\frac{\delta px}{HR^2}\begin{pmatrix} z' \\ -x' \end{pmatrix}-\frac{Q\delta\varphi}{HR^6\Lambda}\begin{pmatrix} \dfrac{x(x'^2+z'^2)}{\sin\theta}-\left(\dfrac{x^2x'}{\sin\theta}\right)' \\ -\left(\dfrac{x^2z'}{\sin\theta}\right)' \end{pmatrix}=\alpha\sin\theta\mathbf{v}, \tag{2.53}$$

of which eigen mode can be viewed as the perturbation and the eigenvalue α is exactly the second variation of the free energy $\delta^2 F$. The last two terms on the left hand side of Eq. (2.53) is zero if the balloon is in the pressure-control and voltage-control mode, while $\delta p=-kTN\delta V/V^2$ and $\delta\varphi=-QH\delta\Lambda/2\varepsilon R^2\Lambda^2$ for the mass-control and charge-control mode, respectively.

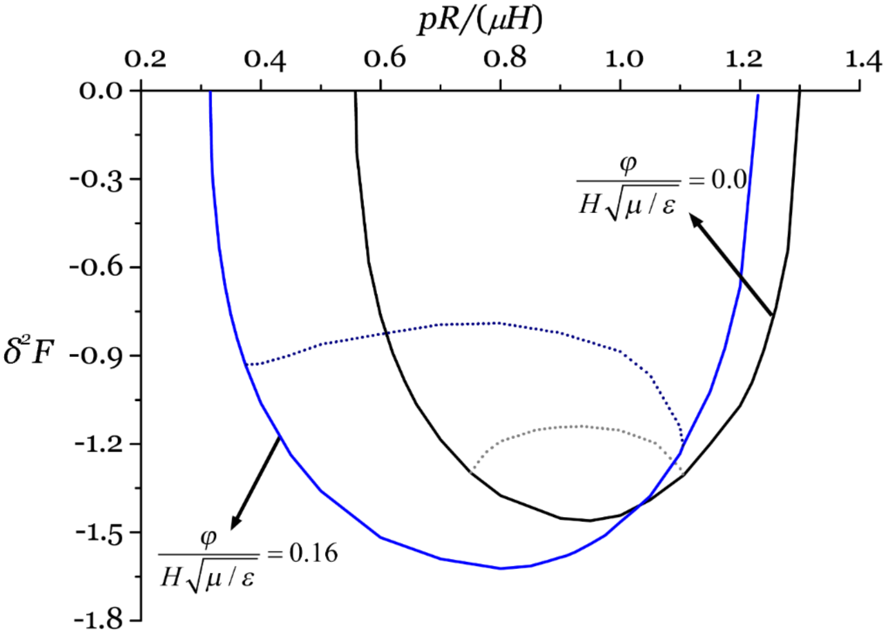

Figure 2.6: Under pressure-control and voltage-control mode, second variation of free energy of the spherical deformation in the descending path of *p*-*V* curve in Fig.2 and non-spherical deformation can be negative. The solid line represents a negative value for the spherical deformation mode while the dash line shows a negative value for the non-spherical deformation mode. The results indicate that under pressure-control and voltage-control mode, both spherical deformation in the descending path of p-V curve and non-spherical deformation of the dielectric elastomer balloon are energetically unstable.

The eigenvalue problem Eq. (2.53) can be solved by shooting method with boundary conditions,

$$v_1(0)=v_1(\pi)=0. \tag{2.54}$$

In pressure-control and voltage-control mode, we can find at least one negative eigenvalue for non-spherical deformation mode and the spherical deformation mode in the descending path of the *p*-*V* curve shown in Fig.2. The negative eigenvalue is plotted in Fig. 2.6 for two different voltages. The calculation indicates that both non-spherical deformation mode and spherical deformation mode in the descending path of *p*-*V* curve are energetically unstable.

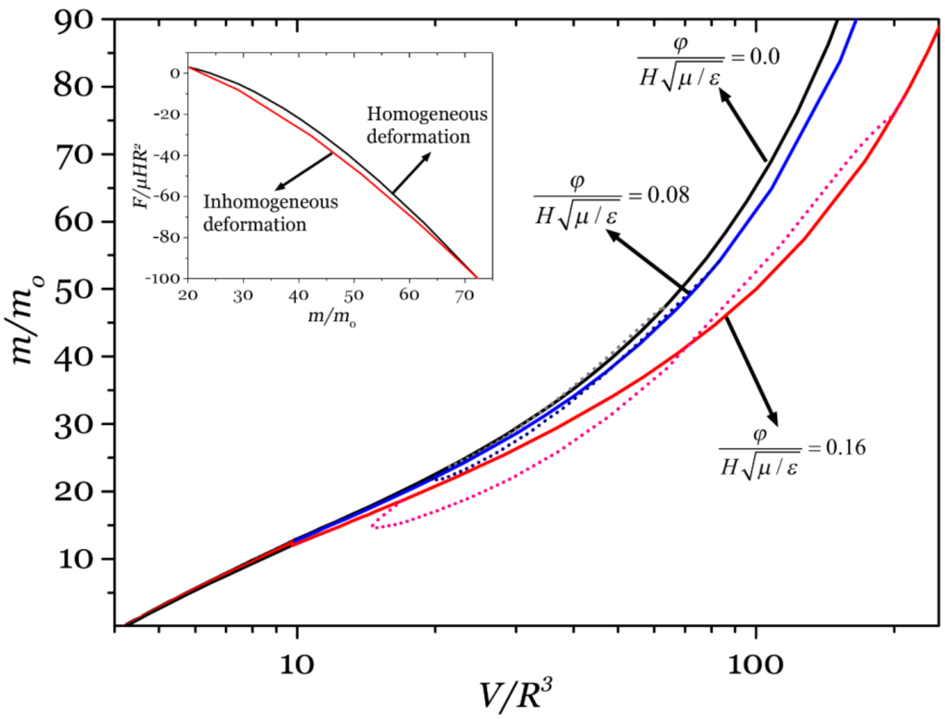

Figure 2.7: The ideal gas mass-volume (*m*-*V*) curves for a dielectric elastomeric balloon subjected to three different voltages. During the deformation, the gas molecules obey the ideal gas law. The spherical deformation is represented by the solid line and the non-spherical deformation is represented by dash line.

For mass-control or charge-control mode, one additional constraint equation for the perturbations needs to be satisfied, which is

$$\left(\frac{HR^2V}{p\pi}+\int_0^\pi \frac{x^2}{2(\alpha_3-\alpha)}d\theta\right)\frac{\delta p}{HR^2}+\left(\int_0^\pi \frac{x^4 z'}{(\alpha_3-\alpha)\sin\theta}d\theta\right)\frac{Q\delta\varphi}{HR^6\Lambda}=-2\int_0^\pi c_1 v_1 d\theta, \tag{2.55}$$

$$\left(\int_0^\pi \frac{x^4 z'}{2(\alpha_3-\alpha)\sin\theta}d\theta\right)\frac{\delta p}{HR^2}+\left(\frac{\varepsilon R^{12}\Lambda^3}{\pi Q^2}+\int_0^\pi \frac{x^4 z'^2}{(\alpha_3-\alpha)\sin^2\theta}d\theta\right)\frac{Q\delta\varphi}{HR^6\Lambda}=-\int_0^\pi c_2 v_1 d\theta, \tag{2.56}$$

where c_1 and c_2 are

$$c_1 = -\frac{\alpha_2 x^2}{2(\alpha_3-\alpha)} + \frac{1}{2}\left(\frac{\alpha_5 x^2}{\alpha_3-\alpha}\right)' + xz', \tag{2.57}$$

$$c_2 = -\frac{\alpha_2 x^2 z'}{(\alpha_3-\alpha)\sin\theta} + \left(\frac{\alpha_5 x^2 z'}{(\alpha_3-\alpha)\sin\theta}\right)' + \frac{x(x'^2+z'^2)}{\sin\theta} - \left(\frac{x^2 z'}{\sin\theta}\right)'. \tag{2.58}$$

Because of the additional constraints, it is much more difficult to find a negative eigenvalue for Eq. (2.53). Detailed calculations show that for all the other three loading methods, the non-spherical deformation of the dielectric elastomer balloon is energetically stable.

At last, we would like to add one more comment on the mass-control and voltage- control mode. It is well known that under pressure-control mode, snap-through instability in a balloon may happen during its inflation process. Such instability can be eliminated by adopting ideal gas mass-control mode. As shown in Fig. 2.2, if only spherical deformation in the balloon is considered, for all three different electric voltages, only one equilibrium solution exists for the mass-control loading mode, which is the crossing point between the curve representing ideal gas law and the calculated *p*-*V* curve for the balloon, so no instability will happen. However, if non-spherical deformation is not excluded, even in ideal gas mass-control loading mode, multiple solutions can coexist, namely, there may be several crossing points between the curve representing ideal gas law and the calculated *p*-*V* curves for the balloon as shown in Fig. 2.2. To be more explicit, we also plot the mass of idea gas molecules as a function of the balloon volume in Fig. 2.7 for three different voltages. For a fixed number of idea gas molecules in a certain range, multiple equilibrium solutions which correspond to spherical and non-spherical deformation of the balloon can be found. Moreover, we also found that in the ideal gas mass-control mode, once non-spherical deformation of the balloon is an equilibrium solution, it always has lower free energy than the spherically deformed balloon as shown in the inset of Fig. 2.7. This indicates that non-spherical deformation is more energetic favorable.

2.7 Concluding remark

This chapter studies shape bifurcation of a spherical dielectric elastomer balloon subjected to internal pressure and electric voltage. Using linear perturbation analysis, we obtain the bifurcation mode and the corresponding critical conditions of a dielectric elastomer balloon under the action of internal pressure and electric voltage. By numerically solving the governing equations of the dielectric elastomer balloon with axisymmetric deformation and under different electromechanical loading conditions, we obtain both spherical deformation and non-spherical deformation solutions for the balloon. Our calculations further show that shape difference between two adjacent spherical and non-spherical deformation modes can be greatly enhanced by increasing the electrical voltage. The non-spherical deformation of the dielectric elastomer balloon in-turn induce large electric field concentration and stress/stretch concentration in certain area of the balloon, which may lead to the failure of the system. Finally, we calculate second variation of the free energy of the balloon in different equilibrium states. Our calculations demonstrate that non-spherical deformation of the balloon can be either energetically stable or unstable depending on the eletromechanical loading method.

Chapter 2, in full appears in the paper “Shape Bifurcation of a Spherical Dielectric Elastomer Balloon under the Actions of Internal Pressure and Electric Voltage”, *Journal of Applied Mechanics* 82, no. 10 (2015): 101002, by X. Liang and S. Cai. The dissertation author was the primary investigator and author of this paper.

Chapter 3 New electromechanical instability modes in dielectric elastomer balloons

Under the actions of internal pressure and electric voltage, a dielectric elastomeric membrane mounted on an air chamber can deform to a balloon shape. Due to the nonlinear deformation, snap-through instability can happen in the balloon, which has been harnessed to achieve giant voltage-triggered deformation. In addition to the snap-through instability, with an applied voltage, a new electromechanical instability mode with a localized bulging-out in the balloon has been recently observed in experiments. However, the reported phenomenon has not been well explained. In this article, through numerical computation, we obtain the relation between the volume of the balloon and its internal pressure, when the balloon is subjected to different voltages. We find out that when the applied voltage is small, the pressure vs. volume diagram of a balloon can be represented by an N-like curve, which is similar to the conventional hyperelastic balloon only subjected internal pressure; when the voltage is larger than a critical value, new instability modes in the balloon emerge, which have a localized bulging-out, similarly to the shape observed in the experiments. We further show that the critical voltage for the new instability mode of the DE balloon is closely associated with the prestretches applied to the membrane and the hyperelastic model for the elastomer.

3.1 Introduction

Dielectric elastomer (DE) has been regarded as a promising soft active material due to many of their unique properties such as large voltage-induced deformation, low noise during operation, low cost and fast response [140]. In a recent decade, DE has been intensively explored in various applications, including artificial muscle [123-125, 141], haptic devices [126, 127], micro-pumps [128-131] and adaptive lens [132, 135, 142, 143]. DE adopted in the aforementioned applications is normally a sandwich structure with a soft elastomeric layer covered by two compliant electrodes on the top and bottom surfaces [23]. The elastomer can dramatically reduce its thickness and expand in area when external electric voltage is applied across the thickness direction.

Nonlinear field theory for elastic dielectric accounting for the coupling between mechanics and electricity was originally proposed by Toupin [102]. Relevant studies of elastic dielectric were further developed by Landau and Lifshitz [144], Eringen [104] and Tiersten [105]. The theory has been re-examined in recent years due to the rapidly growing applications of DE. Constitutive models of DE accounting for large deformation have been developed to explain diverse experimental observations and also provide guidelines for designing new DE devices [25-27].

Among all the DE devices, balloon is one of the most frequently adopted geometries. DE balloons have been successfully developed as spherical-shape actuators and tactile devices [119, 129, 130]. Recently, more applications of DE balloons have been explored due to their unique responses to different electromechanical loadings. Nonlinear vibration with tunable frequency has been demonstrated in spherical DE balloons subjected to a constant pressure and an AC voltage [117]. Rudykh and Bhattacharya [136] predicted snap-through actuation in a thick-walled DE balloon. Liang and Cai [145] has recently identified inhomogeneous shape bifurcation modes in a spherical DE balloon subjected to internal pressure and a constant electric voltage. Recently, Li et al. [79] has observed voltage induced snap-through instability in DE balloons. In their experiment, an acrylic elastomer membrane (3M$^{\text{TM}}$VHB$^{\text{TM}}$4910), covered by carbon grease over the top and bottom surfaces as soft electrodes, is mounted on an air chamber. The membrane deforms to a balloon shape after air is pumped into the chamber through a valve. By closing the valve, the amount of air enclosed by the chamber and balloon is fixed, and a voltage is subsequently applied between the electrodes to further deform the DE membrane. Similar to a hyperelastic balloon only subjected to an internal pressure [80], snap-through instability in a DE balloon was observed due to the non-monotonic relationship between the internal pressure and the volume of the balloon. Additionally, in the experiment, an unusual deformation mode of a DE balloon has been observed [79]. When the volume of the chamber is small, a region on top of the balloon is observed to expand significantly more than its neighboring area (Fig. 3.1b and 3.1c). The area keeps bulging-out as the voltage increases until electrical breakdown happens in the membrane as shown in Fig. 3.1. Different from the conventional snap-through instability, the new instability mode is more localized around the apex of the balloon, with the rest of membrane almost unperturbed. Such a instability in a balloon has never been reported before in other loading conditions and was also left unexplained in the paper [79].

In this article, we will study the new instability mode observed in a DE balloon described above. Our numerical calculations show that when the applied voltage is low, the relationship between the internal pressure and volume of a DE balloon is similar to that of a hyperelastic balloon only subjected to an internal pressure, only with quantitative differences; when the applied voltage is high, a new instability mode emerges in the DE balloon for a certain range of pressure.

We believe that the new instability mode of the DE balloon is associated with the non-convexity of the free energy density function of DE.

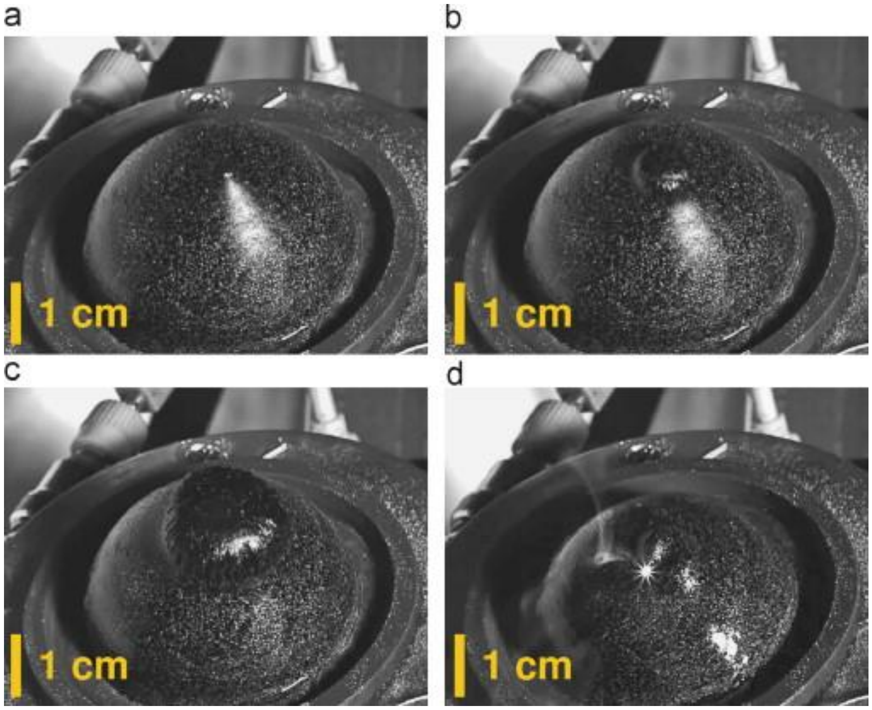

Figure 3.1: Experimental observation of localized bulge-out in an inflated DE membrane [79]. In the experiment, a soft DE membrane is mounted on a chamber and air is pumped into the chamber through a valve. The membrane deforms to a balloon shape (a) and the valve is then closed to fix the total amount of air inside the chamber and the balloon. A voltage is subsequently applied to the membrane to further deform the balloon (b-c). When the volume of chamber is small, the apex of the balloon bulges out significantly, which is greatly different from the shape expected from traditional balloon problem. The applied voltage ramps up until the membrane is failed by electrical breakdown (d).

The remainder of the article is organized as follows. Section 2 summarizes the field equations of a DE membrane mounted on a circular hole of an air chamber and subjected to internal pressure and electric voltage. Those equations are solved numerically in Section 3. New instability mode in the balloon with localized bulging-out is identified when the applied voltage is high. In Section 4, we demonstrate that localized bulging-out instability modes of the DE balloon can be affected by prestretches and material parameters in the hyperelasticity model. We propose that the new instability mode is associated with the non-convexity of the free energy density function of DE in Section 5. Section 6 summarizes our findings in the article.

3.2 Inhomogeneous deformation of a DE membrane mounted on an air chamber

To make this article be self-contained, in this section, we summarize the governing equations for a flat DE membrane with homogenous thickness H subjected to internal pressure p and electric voltage Φ as shown in Fig. 3.2. These equations are mathematically identical to the ones presented in the paper of Li *et al.* [79], though the derivation is slightly different. In the problem, an undeformed DE membrane with radius R_0 is mounted over a circular ridge of a chamber, as shown in Fig. 3.2a. We assume the deformation of the actuated DE balloon is axisymmetric. A Cartesian coordinate system x-z is built upon the apex of the deformed membrane, which coincides with the material point of the center of the undeformed membrane (Fig. 3.2b). For a point in the undeformed flat membrane: $(X, 0)$, it deforms to (x, z) under electromechanical loading. Consider a material element of the membrane, between two particles X and $X+dX$. When the membrane is in the deformed state, the particle X takes the position of coordinates $x(X)$ and $z(X)$, while the particle $X+dX$ takes the position of coordinates $x(X+dX)$ and $z(X+dX)$. In the undeformed state, the material element is a straight segment, with length dX. In the deformed state, the material element becomes a curved segment, with length $\lambda_1 dX$, where λ_1 is the longitudinal stretch. In a curved state, let $\alpha(X)$ be the slope of a membrane at material particle X. Write $dx=x(X+dX)-x(X)$, so that,

$$\frac{dx}{dX} = \lambda_1 \cos\alpha. \tag{3.1}$$

Similarly, dz=z(X+dX)-z(X), so that,

$$\frac{dz}{dX} = \lambda_1 \sin\alpha. \tag{3.2}$$

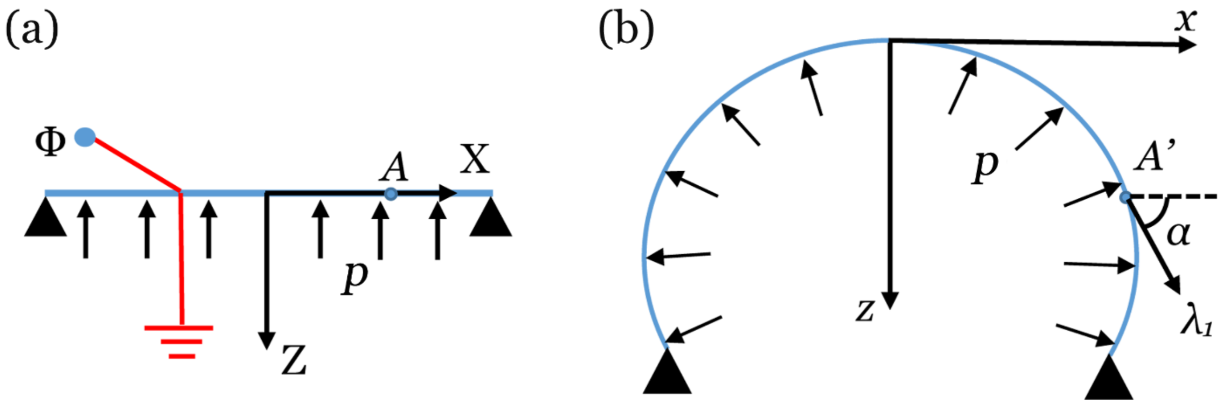

Figure 3.2: Schematics of the deformation of dielectric membrane under the action of pressure and applied voltage. (a) Undeformed dielectric membrane. (b) Deformed dielectric membrane.

In the undeformed state, a circle of material particles is of a perimeter $2\pi X$. In the deformed state, these material particles occupy a circle of perimeter $2\pi x$. The deformation corresponds to the latitudinal stretch, λ_2. In summary, the two principle stretches in the longitudinal and latitudinal direction in the DE balloon are given by,

$$\lambda_1 = \sqrt{\left(\frac{dx}{dX}\right)^2 + \left(\frac{dz}{dX}\right)^2}, \tag{3.3}$$

$$\lambda_2 = \frac{x(X)}{X}. \tag{3.4}$$

Force balance equations of the deformed balloon in the *x*-direction and the *z*-directions are given by

$$\frac{d}{dX}\left(\sigma_1 hx\cos\alpha\right)+px\frac{dz}{dX}-\frac{\sigma_2 h}{\sin\alpha}\frac{dz}{dX}=0, \tag{3.5}$$

$$\frac{d}{dX}\left(\sigma_1 hx\sin\alpha\right)-px\frac{dx}{dX}=0, \tag{3.6}$$

where σ_1 and σ_2 are the true stresses in the longitudinal direction and latitudinal direction, respectively, p is the internal pressure, and $h(X)$ is the thickness of the deformed DE balloon.

DE is assumed to be incompressible, namely,

$$\lambda_1\lambda_2\lambda_3=1, \tag{3.7}$$

where $\lambda_3=h(X)/H$ is the stretch in the thickness direction.

Ideal dielectric elastomer model [120] is adopted here by assuming dielectric behavior of an elastomer is exactly the same as that of a polymer melt and the electrical permittivity of DE is not affected by its deformation. We relate the electric displacement D with the electric field E by the following linear equation,

$$D=\varepsilon E, \tag{3.8}$$

where ε is the electrical permittivity. The electric displacement is equal to the charge density, namely, $D=dQ/da$, where da is the area of the deformed DE membrane and dQ is the correspondent charge accumulated over the area. Electric field in the membrane can be calculated by $E=\Phi/h$, which is inhomogeneous when the thickness of the membrane becomes inhomogeneous.

Using the incompressibility constraint (Eq. (3.7)), the relations between the true stresses and stretches in the DE membrane can be given by ideal dielectric elastomer model [23, 120] as,

$$\sigma_1 - \sigma_3 = \lambda_1 \frac{\partial W_s(\lambda_1, \lambda_2)}{\partial \lambda_1} - \varepsilon E^2, \tag{3.9}$$

$$\sigma_2 - \sigma_3 = \lambda_2 \frac{\partial W_s(\lambda_1, \lambda_2)}{\partial \lambda_2} - \varepsilon E^2, \tag{3.10}$$

where $W_s(\lambda_1, \lambda_2)$ is strain energy density of the elastomer in deformed state with λ_1, λ_2 as its principle stretches, and Gent model [146] is adopted:

$$W_s(\lambda_1, \lambda_2) = -\frac{\mu J_{\mathrm{lim}}}{2} \log\left(1 - \frac{\lambda_1^2 + \lambda_2^2 + \lambda_1^{-2}\lambda_2^{-2} - 3}{J_{\mathrm{lim}}}\right), \tag{3.11}$$

where μ is the shear modulus for infinitesimal deformation, and J_{lim} is a constant related to the stretching limit of the elastomer, which is taken to be J_{lim}=270 and 97.2 in this article [79, 147].

Considering the thickness of the DE balloon is much smaller than its radius, the stress in the normal direction of the balloon is negligible compared to the membrane stresses, namely,

$$\sigma_3 = 0. \tag{3.12}$$

Using the geometric relations in Eqs. (3.1) and (3.2) and expressing $d\alpha/dX$, dz/dX and $h=H/\lambda_1\lambda_2$ explicitly, we rewrite the force balance equations (3.5) and (3.6) as,

$$\frac{d\alpha}{dX}=-\frac{\sigma_2\lambda_1\sin\alpha}{\sigma_1\lambda_2 X}+\frac{p\lambda_1^2\lambda_2}{\sigma_1 H}, \tag{3.13}$$

$$\frac{d\lambda_1}{dX}=\left(X\frac{\partial}{\partial\lambda_1}\left(\frac{\sigma_1}{\lambda_1}\right)\right)^{-1}\left[\frac{\sigma_2}{\lambda_2}\cos\alpha-\frac{\sigma_1}{\lambda_1}-\frac{\partial}{\partial\lambda_2}\left(\frac{\sigma_1}{\lambda_1}\right)\left(\lambda_1\cos\alpha-\lambda_2\right)\right]. \tag{3.14}$$

The force balance equations (3.13) and (3.14), together with the geometric relations (3.1) and (3.2), form a set of first-order differential equations that govern the inhomogeneous deformation of the DE membrane. Using the constitutive model in Eqs. (3.9)-(3.12) and the definition of the latitudinal stretch in Eq. (3.2), the right hand side of the governing equations (3.1), (3.2), (3.13) and (3.14) can be expressed as functions of $x(X)$, $z(X)$, $\lambda_1(X)$ and $\alpha(X)$. The boundary conditions for the DE membrane mounted over an air chamber are prescribed on the apex and the edge of the membrane,

$$x(0)=0, z(0)=0, \alpha(0)=0 \tag{3.15}$$

$$x(R_0)=R_0. \tag{3.16}$$

Together with the boundary conditions (3.15) and (3.16), the inhomogeneous deformation of the DE membrane subjected to different pressures and voltages can be obtained.

3.3 Numerical computation of inhomogeneous deformation of the DE membrane

In this section, we conduct numerical calculations to obtain all equilibrium configurations of the DE balloon under the actions of internal pressure and electric voltage, which are governed by the equations formulated in Section 2.

The set of first order differential equations (3.1), (3.2), (3.13) and (3.14) can be solved numerically by shooting method. Except for the boundary values at the apex: $x(0)=0$, $z(0)=0$, and $\alpha(0)=0$, an value of $\lambda_1(0)=\lambda_a$ is assigned as an additional boundary condition. Those values are used as initial conditions and numerically integrated in Eqs. (3.1), (3.2), (3.13) and (3.14) to obtain the values of $x(X)$, $z(X)$, $\lambda_1(X)$ and $\alpha(X)$. The value of λ_a is continuously varied until the boundary condition at the edge, $x(R_0)=R_0$, is satisfied.

In Fig. 3.3, we plot the relation between internal pressure and volume of the DE balloon in equilibrium state with different applied voltages. Pressure, volume and electric voltage are scaled to the dimensionless forms as $pR_0/\mu H$, V/R_0^3 and $\Phi\Big/\left(H\sqrt{\mu/\varepsilon}\right)$, respectively. The pressure vs. volume diagram of the balloon remains an N-like shape, when the normalized voltage is less than 0.145, similar to the traditional hyperelastic balloon only subjected to pressure [80, 81, 83, 84, 148]. If the internal pressure of the balloon is controlled in experiments, when the internal pressure is increased to the first pressure peak in the pressure vs. volume curve: $p_{\max}$, further increase of the pressure will make the DE balloon discontinuously jump from one state with small volume to another state with large volume through snap-through instability. Similarly, when the internal pressure is decreased to the first valley in the pressure vs. volume curve: $p_{\min}$, further decrease of the pressure will make the DE balloon discontinuously jump from a large volume to a small volume. Such snap-through instability has already been widely observed in different experiments. As the normalized voltage exceeds 0.145, additional equilibrium configurations can be obtained in the descending path of pressure vs. volume curve of the balloon as shown in Fig. 3.3. Consequently, for a certain range of pressure, five different equilibrium states of a DE balloon are found. This is different from the shape bifurcation in a spherical DE balloon, where a non-uniform deformation branch bifurcates from a homogenously deformed state [84, 145].

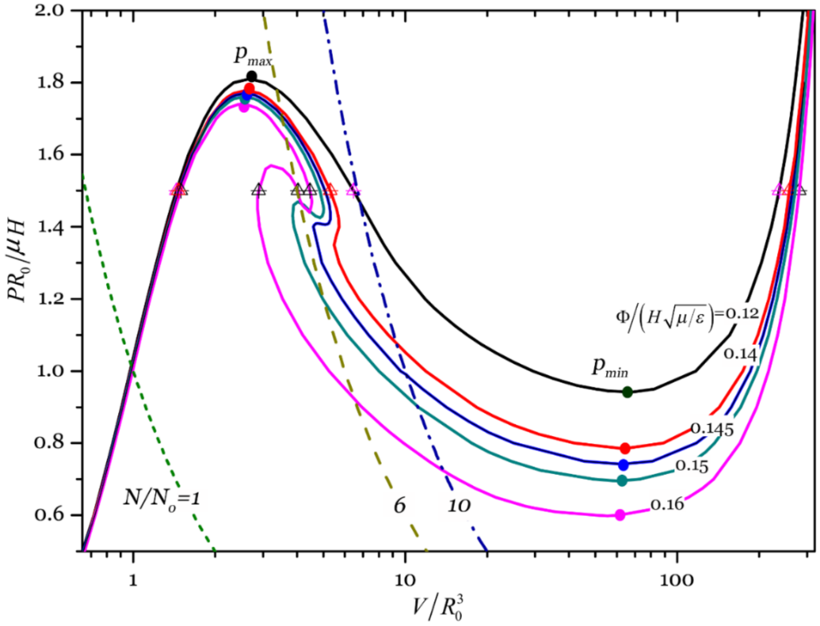

Figure 3.3: Pressure vs. volume curve of a DE balloon under several different applied voltages. When the voltage $\Phi/\left(H\sqrt{\mu/\varepsilon}\right)$<0.145, the pressure-volume relationship is represented by an N-like curve. When the voltage $\Phi/\left(H\sqrt{\mu/\varepsilon}\right)$>0.145, a new instability mode of the DE balloon emerges. For a certain range of pressure, five different equilibrium states can be found in the balloon with different volumes. The triangles mark the equilibrium configurations of the DE balloon under the normalized pressure: $pR_0/\mu H$=1.5. The dash lines describe the state equation of ideal gas under three different amounts of air enclosed in the balloon (N/N_0=1, 6 and 10), where N_0 is the amount of air molecule when pressure and volume are unity.

We further visualize the deformed shapes and electric field in the DE balloons in Fig. 3.4. As marked by triangles in the pressure vs. volume curve of the balloon in Fig. 3, the DE balloons are inflated by an internal pressure: $pR_0/\mu H$=1.5 and the electric voltages $\Phi/\left(H\sqrt{\mu/\varepsilon}\right)$ ranging from 0.12~0.16. For the voltage smaller than 0.145, there are three equilibrium configurations under certain pressures. The different shapes of the balloon under the same pressure and voltage have significantly different volumes, which is attributed to the snap-through instability discussed previously. With the increase of the volume, the membrane of the balloon thins down drastically in most part of the balloon, generating a high electric field. By increasing the voltage from 0.12 to 0.14, the deformed shapes of the DE balloons are similar, with only an increase in the volume and the electric filed. However, when the voltage is increased to 0.16, in addition to the deformed shapes observed at lower voltages, two additional configurations emerge. As shown in the third row of Fig. 4, when the applied voltage is 0.16, the first, fourth and fifth configurations of the DE balloon are similar to the lower voltage cases. The second and third configurations of the balloon in the row show different shapes, with localized bulging-out formed around the apex of the balloon, which are similar to what were observed in the experiments (Fig. 1c and 1b). After forming the localized bulging-out, the volume of the DE balloon decreases compared to the counterpart without the bulging-out, but the electric field at the apex increases dramatically as the membrane thins down greatly. The generation of high electric field accompanied with the formation the bulging-out makes the DE balloon susceptible to electrical breakdown [79, 145].

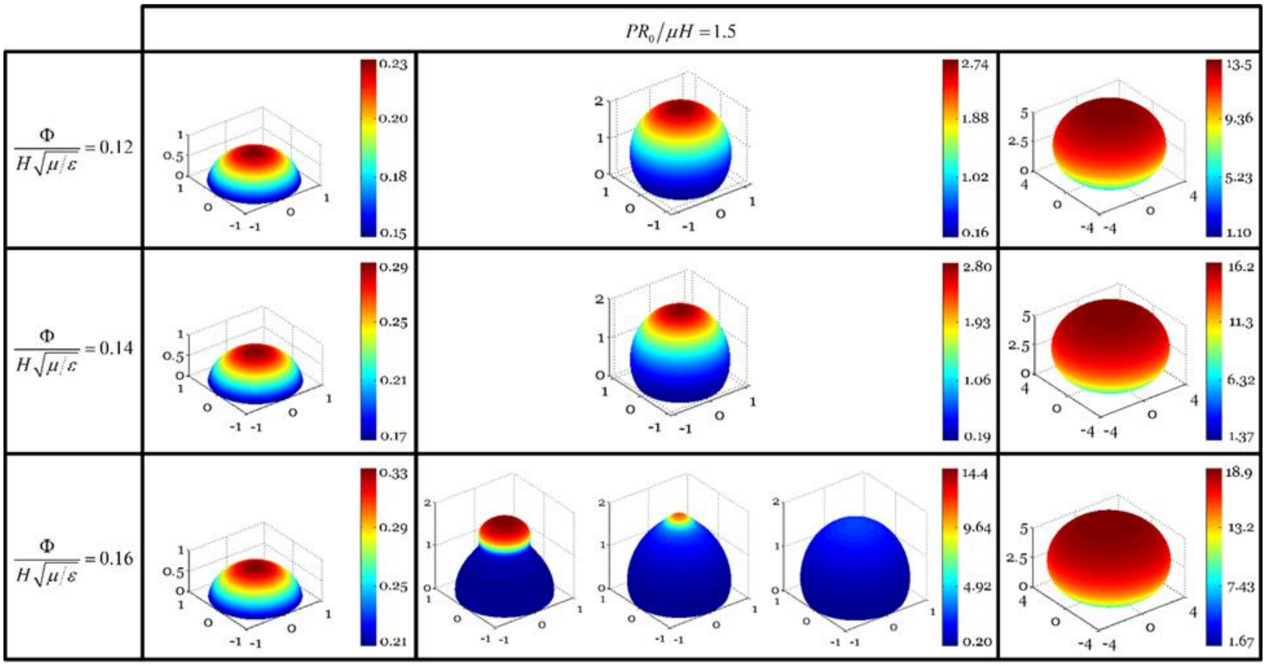

Figure 3.4: Deformed shapes and electrical fields in the DE balloons under pressure $pR_0/\mu H$=1.5. The equilibrium states of the DE balloons are marked with triangles in Fig. 3.3 and arranged by volume (from small to large) in each row. The color stands for the dimensionless true electric field, $E/\sqrt{\mu/\varepsilon}$.

Although the balloon with a bulging-out around its apex is an equilibrium state as shown in Figure 3.4, it cannot be easily achieved in the experiment with pressure-controlled loading condition [79, 80, 89, 92]. When the internal pressure reaches the first peak $p_{\max}$ in the pressure vs. volume curve of the balloon, further increase of internal pressure will result in snap-through instability of the balloon as described previously. To reach the equilibrium configurations of the balloon in the descending path of the pressure vs. volume curve, different loading paths need to be adopted in the experiment. As described in the paper [79], the new instability mode of the balloon can be observed when the applied voltage is increased while the total amount of air enclosed by the balloon is fixed. To obtain the relation between the applied and the volume of the balloon, we simply need to introduce the ideal gas law as the state equation of the enclosed air:

$$Nk_B T = \left(p + p_{atm}\right)\left(V + V_c\right), \tag{3.17}$$

where p is the excessive internal pressure of the enclosed air in the balloon relative to the atmospheric pressure p_{atm}, V and V_c are the volume of the balloon and the air chamber, respectively, N is the number of the gas molecule, k_B is the Boltzmann constant and T is the temperature. The amount of the air molecules in the chamber and balloon is fixed after the valve is closed in the experiment, and it is scaled as N/N_0, where N_0 is the number of molecules when dimensionless pressure and volume are unity.

Without losing generality, we assume the deformation of the balloon is isothermal, the volume of the chamber V_c=0 in the following analysis. By selecting different amount of air enclosed in the balloon, the curves describing the state equation of ideal gas (Eq. (3.17)) are sketched as dash lines in Fig. 3.3. The crossing points between the curves describing the state equation of ideal gas and the pressure vs. volume curves of the DE balloon represent the equilibrium configurations of the DE balloon with certain amount of enclosed air. By selecting the crossing points, we can obtain the relations between the applied-voltage vs. volume of the DE balloons with fixed amount of enclosed air as plotted in Fig. 3.5. For a small amount of enclosed air (N/N_0=1), the excessive internal pressure p is smaller than the first pressure peak p_{max} in the pressure vs. volume curve. The balloon is slightly inflated and relatively stiff toward expansion. Consequently, increase of the applied voltage results in a small change of balloon volume. For a large amount of air (N/N_0=10), the curve describing the state equation of ideal gas also only intersects with the pressure vs. volume curve of the DE balloon at one point for one applied voltage.

However, the stiffness of DE balloon decreases a lot with a large volume. A small increase of voltage can result in large volume change of the balloon as shown in Fig. 3.5, which was also demonstrated in the experiments [79, 92]. For an intermediate amount of enclosed air with N/N_0=6, the curve describing the state equation of ideal gas may intersect with pressure vs. volume curves of the balloon at multiple points for a given voltage. In another word, for a fixed amount of enclosed air and applied voltage, multiple equilibrium states of the balloon may exist. We plot several deformed shapes and electric field in the DE balloons with varied loading conditions (A~D) in the inset of Fig. 3.5. To determine if any configurations of the DE balloon is stable or not, perturbation analyses are necessary, which is beyond the scope of the current article.

Last, we compared the electric breakdown field of the material to the true electric fields in the DE balloon of different shapes. It is apparent that if the bulging-out shape of the DE balloon is physically realizable, the maximum electric field in the balloon has to be lower than the electric breakdown field of the DE material. Given that the DE material used in the experiment [79] was VHB^{TM} 4910, we use the following representative values of shear modulus μ=10~45 *kPa*, the dielectric constant ε=4.16×10^{-11} *F/m* and the electric breakdown field E_B=2.18×10^8 *V/m* [147, 149, 150]. The dimensionless electric breakdown field can be estimated as $E_B \big/ \sqrt{\mu/\varepsilon} = 6.7 \sim 10$. The maximum electric field in some DE balloons with bulging-out configurations shown in Fig. 3.4 and inset of Fig. 3.5 are slightly smaller than or comparable to the electric breakdown field. This is consistent with the experimental observations that the formation of localized bulging-out often quickly results in the failure of the material [79].

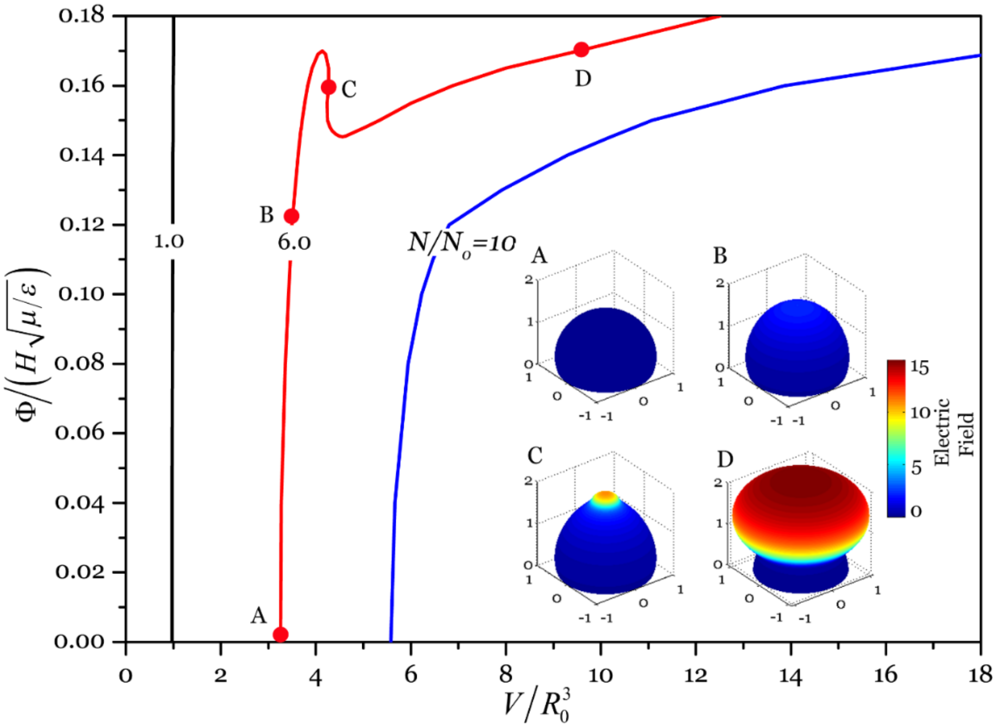

Figure 3.5: Voltage vs. volume curve for the DE balloon with different amounts of enclosed air. The number of air molecule N is normalized by N_0, which is the number of molecule when the normalized pressure and volume are unity. The voltage-volume relation is monotonic for small (N/N_0=1) and large (N/N_0=10) amount of air, while non-monotonic for N/N_0=6. The deformed shapes and electric field with varied loading conditions (A~D) in the DE balloon are plotted in the inset.

3.4 Effects of prestretches and stretching limit on the new instability modes

Actuating behavior of DE can be greatly affected by its prestretches [151-155]. In particular, electromechanical instability in a DE membrane can be delayed or even eliminated by applying prestretches. Consequently, for most applications of DE devices, prestretches are often applied onto the material. In this section, we first study the effects of prestretches in the DE membrane on the new bulging-out instability modes of the DE balloon.

As shown in the inset of Fig. 3.6, the DE membrane is of flat circular shape with radius R_0 in the reference state, and is prestretched equal-biaxially and held by a rigid ring before actuation. The pressure vs. volume curves of equilibrium states of a DE balloon are shown in Fig. 6 with prestretch λ_p=2. By comparing Fig. 3.6 with Fig. 3.3, we can clearly see the effects of prestretches on the actuation behavior of a DE balloon. With the applied prestretch, when the dimensionless voltage $\Phi/\left(H\sqrt{\mu/\varepsilon}\right)$<0.14, the internal pressure applied to the balloon increases monotonically with its volume; no snap-through instability is expected, which is in direct contrast to the results shown in Fig. 3.3. When 0.14<$\Phi/\left(H\sqrt{\mu/\varepsilon}\right)$<0.17, the pressure vs. volume relationship becomes non-monotonic. For such a range of voltage, a DE balloon can undergo snap-through instability as it jumps from one state to another at the local maximum or minimum pressures ($p_{\max}$ and $p_{\min}$). However, the volume change of a DE balloon is much smaller than the one without prestretch as shown in Fig. 3.3. The additional configurations, which correspond to the localized bulging-out, only appear when $\Phi/\left(H\sqrt{\mu/\varepsilon}\right)$ is further increased to 0.17. The emergence of the new instability mode with bulging-out shape requires a higher voltage when prestretches are applied. Consequently, the DE material is prone to electric breakdown due to the application of prestretch. Therefore, our results show that prestretches can be used to tune the critical voltages for both snap-through instability and the emergence of the bulging-out instability modes of a DE balloon subject to electromechanical loading.

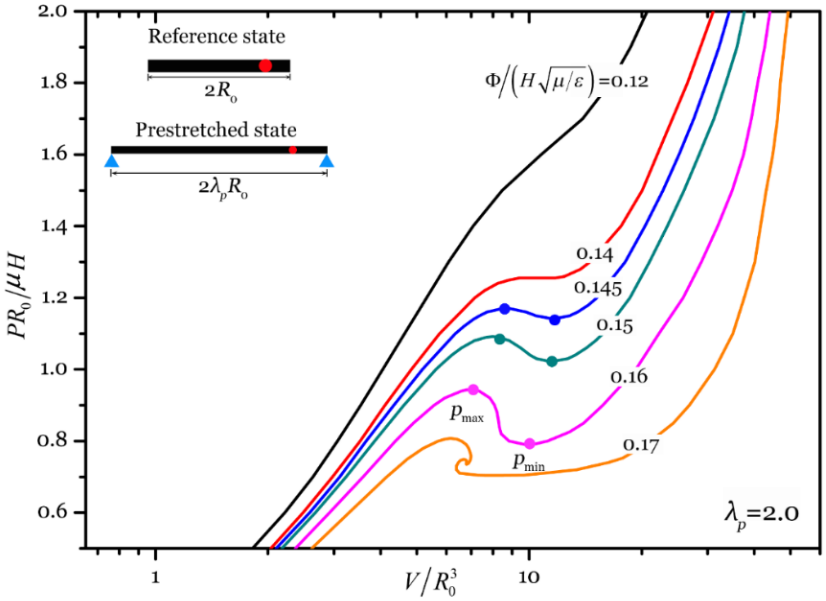

Figure 3.6: Pressure vs. volume curves of a DE balloon with prestretch λ_p=2.0 as shown in the inset. Both snap-through and localized bulging out instability modes are delayed by prestretches on the DE membrane. For dimensionless voltage $\Phi/\left(H\sqrt{\mu/\varepsilon}\right)<0.14$, the pressure increases monotonically with the volume. For $0.14<\Phi/\left(H\sqrt{\mu/\varepsilon}\right)<0.17$, the pressure vs. volume curves remain N-shape, with three equilibrium configurations within a range of pressures. For $\Phi/\left(H\sqrt{\mu/\varepsilon}\right)=0.17$, two additional configurations emerge as the localized bulging-out configurations for certain pressures.

Different hyperelastic models have been used in DE model to interpret different experimental results [79, 145, 147, 156]. Even with the same hyperelastic model, different material parameters have been adopted. For example, recent experimental measurements of acrylic elastomer (VHB$^{\text{TM}}$ 4910) which is used in the referred experiments [79], revealed a stretching limit λ_{lim}~9.0 under quasi-static (low stretch-rate), monotonic simple tension test [147], corresponding to the value of J_{lim}=97.2 in Gent model. The value of J_{lim} is much smaller than the one used in the previous studies [79] and the aforementioned numerical computation (J_{lim}=270). Therefore, in the section, we next study the effects of material parameter J_{lim} on the actuating behavior of DE balloon.

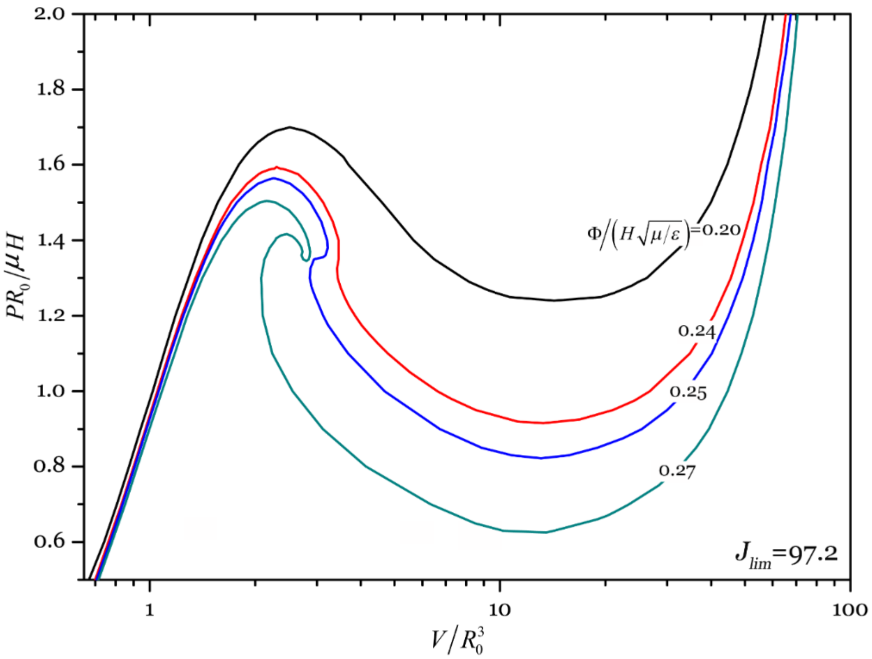

Figure 3.7: Pressure vs. volume curves of a DE balloon with smaller stretch limit as J_{lim}=97.2. When the voltage $\Phi/\left(H\sqrt{\mu/\varepsilon}\right)$<0.25, the pressure-volume relationship is represented by an N-like curve. When $\Phi/\left(H\sqrt{\mu/\varepsilon}\right)$>0.25, new instability modes with bulging-out of the DE balloon emerge. The voltage required for the emergence of the bulging-out instability mode increases when J_{lim} of the elastomer is reduced from 270 to 97.2.

An elastomer with smaller value of J_{lim} shows stiffening effect at smaller stretches. To reveal the effects of J_{lim} on the actuating behavior of a DE balloon, we carried out simulations with J_{lim}=97.2 and compared the results to the one with J_{lim}=270. As shown in Fig. 3.7, the pressure vs. volume curves of a DE balloon share a similar shape under pressure and electric field as shown in Fig. 3.3. When the voltage is lower than a critical value (~0.25), the pressure-volume curve remains an N-shape curve; when voltage is higher than the critical value, two additional configurations emerge with the localized bulging-out for certain pressure. Similar to the effect of prestretch, reducing the value of J_{lim} also increases the voltage for triggering the bulging-out instability mode.

3.5 Non-convex free energy and new instability modes in DE balloon

For an elastomeric balloon, the relationship between its internal pressure and volume can be usually represented by an N-like curve [81, 88, 148], which often results in snap-through instability of the balloon in experiments [80, 89]. Such a non-monotonic relationship between the internal pressure and volume of a balloon is due to its large and nonlinear deformation instead of any special constitutive model of the elastomer. Explicitly speaking, strain energy density functions of an elastomer given by different constitutive models are typically convex [23, 148]. As a result, similar N-like curves between the pressure and volume have also been theoretically predicted [79, 142] and experimentally validated [79, 92] for a DE balloon subjected to a constant voltage across its thickness.

However, it is known that free energy density function of a DE membrane may become non-convex when the applied voltage is high, which can lead to electromechanical instability of a DE membrane with homogenous deformation [120, 157]. We believe the additional instability modes of the DE balloon observed in the experiment and captured by our numerical computation in Section 3 are due to the non-convexity of the free energy density function of the DE membrane when the applied voltage is high.

The convexity of free energy density function of a DE membrane can be assessed by computing its Hessian. Based on ideal dielectric elastomer model, free energy density function of a DE membrane can be written as [23, 120],

$$W(\lambda_1, \lambda_2, \tilde{D}) = W_s(\lambda_1, \lambda_2) + \frac{\tilde{D}^2}{2\varepsilon\lambda_1^2\lambda_2^2}, \tag{3.18}$$

where $W_s(\lambda_1,\lambda_2)$ is the strain energy density of the elastomer given in Eq. (3.11) and $\tilde{D}$ is nominal electric displacement, namely, $\tilde{D} = dQ/dA$, where dA is the area of an element in the undeformed state and dQ is the amount of charge over the area on each side of the element. Convexity of the free energy density function in Eq. (3.11) is determined by its Hessian, which can be calculated as,

$$\mathbf{H} = \begin{bmatrix} \frac{\partial^2 W(\lambda_1,\lambda_2,\tilde{D})}{\partial \lambda_1^2} & \frac{\partial^2 W(\lambda_1,\lambda_2,\tilde{D})}{\partial \lambda_1 \partial \lambda_2} & \frac{\partial^2 W(\lambda_1,\lambda_2,\tilde{D})}{\partial \lambda_1 \partial \tilde{D}} \\ \frac{\partial^2 W(\lambda_1,\lambda_2,\tilde{D})}{\partial \lambda_2 \partial \lambda_1} & \frac{\partial^2 W(\lambda_1,\lambda_2,\tilde{D})}{\partial \lambda_2^2} & \frac{\partial^2 W(\lambda_1,\lambda_2,\tilde{D})}{\partial \lambda_2 \partial \tilde{D}} \\ \frac{\partial^2 W(\lambda_1,\lambda_2,\tilde{D})}{\partial \tilde{D} \partial \lambda_1} & \frac{\partial^2 W(\lambda_1,\lambda_2,\tilde{D})}{\partial \tilde{D} \partial \lambda_2} & \frac{\partial^2 W(\lambda_1,\lambda_2,\tilde{D})}{\partial \tilde{D}^2} \end{bmatrix}. \tag{3.19}$$

The free energy density function of DE is convex if the Hessian is positive definite. The free energy density function of DE becomes non-convex when the Hessian is not positive definite, and multiple equilibrium states can coexist [23]. To determine whether the Hessian is positive definite or not, we calculate the eigenvalues of the Hessian. Following linear algebra, we can easily show that the critical condition for the free energy density function of the DE becoming non-convex is that the smallest eigenvalue of **H** is zero, namely,

$$\alpha_1(\lambda_1,\lambda_2,\tilde{D}) = 0, \tag{3.20}$$

where α_1 is the smallest eigenvalue of **H**. The solution of Eq. (3.20) can be rewritten as

$$\tilde{D} = f(\lambda_1,\lambda_2), \tag{3.21}$$

which can be illustrated in a two dimensional contour plot. The nominal electric displacement and applied voltage is linked by the equation, $\tilde{D} = \varepsilon \lambda_1^2 \lambda_2^2 \Phi / H$, which directs to the equivalent expression of Eq. (3.21) as $\Phi = g(\lambda_1, \lambda_2)$. Consequently, the critical condition for the free energy density function of a DE to be non-convex can be given by a stretched state for a given voltage. Each curve represents a contour of non-positive-definite Hessian, along which the function $\Phi = g(\lambda_1, \lambda_2)$ has a constant value. As shown in Fig. 3.8, the global minimum of the contour plot stays at the voltage: $\Phi_{\min} = 0.123H\sqrt{\mu/\varepsilon}$ for J_{lim}=270, which correspond to the stretched state of λ_1=1.1 and λ_2=11.6 (or λ_1=11.6 and λ_2=1.1); $\Phi_{\min} = 0.2085H\sqrt{\mu/\varepsilon}$ for J_{lim}=97.2, which correspond to the stretched state of λ_1=1.14 and λ_2=7.1 (or λ_1=7.1 and λ_2=1.14). When the applied voltage $\Phi < \Phi_{\min}$, the free energy density function of the DE is convex for any deformation state, and a DE balloon behaves like a hyperelastic balloon only subjected to internal pressure. When the applied voltage is larger than $\Phi_{\min}$, the free energy density function of DE becomes non-convex for certain deformation states and the abnormal bulging-out shape might be formed.

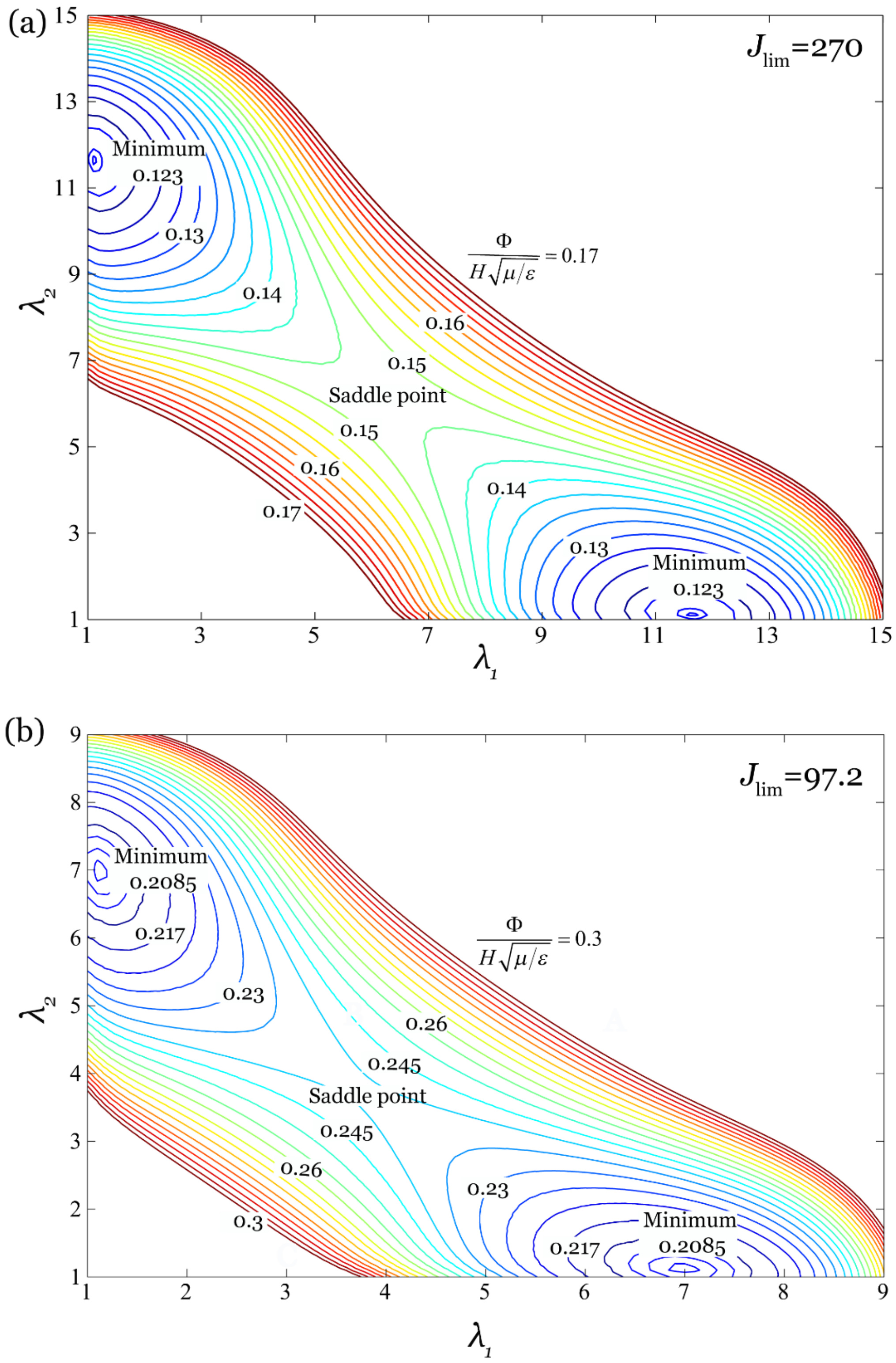

Figure 3.8: Contours of critical voltage for the non-convex free energy density of DE under different values of J_{lim} in the hyperelastic material model: (a) J_{lim}=270 and (b) J_{lim}=97.2.

It is noted that in this article, we do not intend to precisely predict the onset of the newly observed bulging-out instability by evaluating Hessian, which is only valid for predicting critical conditions for instability with homogeneous deformation [23, 106]. To predict onset of instability of a structure with inhomogeneous deformation or other fields, perturbation analyses may be required [84, 106, 145, 158]. In the chapter, we would like to propose that the additional bulging-out instability modes of the DE balloon are associated with its non-convex free energy density function of DE at high voltage.

3.6 Concluding remarks

In this article, we have studied new instability modes in a DE balloon subjected to internal pressure and electric voltage. By numerically solving the governing equations, we obtain the equilibrium configurations of a DE balloon under different internal pressures and voltages. We find out that when the applied voltage is small, the pressure vs. volume diagram of a DE balloon can be represented by an N-like curve, which is similar to the conventional hyperelastic balloon problem; when the voltage is larger than a critical value, new instability modes in the balloon emerge, which have an abnormal localized bulging-out, similar to the shape observed previously [79]. Based on our numerical calculations, we show that the bulging-out modes recently observed in a DE balloon can be an equilibrium configuration. Such a bulging-out shape does not rely on any specific material or geometrical defects. In addition, the prediction of the bulging-out configuration does not require any modifications of the DE balloon model. We further show that the DE balloon with a bulging-out shape can be realized in the experiment by gradually increasing the applied voltage while fixing the total amount of air enclosed in the balloon. We believe the bulging-out instability modes of a DE balloon are related to the non-convexity of the free energy density function of DE when the applied voltage is high. We finally show that prestretch as well as the material parameter (J_{lim}) can affect the voltage required for triggering the emergence of the bulging-out instability of a DE balloon.

Chapter 3, in full appears in the paper “"New electromechanical instability modes in dielectric elastomer balloons”, *International Journal of Solids and Structures* (2017), by X. Liang and S. Cai. The dissertation author was the primary investigator and author of this paper.

Chapter 4 Creasing of an everted elastomer tube

A cylindrical elastomer tube can stay in an everted state without any external forces. If the thickness is small, an everted tube, except for the regions close to its free ends, maintains cylindrical shape; if the thickness is larger than a critical value, cross-section of the everted tube becomes noncircular, which is caused by mechanical instability. Although eversion-induced mechanical instability in an elastomer tube has been reported several decades before, a satisfying explanation of the phenomenon is still unavailable. In previous studies, linear or weakly nonlinear analyses have been usually adopted to predict the critical thickness of the tube for the eversion-induced instability. The discrepancy between the prediction and experiment is significant. In this article, based on experiments and theoretical analyses, we show that crease formation on the inner surface of an everted tube is the mechanical instability mode, which cannot be captured by linear stability analyses. Instead, a combination of energetic analyses and numerical simulations of finite deformation in an everted tube enables us to correctly predict both critical tube thickness for the onset of creases and profile of the noncircular cross-section of an everted tube with large thickness.

4.1 Introduction

Turning a structure inside out, often called eversion, is ubiquitous in nature and also frequently used in different fabrication processes. For example, during the development of *Volvox* embryo, a spherical monolayer cell sheet folds itself inside out to trigger the formation of an internal cavity and achieves the adult configuration in morphogenesis [159]. The eversion of jellyfish, known as ‘Jellyfish syndrome’, is a self-defense mechanism to protect itself from environmental changes [160, 161]. The stent eversion has been used to construct an autologous heart valve, known as the stent-bi0valve [162]. The carotid endarterectomy in surgery by everting the internal carotid artery is a way to preserve the neurological function [163]. Due to its profound influence in nature and various engineering applications, eversion of 3D objects has been a topic of significant interest for a large group of researchers for several decades [164-172].

Finite deformation is often involved in the eversion of various structures [171]. Deformation of an everted elastomeric tube has been one of the most classical finite deformation problems since Rivlin [171] first proposed it. Varga [167] has shown that in experiments, except for the regions close to the two free ends of the tube, after eversion, most part of the tube is very close to be cylindrical shape. Chadwick and Haddon [168] have investigated the conditions for the existence and uniqueness of the solutions associated with cylindrical tube eversion of hyperelastic materials. Ericksen [169] and Antman [170] further extended the results to the eversion of spherical shells.

However, an experimental phenomenon associated with the tube eversion, first described by Truesdell [173], has not been well explained for several decades. Truesdell discovered in his experiments that the cross-section of an everted cylindrical tube became noncircular when the tube thickness is large. To explain the observation quantitatively, both linear stability analyses [164, 165] and weakly nonlinear analyses [166] of tube eversion have been conducted. These analyses have shown that when the tube thickness is larger than a critical value, axisymmetric deformation of an everted tube is not stable anymore and wrinkles may appear on the inner surface of the tube after eversion. Nevertheless, as pointed out in many of these articles [164-166], the critical thickness of the tube predicted by the analyses is significantly larger than the tube thickness in Truesdell's experiments. The well-known discrepancy between the predictions and experiments has not been resolved until now.

In the present chapter, we investigate mechanical instability in an everted cylindrical tube. The theory of finite elasticity and Neo-Hookean material model are adopted in the analyses. Inspired by recent studies on the surface instabilities of elastomers with large deformation [95, 97], we will calculate the critical conditions for both wrinkling and creasing in an everted tube. Specifically, we use linear perturbation method [67] to obtain the critical conditions of wrinkling instability in an everted tube. We combine numerical method and energetic analyses to model crease formation and post-creasing phenomena. In addition, we will compare our theoretical predictions of instability patterns in an everted tube with its micro-computer tomography (micro-CT) images. In this article, we will, for the first time, demonstrate that multiple creases, instead of wrinkles, can form on the inner surface of an everted tube when its thickness is larger than a critical value.

The organization of the chapter is as follows. Section 2 describes the experiment of eversion of a cylindrical elastomer tube. Section 3 formulates axisymmetric deformation of an everted tube. Numerical solutions of the equations are also given. In Section 4, we conduct a linear stability analysis of everted tubes and obtain the critical conditions associated with the wrinkling instability. We implement the nonlinear finite element simulation for the crease initiation and post-creasing in everted tubes in Section 5. We compare theoretical predictions with experimental measurements of everted tube with noncircular cross-sections in Section 6. Finally, Section 7 summarizes the main conclusions of the study.

4.2 Experiment of tube eversion

We fabricate elastomeric tubes of various sizes using homemade molds. The material of the tube is silicone rubber purchased from the company Smooth-on (USA), with Young's modulus around 150 kPa and uniaxial stretch limit around 10. In Fig. 4.1, we show the photos of cylindrical elastomer tubes with two different thickness before and after eversion. The thicknesses of the tubes in the undeformed state are 42% and 50% of their outer radius as shown in Fig.4.1a and 4.1b, respectively.

Both tubes can be everted manually without many difficulties. After the eversion, both tubes can reach a stable state without any detectable material damage or plastic deformation. For the thinner tube as shown in Fig. 4.1a, the inner surface of the tube in the everted configuration is smooth. For the thicker one in Fig. 4.1b, the inner surface of the everted tube is not smooth any more, as indicated by multiple shadow lines in the figure. The observations suggest that mechanical instability may happen in an everted tube with the thickness larger than a critical value, which is consistent with Truesdell's original experiments [173] described in the Introduction.

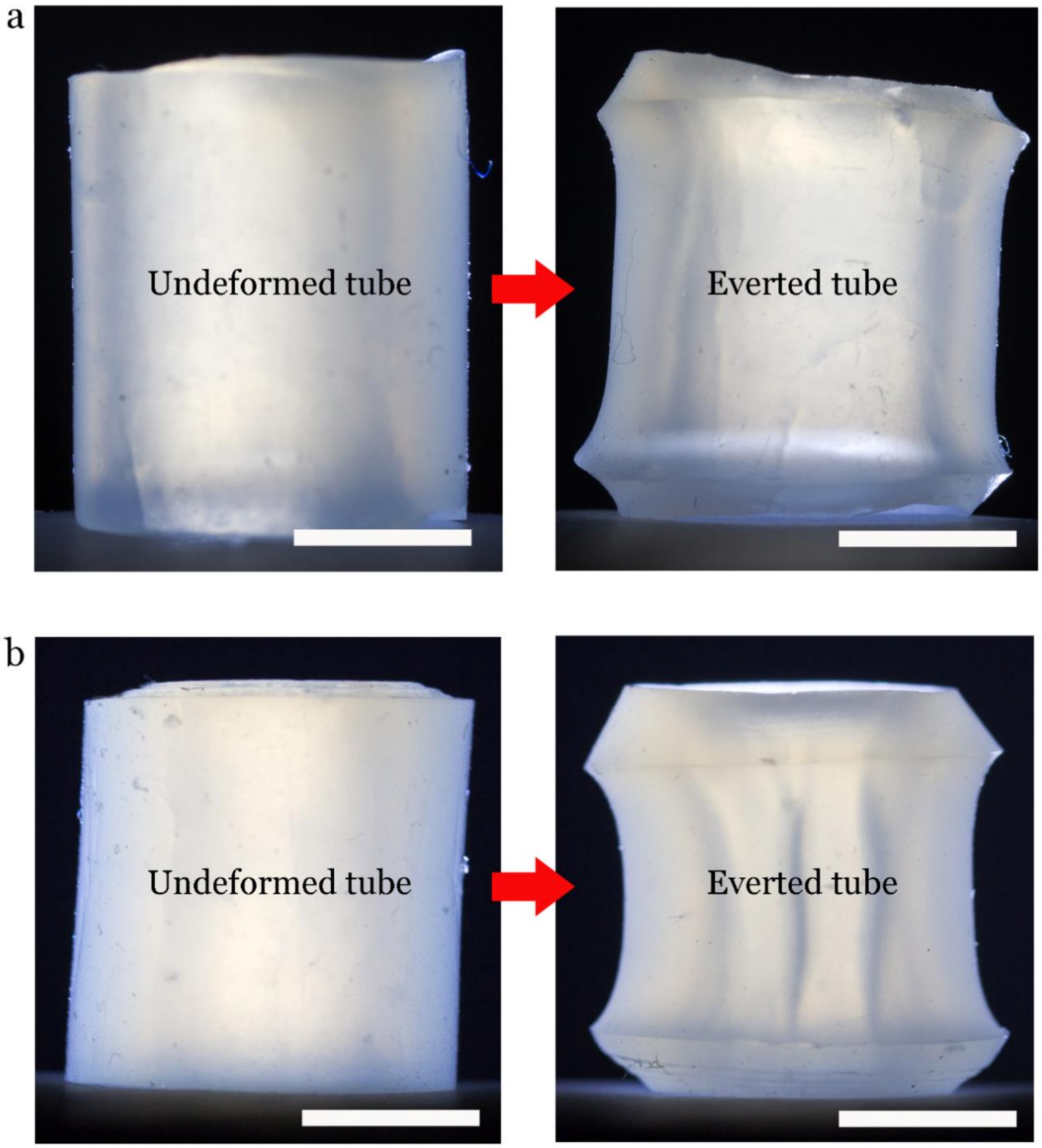

Figure 4.1: Crease formation on the inner surface of an everted elastomer tube. (a) If the thickness of the tube is small, after eversion, the inner surface of the tube is smooth; (b) If the thickness of the tube is larger than a critical value, multiple creases form on the inner surface of the everted tube. In the photos, the outer radius of the tube is 6mm, while thickness of the tube in (a) is 2.5 mm and in (b) is 3.0 mm. The length of the scale bar is 5mm.

4.3 Axisymmetric deformation of an everted tube

We first consider a homogenous cylindrical tube with an axisymmetric deformation field induced by the eversion as shown in Fig 4.1. We use the polar coordinate $\mathbf{X}=(R, \Theta, Z)$ to describe undeformed configuration of the tube and $\mathbf{x}=(r, \theta, z)$ for its deformed configuration. As illustrated in Fig. 4.2, the inner radius and outer radius of an undeformed cylindrical tube are denoted by A and B, respectively. The thickness of the undeformed tube is given by $H=B-A$. After the eversion, except for the regions close to the free ends of the tube, most part of the tube remains cylindrical shape with inner radius a and outer radius b. Previous studies [164] have shown that by neglecting the edge effect, the deformation of an everted tube can be described by the following fields,

$$r = r(R), \Theta = \theta, z = \lambda Z. \tag{4.1}$$

The principle stretches are given by $\lambda_r=dr/dR$ in the radial direction, $\lambda_\theta=r/R$ in the hoop direction and $\lambda_z=\lambda$ in the axial direction.

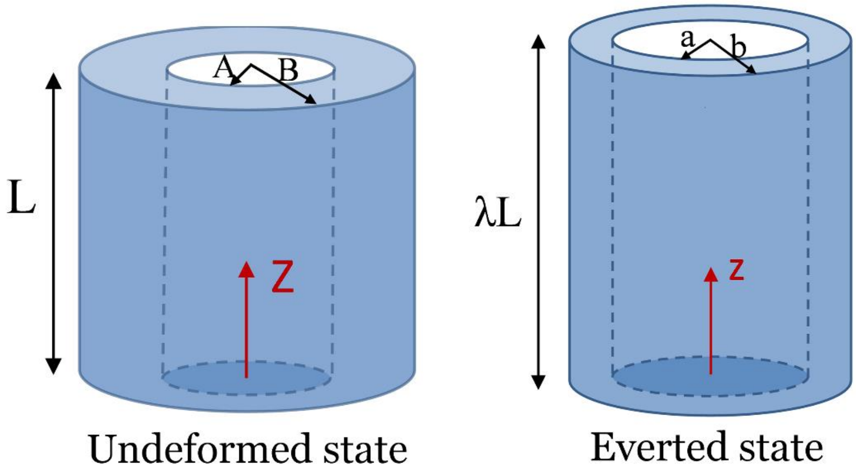

Figure 4.2: Schematics of a cylindrical tube in the undeformed state and everted state.

Following the literatures [164, 165], tube eversion can be regarded as a generalized plane strain problem, with homogenous stretch $\lambda_z=\lambda$ in the axial direction. After eversion, the inner surface of an undeformed tube becomes the outer surface of the tube in the everted state, and the outer surface of an undeformed tube becomes the inner surface of the tube in the everted state, namely,

$$r(A)=b,\ \ r(B)=a. \tag{4.2}$$

The elastomer is taken to be incompressible, so that we have,

$$B^2-R^2=\lambda(r^2-a^2). \tag{4.3}$$

The deformation field can be rewritten as,

$$r\left(R\right)=\sqrt{\left(B^2-R^2\right)/\lambda+a^2}. \tag{4.4}$$

When the axial stretch λ and the inner radius a in the deformed state are known, the deformation field of the everted tube $r(R)$ can be fully determined.

Based on Eq. (4.4), we can calculate the hoop stretch and radial stretch:

$$\lambda_\theta=\sqrt{\left(\left(B/R\right)^2-1\right)/\lambda+\left(a/R\right)^2}, \tag{4.5}$$

$$\lambda_r=1/\sqrt{\left(\left(B/R\right)^2-1\right)\lambda+\left(a\lambda/R\right)^2}. \tag{4.6}$$

With the assumption of axisymmetric deformation, force balance equation for an everted tube is given by,

$$\frac{d\sigma_{rr}}{dr}+\frac{\sigma_{rr}-\sigma_{\theta\theta}}{r}=0, \tag{4.7}$$

where σ_{rr} and $\sigma_{\theta\theta}$ are true stresses in the radial direction and hoop direction, respectively. The boundary condition for the everted tube is $\sigma_{rr}=0$ on the inner surface: $r=a$ and the outer surface: $r=b$. Following Rivlin [171], instead of requiring the normal stress to be zero on both ends of the tube, we relax the boundary condition to enforce the resultant force applied on the ends of the tube to be zero, namely, $\int_a^b r\sigma_{zz}dr=0$. As shown in the early experiments done by Varga [167], the edge effect in an everted tube only exists for the region with the distance of the tube thickness from its free ends.

We assume that the material of the tube can be described by incompressible Neo-Hookean model [174]. The true stress along the radial, the hoop and the axial directions of the tube can be given by,

$$\sigma_{rr}=\mu\lambda_r^2-p, \tag{4.8}$$

$$\sigma_{\theta\theta}=\mu\lambda_\theta^2-p, \tag{4.9}$$

$$\sigma_{zz}=\mu\lambda_z^2-p, \tag{4.10}$$

where μ is the small-deformation shear modulus of the elastomer and p is hydrostatic pressure. The material is assumed to be incompressible, so we have $\lambda_r\lambda_\theta\lambda_z=1$.

By plugging Eq. (4.8)–(4.10) into Eq. (4.7) and using the boundary condition $\sigma_{rr}=0$ at $r=a$, we can obtain,

$$p(r)=\frac{\mu\left(\lambda a^2-\lambda r^2+B^2\right)}{\lambda^2 r^2}+\frac{\mu(\lambda a^2+B^2)}{2\lambda^2}\left(\frac{1}{a^2}-\frac{1}{r^2}\right)+\frac{\mu}{\lambda}\ln\frac{aR}{Br}. \tag{4.11}$$

The boundary condition σ_{rr}=0 at $r=b$ can be rewritten as,

$$\frac{(\lambda a^2+B^2)}{2\lambda^2}\left(\frac{1}{a^2}-\frac{1}{b^2}\right)+\frac{1}{\lambda}\ln\frac{aA}{Bb}=0. \tag{4.12}$$

The relaxed boundary conditions of zero resultant force at the ends of the tube requires that,

$$\int_a^b\left(\frac{\lambda a^2-\lambda r^2+B^2}{\lambda^2 r}-\lambda^2 r-\int_a^b\left(\frac{(\lambda a^2-\lambda r^2+B^2)(b^2-r^2)}{2\lambda^2 r^3}-\frac{r(b^2-r^2)}{2(\lambda a^2-\lambda r^2+B^2)}\right)dr\right)dr=0. \tag{4.13}$$

The equilibrium solution of an everted tube can be numerically solved using shooting method. Because both the stress boundary conditions and stress balance equations are homogenous, the equations apparently have a trivial solution corresponding to the stress-free state. A nontrivial solution corresponds to the everted state of the tube with finite deformation. In the calculation, we continuously vary the axial stretch λ and inner radius a until the boundary conditions (4.12) and (4.13) are both satisfied. Once λ and a are known, the deformation field $r(R)$, radial stretch λ_r and hoop stretch λ_θ can be calculated using Eqs. (4.4)-(4.6). The axisymmetric deformation state of an everted tube without mechanical instability is obtained.

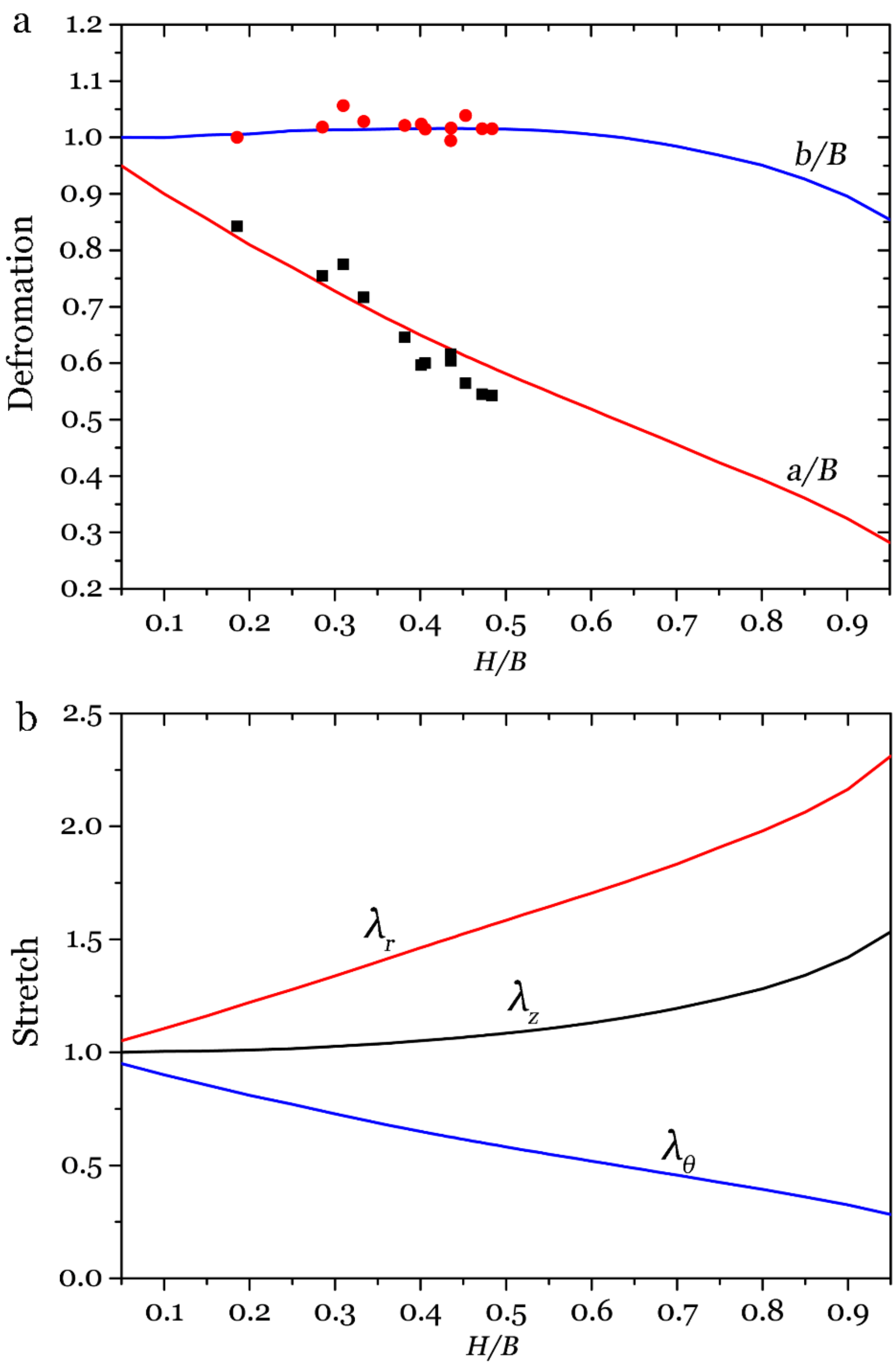

Figure 4.3: Distribution of the (a) inner and outer radius and (b) stretch in the everted tube with different thickness.

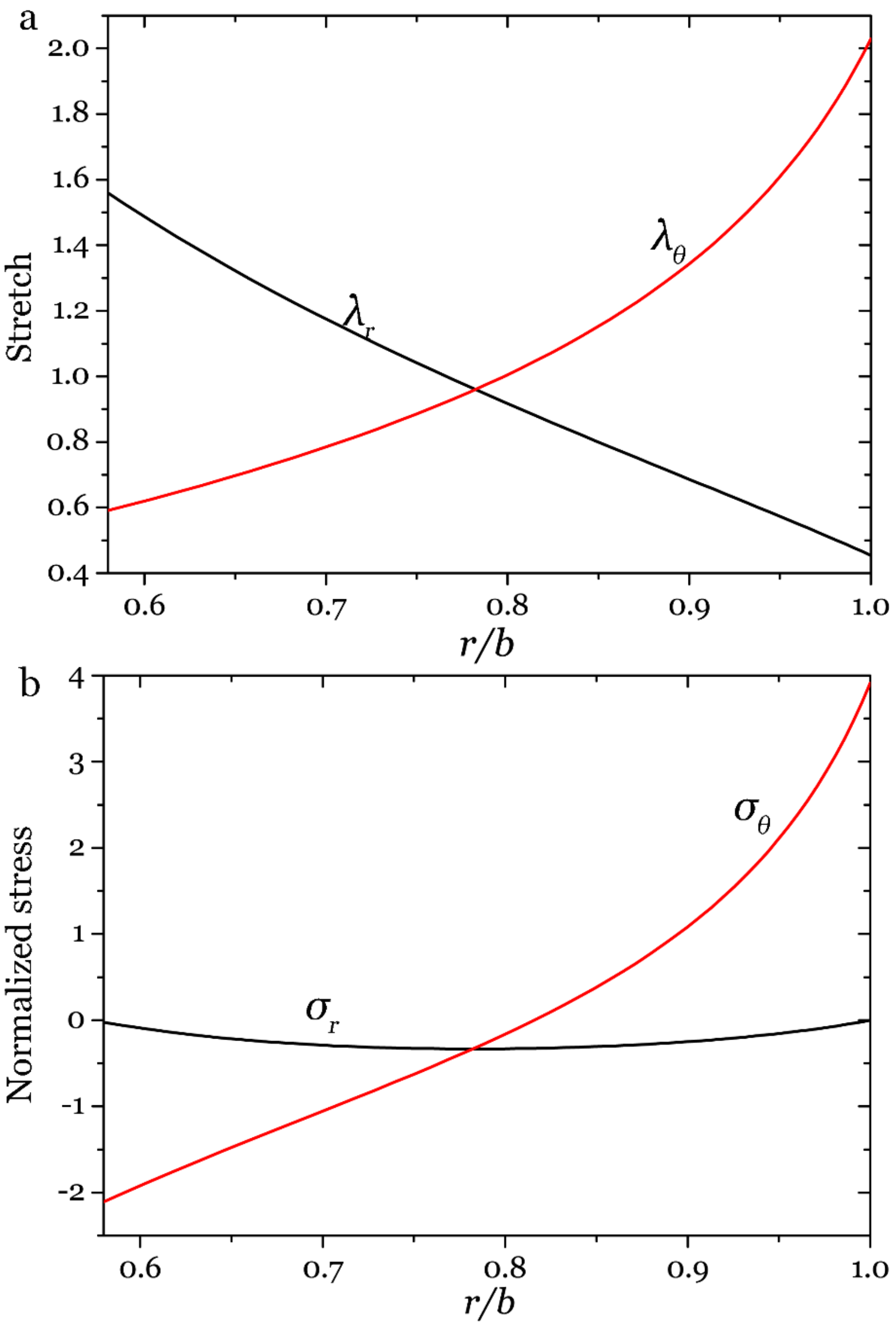

Figure 4.4: Distribution of (a) stretch and normalized stress along the radius of the everted tube with thickness of 0.5*B*.

In Fig. 4.3a, we plot the normalized inner radius a/B and the normalized outer radius b/B of the everted tube as functions of normalized thickness H/B. As thickness of the tube increases, the inner radius of the everted tube increases, while the outer radius of the everted tube increases when thickness is small and decreases when thickness is large. The comparisons between the experimental measurements and theoretical predictions of the inner and outer radius of the everted tube for $H/B<0.5$ are also presented in Fig. 4.3a. As we will show later, when the tube thickness of is large, mechanical instability may happen in the everted tube, which makes the axisymmetric deformation assumption not valid anymore.

In Fig. 4.3b, we plot the stretches of the inner surface of the everted tube in the radial, hoop and axial directions. Radial and axial stretches are always larger than one for different tube thickness. As a result of the material incompressibility, the hoop stretch of the inner surface is smaller than one.

The stretch and stress field along the radius of an everted tube with the thickness $H=0.5B$ are illustrated in Fig. 4.4. In the radial direction, the stretch λ_r decreases from the value larger than one on the outer surface to the value smaller than one on the inner surface. The radial stress σ_{rr} between the inner and outer surface of the tube is compressive. In the hoop direction, stress $\sigma_{\theta\theta}$ is compressive on the inner surface of the everted tube, which may result in surface instability shown in Fig. 4.1b.

4.4 Linear stability analysis

When the compressive stress in the hoop direction of an everted tube is sufficiently large, axisymmetric deformation of the tube caused by eversion is not stable anymore. Inner surface of an everted tube can significantly deviate from a circular shape as observed in Truesdell's original experiments [173]. As discussed in the introduction, wrinkling and creasing are two distinct but commonly observed surface instability modes in soft materials [93, 95, 97, 175]. Wrinkles can be usually characterized by a smooth undulation, while creases are characterized by singular regions of self-contact. Linear perturbation analysis is usually adopted to obtain the critical condition of wrinkling instability [67], while a combination of numerical simulation and energetic analyses has been used to study the crease formation [95, 98]. In this section, we first calculate the critical conditions for wrinkling instability of a tube after eversion.

Stretch and stress fields of an everted tube with axisymmetric deformation have been obtained in section 3. With the axisymmetric deformation, each material point of a tube in the undeformed state described by its coordinate **X**, moves to current coordinate $\mathbf{x}^{o}$ after the eversion. The deformation gradient can be calculated as,

$$F_{iK}^{0} = \frac{\partial x_i^0\left(\mathbf{X}\right)}{\partial X_K}. \tag{4.14}$$

To obtain the critical conditions for wrinkling instability of the elastomeric tube after eversion, we adopt linear perturbation analysis proposed by Biot [67]. The axisymmetric deformation filed of the elastomer $\mathbf{x}^{o}(\mathbf{X})$ is perturbed by a state of infinitesimal displacement $\mathbf{u}(\mathbf{x}^{o})$.

Using Neo-Hookean material model [174], we can obtain the corresponding perturbations of true stress as,

$$\tilde{\sigma}_{ij} = \mu F^0_{jK} F^0_{pK} L_{ip} + p^0 L_{ji} - \tilde{p}\delta_{ij}, \tag{4.15}$$

where $\tilde{\sigma}_{ij}$ and $\tilde{p}$ are the perturbations of true stress and hydrostatic pressure, p^0 is the hydrostatic pressure for the axisymmetric deformation, and $L_{ij} = \partial u_i / \partial x_j$.

The perturbations of true stress need to satisfy force balance equations, namely,

$$\frac{\partial \tilde{\sigma}_{ij}}{\partial x_j} = 0. \tag{4.16}$$

The incompressible condition expressed by the perturbation fields is,

$$L_{ii} = 0. \tag{4.17}$$

With the assumption of generalized plane strain condition, the perturbation of the displacement field can be given by,

$$\mathbf{u}(r,\theta) = u_r(r,\theta)\mathbf{e_r} + u_\theta(r,\theta)\mathbf{e_\theta}, \tag{4.18}$$

where the functions u_r and u_θ are the displacement perturbations in the radial and hoop directions, $\mathbf{e_r}$ and $\mathbf{e_\theta}$ are the corresponding unit base vectors, respectively. Consequently, the gradient of displacement perturbations are given by,

$$L_{rr} = \frac{\partial u_r}{\partial r}, L_{\theta\theta} = \frac{u_r}{r} + \frac{1}{r}\frac{\partial u_\theta}{\partial \theta}, L_{r\theta} = \frac{1}{r}\frac{\partial u_r}{\partial \theta} - \frac{u_\theta}{r}, L_{\theta r} = \frac{\partial u_\theta}{\partial r}. \tag{4.19}$$

The incompressible condition of Eq. (4.17) becomes,

$$\frac{\partial u_r}{\partial r} + \frac{u_r}{r} + \frac{1}{r}\frac{\partial u_\theta}{\partial \theta} = 0. \tag{4.20}$$

The stress perturbations $\tilde{\sigma}_{ij}$ in Eq. (4.15) takes the form,

$$\tilde{\sigma}_{rr} = \left(\mu\lambda_r^2 + p\right)L_{rr} - \tilde{p}, \tag{4.21a}$$

$$\tilde{\sigma}_{\theta\theta} = \left(\mu\lambda_\theta^2 + p\right)L_{\theta\theta} - \tilde{p}, \tag{4.21b}$$

$$\tilde{\sigma}_{r\theta} = \mu\lambda_\theta^2 L_{r\theta} + pL_{\theta r}, \tag{4.21c}$$

$$\tilde{\sigma}_{\theta r} = \mu\lambda_r^2 L_{\theta r} + pL_{r\theta}. \tag{4.21d}$$

The force balance equation Eq. (4.16) for stress perturbations can be expressed in the polar coordinate system as,

$$\frac{\partial \tilde{\sigma}_{rr}}{\partial r} + \frac{1}{r}\frac{\partial \tilde{\sigma}_{r\theta}}{\partial \theta} + \frac{\tilde{\sigma}_{rr} - \tilde{\sigma}_{\theta\theta}}{r} = 0, \tag{4.22}$$

$$\frac{\partial \tilde{\sigma}_{\theta r}}{\partial r} + \frac{1}{r}\frac{\partial \tilde{\sigma}_{\theta\theta}}{\partial \theta} + \frac{\tilde{\sigma}_{\theta r} + \tilde{\sigma}_{r\theta}}{r} = 0. \tag{4.23}$$

The boundary conditions for the stress perturbations are,

$$\tilde{\sigma}_{rr} = 0, \tilde{\sigma}_{\theta r} = 0, \tag{4.24}$$

for both *r=a* and *r=b*.

To determine the critical conditions for the wrinkling instability in the everted tube, we seek the existence of a non-trivial solution of the differential equations of Eqs. (4.22)-(4.24). By setting the perturbed displacement fields with the sinusoidal form,

$$u_r(r,\theta) = f(r)\cos\left(m\theta\right), \tag{4.25a}$$

$$u_\theta(r,\theta) = g(r)\sin\left(m\theta\right), \tag{4.25b}$$

$$\tilde{p}(r,\theta) = k(r)\cos\left(m\theta\right), \tag{4.25c}$$

where *f(r)*, *g(r)* and *k(r)* are real functions of variable *r* and *m* is the wave number of wrinkles.

Substituting Eq. (4.25) into (4.20)-(4.23), after elimination of *g*(*r*) and *k*(*r*) with *f*(*r*), we can obtain the following ordinary differential equation (ODE),

$$\begin{aligned}
&\frac{\mu R^2}{m^2\lambda^2} f^{IV} + \frac{2\mu(R^2 - 2\lambda r^2)}{m^2\lambda^2 r} f^{'''} - \left(\frac{p^{'} r}{m^2} + \frac{\mu((4+m^2)R^2 + 10\lambda r^2)}{m^2\lambda^2 r^2} + \frac{(m^2+1)\mu r^2}{m^2 R^2} \right) f^{''} \\
&- \left(\frac{p^{''} r}{m^2} + \frac{2}{m^2} p^{'} - \frac{\mu((4+m^2)R^2 + 2(m^2+2)\lambda r^2)}{m^2\lambda^2 r^3} + \frac{3\mu(m^2+1)rR^2 + 2\mu(m^2+1)\lambda r^3}{m^2 R^4} \right) f^{'} \\
&+ \left(\frac{\mu(m^4-1)}{m^2 R^2} + \frac{2\mu(m^2-1)\lambda r^2}{m^2 R^4} + \frac{m^2-1}{m^2} p^{''} \right) f = 0,
\end{aligned} \tag{4.26}$$

where both *r*(*R*) and *p*(*R*) are functions of *R*, which can be obtained from Eq. (4.4) and Eq. (4.11).

The boundary conditions given in Eq. (24) take the form,

$$\frac{R^2}{\lambda^2 m^2} f''' + \frac{2(R^2 - \lambda r^2)}{\lambda^2 m^2} f'' - \left(\frac{r^2}{R^2} + \frac{2R^2}{\lambda^2 r^2} + \frac{(R^2 + 2\lambda r^2)}{\lambda^2 m^2 r^2} \right) f' - \frac{\left(m^2 - 1\right)(R^2 + 2\lambda r^2)}{\lambda^2 m^2 r^3} f = 0, \quad (4.27)$$

$$r^2 f'' + r f' + (m^2 - 1) f = 0, \quad (4.28)$$

for both $r=a$ and b.

The differential equations Eq. (4.26) accompanied with the boundary conditions Eqs. (4.27)-(4.28) formulated an eigenvalue problem with loading parameter *H/B*, which determines the condition for the onset of wrinkles, and the associated eigenvectors describe the modes of wrinkling. It is difficult to solve the above eigenvalue problem analytically. Instead, we adopt compound matrix method [176] to solve the eigenvalue problems numerically.

The tube thickness for the onset of wrinkles as a function of its wavenumbers *m* defined in Eq. (4.25) is plotted in Fig. 4.5. We define H_{crit} as the smallest tube thickness for the onset of wrinkles with a critical wavelength m_{cirt} as shown by the red dot in Fig. 4.5. From the numerical calculations, we can conclude that the critical tube thickness for the wrinkling instability associated with eversion is H_{crit}=0.58*B*, with a wave number m_{cirt}=14. The critical thickness given by linear stability analysis is dramatically larger than the thickness of the tube shown in Fig.1b. This discrepancy implies other mechanical instability mode may happen during tube eversion.

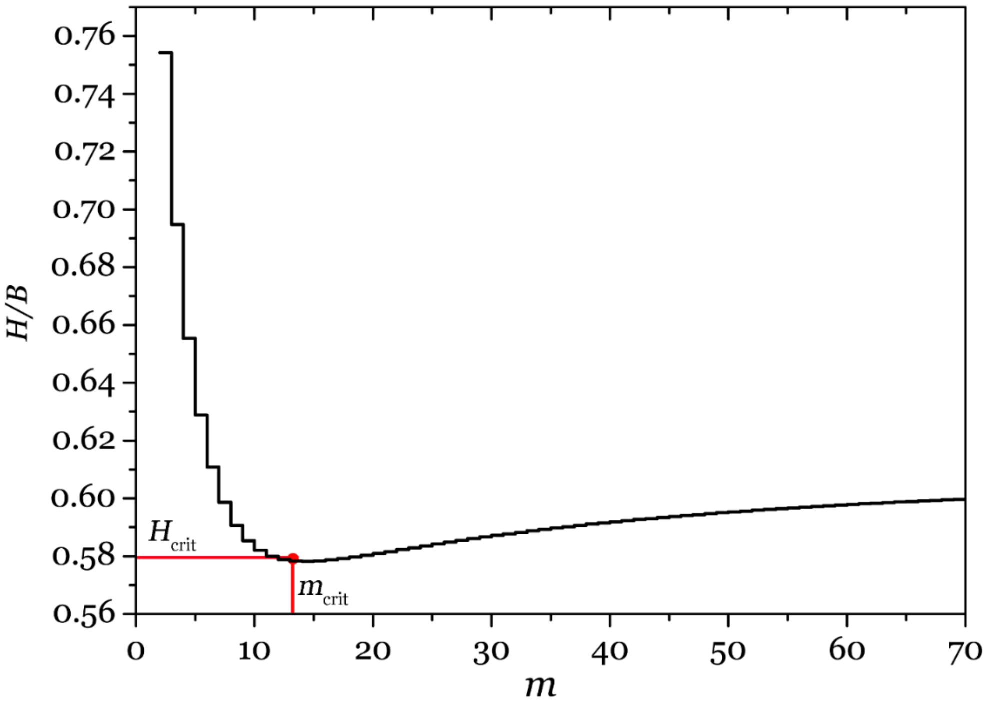

Figure 4.5: Critical tube thickness for the wrinkling instability with respect to the wavenumber *m*. The red dot represents the critical thickness and the critical wave number for the wrinkling instability in the an everted tube, which are H_{cirt}=0.58*B* and m_{cirt}=14, respectively.

4.5 Creasing instability

We next calculate the critical thickness for the onset of creases on the inner surface of an everted tube. Creases are localized folds with a singular region of self-contact, around which the strain field is concentrated and finite [95, 98, 175]. Consequently, the critical condition for the onset of creases and the subsequent growth of creases cannot be predicted by linear stability analyses. In this section, we conduct a nonlinear finite element simulation using the commercial software ABAQUS (version 6.12.1) to predict the critical condition for the onset of creases and crease patterns in an everted cylindrical tube.

As shown in the previous studies [95], the crease initiation is autonomous, so the critical condition of creasing instability can be determined by the local strain field. Based on numerical simulation and energetic analyses, Hong et al [95] obtained the critical condition for the initiation of a crease on a free surface,

$$\lambda_3/\lambda_1 = 2.4, \tag{4.29}$$

where direction 3 is normal to the surface, and direction 1 is in the surface and normal to the crease, and the principle stretches correspond to λ_θ and λ_r in the cylindrical coordinates adopted in the current tube eversion problem. Consequently, we can easily obtain the critical tube thickness for the onset of creases as $H_{crit=}0.435B$, through comparing the stretches in the inner surface of an everted tube with different thickness as shown in Fig.3b and the critical condition of Eq. (4.29) for the initiation of a crease on a free surface. The predicted critical tube thickness for creasing instability is much smaller than the critical thickness for wrinkling instability as predicted in Section 4. Therefore, our analyses suggest that creasing, instead of wrinkling, is the mechanical instability mode in an everted tube with large thickness.

We next conduct finite element simulations to further confirm the critical condition for the crease initiation obtained above. To avoid simulating the complex tube eversion process, we first map our previously computed stress field for the axisymmetric deformation of an everted tube into our 2D finite element model. The equilibrium stress state obtained in Section 3 is introduced as initial stress through the user subroutine SIGINI in ABAQUS, which is then called at the beginning of the creasing analysis. The subsequent deformation is set to be in generalized plane-strain condition with a constant axial stretch λ_z. The plane-strain hybrid element CPE6MH is adopted to simulate the crease formation. To simplify the problem, we assume creases distribute around the inner surface of an everted tube periodically. Therefore, only half of the crease with symmetric boundary condition is used in the simulation as shown in the inset of Fig. 4.6, with θ being the angle of a sector. By varying the angle of the sectors, we can simulate the scenario of an everted tube with different number of creases on its inner surface.

To artificially introduce a crease, we impose a radial displacement d at a point 0n the inner surface of an everted tube as shown in Fig.6. We then numerically calculate the strain energy of the everted tube as a function of crease depth d. In Fig.6, we plot the strain energy of the everted tube with $\theta=\pi/12$ in the creasing state U_c, normalized by the strain energy of the everted tube with asymmetric deformation U_o, as a function of crease depth d/H. When the tube thickness H is small, the strain energy of an everted tube increases monotonically with the increase of crease depth d (dash lines in Fig.6). When the tube thickness H is larger than $H_{crit=}0.435B$, the strain energy of the everted tube decreases first with the increase of crease depth, which reaches a minimum value for a certain crease depth defined as d_{crit}. Further increase of crease depth will cause the increase of the strain energy. The computational results verify that when the tube thickness is larger than $0.435B$, the formation of creases with certain depth on the inner surface of the everted tube can reduce its total strain energy.

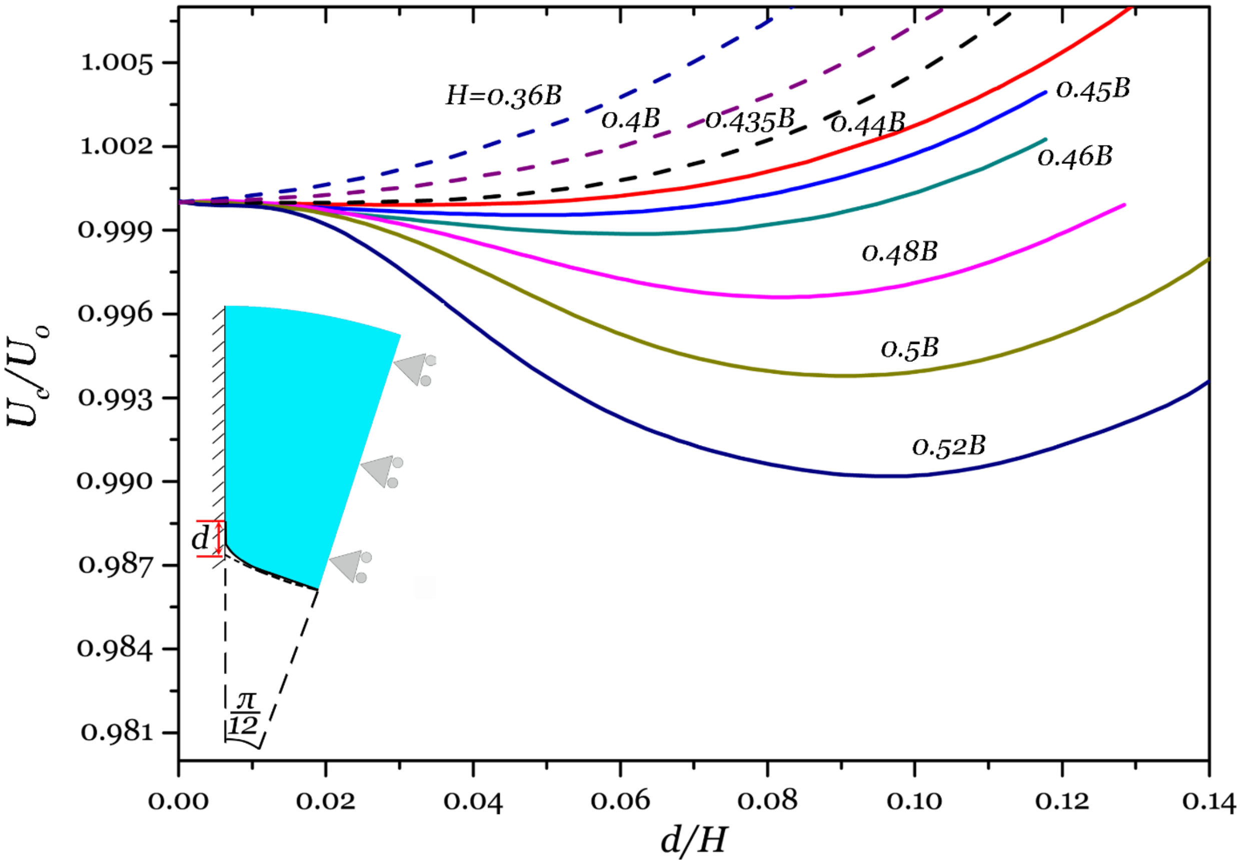

Figure 4.6: Normalized strain energy of an everted tube with different thicknesses as a function of crease depth d. When the thickness H is smaller than the critical thickness: $0.435B$, the strain energy of the everted tube increases monotonically with the increase of crease depth. When the thickness H is larger than the critical thickness, the strain energy of the everted tube has a minimum value for a finite crease depth. In the above calculation, we assume there are 12 creases distributed periodically around the inner surface of the everted tube.

The numerical simulation is consistent with our theoretical predictions of the critical tube thickness for the crease formation. The critical tube thickness for the onset of crease is much smaller than the critical thickness for wrinkle formation. The discovery successfully addresses the long-lasting discrepancy between theoretical predictions and experiments of mechanical instability in an everted tube as described in the introduction. Our prediction has also been confirmed by the experiments shown in Fig. 4.1. The inner surface of an everted tube is smooth in Fig.1a with the thickness: *H*=0.42*B*; while multiple creases are clearly visible on the inner surface of an everted tube in Fig.1b for the thickness: *H*=0.5*B*. Although it is not easy to determine the exact thickness for the onset of crease, the critical tube thickness has to fall in the range between 0.42*B* and 0.5*B*, which agree well with our prediction.

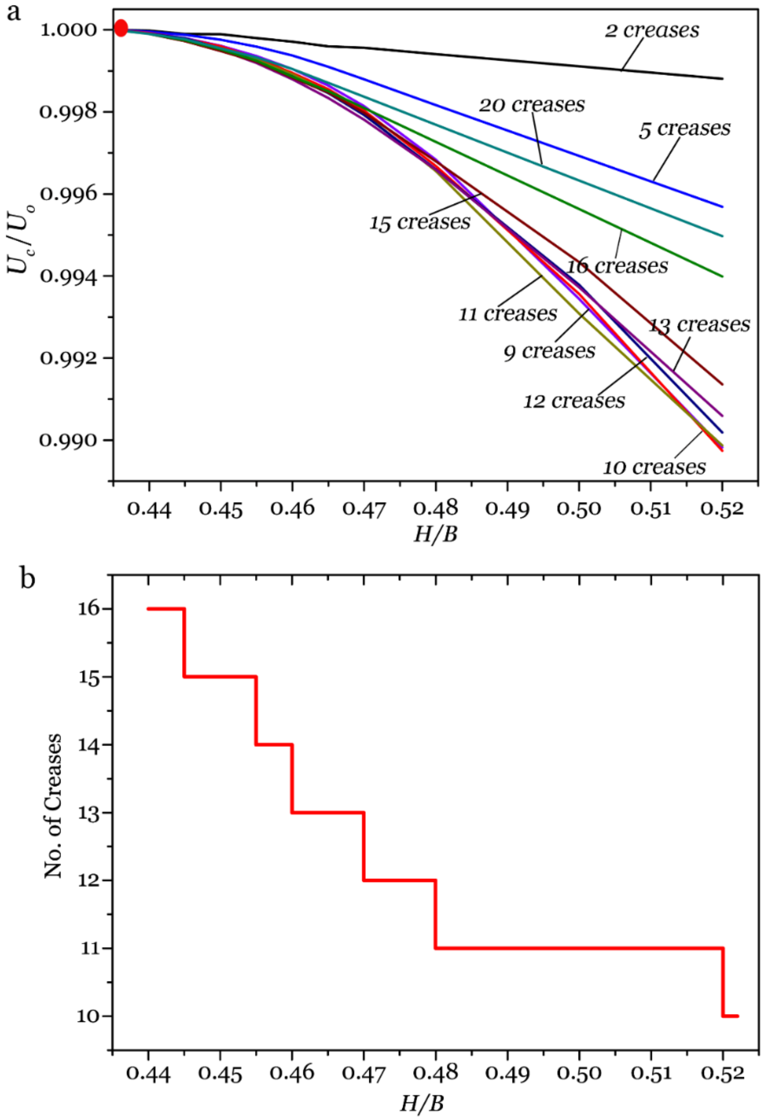

Figure 4.7: (a) Normalized strain energy of an everted tube with different number of creases. (b) Number of creases on its inner surface of everted tube with minimal strain energy.

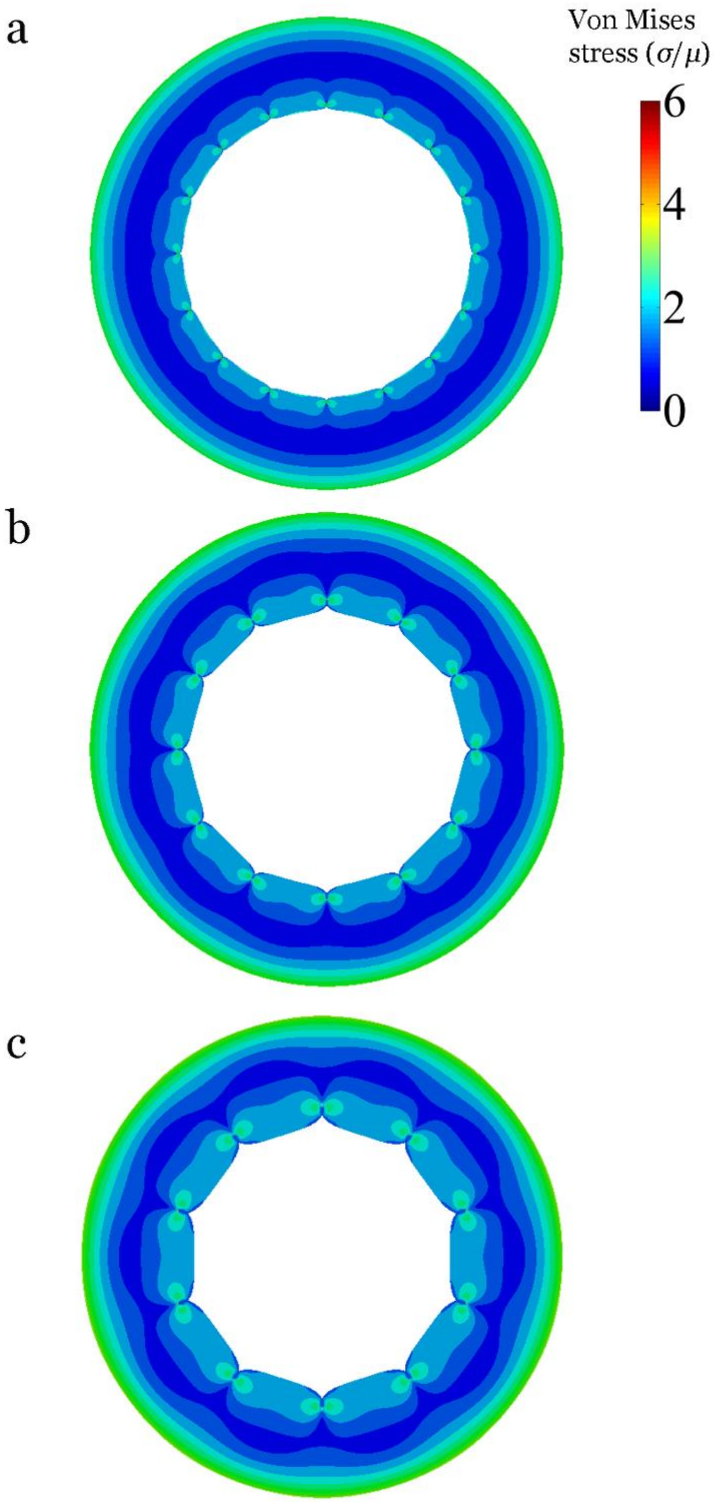

Figure 4.8: With the assumption of periodic crease distribution, the cross sections of everted tubes with minimalized strain energy for three different thicknesses: (a) H=0.44B, (b) H=0.48B, and (c) H=0.52B.

To predict the depth and number of creases forming on the inner surface of an everted tube with large thickness, we assume crease distribution is periodic and the creasing patterns observed in experiments minimize the total energy of the everted tube. Based on the assumptions, we next perform nonlinear finite element simulations to study crease patterns on the inner surface of an everted tube with thickness larger than H_{crit}. By varying the crease depth and the angle of the sector in the simulation, we can compute the minimal strain energy of an everted tube with different number of creases. To accurately capture the stress/strain field associated with the formation of creases in an everted tube and improve the convergence of the numerical simulation, mesh-to-mesh solution mapping in ABAQUS is adopted when elements are severely distorted during the crease formation. Old and severely deformed meshes are frequently replaced by new meshes with better quality. According to our knowledge, the numerical simulation strategy described above has never been reported to model crease formation in previous studies.

As shown in Fig. 4.7a, when the thickness of the tube H is larger than the critical thickness, an everted tube with finite number of creases on its inner surface can minimize its total strain energy. Based on the computational results shown in Fig.4.7a, we further plot the number of creases in Fig. 4.7b, which minimize the total strain energy of the everted tube, as a function of tube thickness. As expected, with increasing the tube thickness, the number of creases on the inner surface of everted tubes decreases.

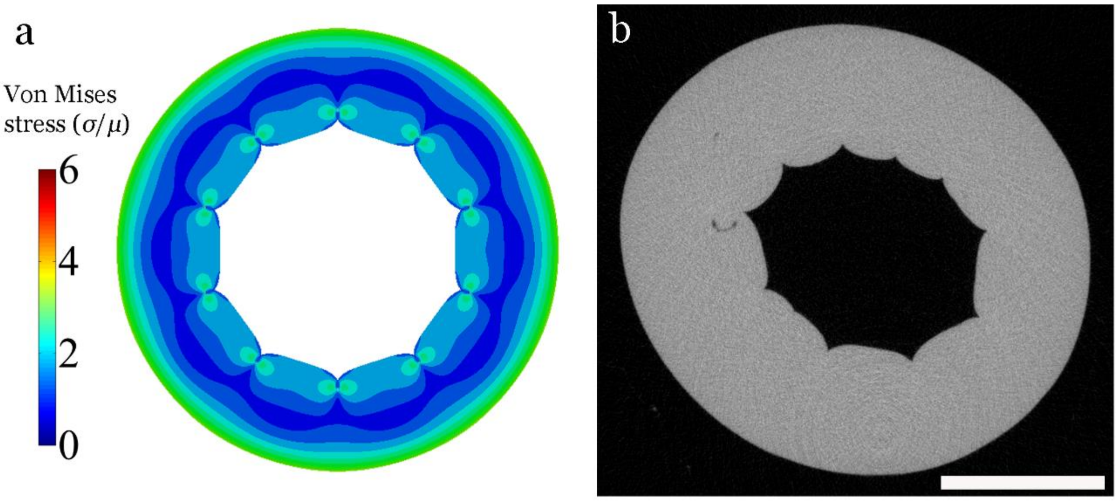

Figure 4.9: The comparison between the predicted and microCT image of a cross-section of an everted tube with the initial thickness of *H/B*=0.52. The color in (a) stands for the Von Mises stress normalized by the shear modulus μ of the elastomer. The length of the scale bar in (b) is 5mm.

Fig. 4.8a-c illustrates the stress distribution of everted tubes with different number of creases, which minimizes the total strain energy of the everted tubes. In Fig. 4.9, the predicted cross-section of an everted tube with thickness of *H/B*=0.52 is compared with its microCT image. It clearly shows that not only the number of creases, but also the profile of the inner surface of the everted tube can be well captured by our simulations.

Although our predictions agree well with experimental observations, certain limitations exist in our theory. For example, we assume the distributions of creases are periodic on the inner surface of everted tubes. The assumption may be invalid in certain scenarios. In particular, preexisting defects in the system may predetermine the locations of crease formation. In addition, we adopt Neo-Hookean model to characterize the hyperelasticity of elastomers in our experiments, which may be inaccurate for different elastomers. However, as discussed in the reference [95], the strain involved in the crease formation is finite but modest; Ne0-Hookean model should be accurate enough for many elastomers.

4.6 Conclusion

In this article, we studied mechanical instability of an everted cylindrical elastomer tube. By comparing the critical conditions of creasing and wrinkling, we show that the formation of creases, instead of wrinkles, is the mechanical instability mode for an everted tube when its thickness is larger than a critical value. Our studies have successfully resolved a long-lasting discrepancy between the theoretical predictions and experimental observations of eversion-induced mechanical instabilities in cylindrical elastomer tubes. Based on a hybrid theoretical-numerical approach, we have also successfully predicted the number of creases formed on the inner surface of a thick tube after eversion. The analyses we conduct in this article can be easily extended to investigate eversion-induced mechanical instability of other structures.

Chapter 4, in full appears in the paper "Creasing of an everted elastomer tube", *Soft matter* 12, no. 37 (2016): 7726-7730, by X. Liang; F. Tao and S. Cai. The dissertation author was the primary investigator and author of this paper.

Chapter 5 Gravity induced crease-to-wrinkle transition in soft materials

Creasing and wrinkling instability are two distinct surface instability modes characterized by localized singular folds and continuous smooth undulations, respectively. In this article, we show that the surface of a soft elastomer may develop wrinkles or creases under compression and the action of gravitational force, depending on the magnitude of gravitational force. Using linear perturbation analysis and numerical calculations, we establish a phase map with respective creasing domain, wrinkling domain and the domain of homogenous deformation. When the gravitational force is small, the surface of the elastomer forms creases when the compressive strain is beyond a critical value, while the surface of the elastomer forms wrinkles under compression when the gravitation force is large.

5.1 Introduction

Wrinkles and creases are two fundamentally distinct mechanical instability modes, which can be often observed in deformed soft materials such as gels and rubbers [67, 93, 177]. It has been demonstrated in both experiments and theoretical analyses that when a soft elastic solid is compressed beyond a critical strain, the free surface suddenly forms creases with self-contact [93, 95]. In a recent experiment [178], wrinkles have been observed on the surface of a soft gel under the effect of gravitational force. Those experiments suggest that the competition between elastic energy and gravitational potential energy in a soft solid may determine its surface instability mode-creases or wrinkles.

The effects of gravity on the elastic deformation of a solid can be evaluated by the magnitude of a dimensionless number: $\alpha=\rho gH/\mu$, where ρ is the density, g is the gravity, H is the characteristic size and μ is the elastic modulus of the solid. When the dimensionless number α is comparable or larger than 1, gravitational force may greatly affect the elastic deformation of solids. For example, when a mountain range is built in the crust, α is large due to the considerable characteristic size. Consequently, gravitational instability can happen in continental lithosphere [179]. Gravitational force also plays important roles in the deformation of soft bio-tissue such as intestinal tissue [47], which is commonly soft with a Young's modulus ranging from several hundred to several kilo Pa [180].

In this article, we investigate the conditions for the onset of creases and wrinkles on the surface of the soft elastic solid under compression and subject to the gravitational force. By comparing the onset conditions of creases and wrinkles, we establish a phase map with respective creasing domain, wrinkling domain and the domain of homogenous deformation.

5.2 Linear stability analysis

We first briefly summarize the governing equations of an elastic solid undergoing finite deformation. Deformation gradient of the solid is defined as,

$$F_{iK} = \frac{\partial x_i(\mathbf{X})}{\partial X_K}. \tag{5.1}$$

where X_i is the coordinates of a material point of the elastomer in undeformed state and x_i is the coordinate of the same material point in deformed configuration.

Using thermodynamics, the constitutive model of the solid can be specified by a certain free energy density function $W(\mathbf{F})$, namely

$$S_{iK} = \frac{\partial W(\mathbf{F})}{\partial F_{iK}}. \tag{5.2}$$

where S_{iK} is the nominal stress.

With taking account of the gravitational force, the mechanical equilibrium of the solid requires that,

$$\frac{\partial S_{iK}}{\partial X_K} + \rho g_i = 0. \tag{5.3}$$

where g_i is the component of gravity.

(a) Undeformed state

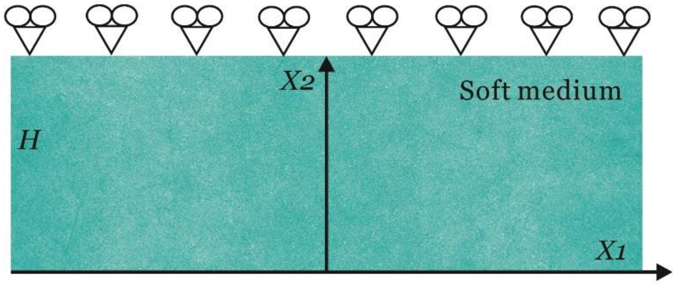

(b) Deformed state

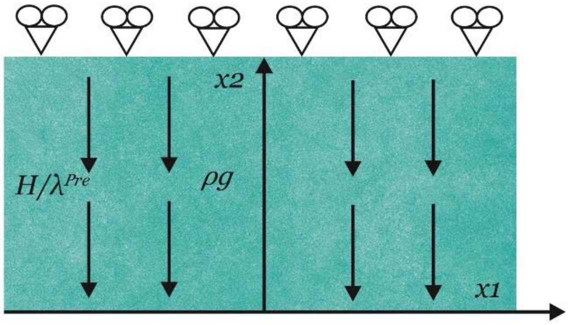

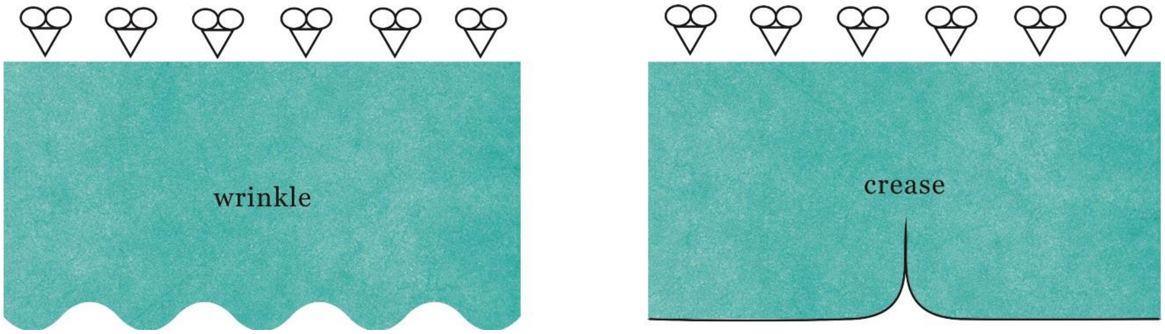
(c) Wrinkling state

(d) Creasing state

Figure 5.1: An elastomer is subject to gravity and uniaxial compression. (a) The undeformed elastomer is taken to be the reference state with thickness *H*. (b) The homogeneously deformed state of the elastomer is under gravity force ρg and pre-stretch λ^{Pre}. When the compressive strain is large enough, the homogenously deformed state may bifurcate into (c) wrinkling state or (d) creasing state.

Fig. 5.1a sketches the model to be analyzed in the article. A block of an undeformed elastomer with thickness *H* is taken to be the reference state. The gravity force α and uniaxial pre-stretch λ^{Pre} are applied to the block of elastomer as shown in Fig. 5.1b. The top surface of the elastomer is not allowed to move vertically and the elastomer is assumed to deform in plane strain condition. When the compression or gravitational force is large, homogenously deformed elastomer may bifurcate either into wrinkling state (Fig. 5.1c) or creasing state (Fig. 5.1d) depending on the magnitude of the dimensionless parameter α.

To obtain the critical conditions of wrinkling of the elastomeric block under compression, we adopt linear perturbation analysis [67]. A homogeneously deformed elastomer with applied horizontal stretch λ^{Pre} can be described by,

$$x_1^0 = \lambda^{\mathrm{Pre}} X_1, \tag{5.4a}$$

$$x_2^0 = X_2 / \lambda^{\mathrm{Pre}}. \tag{5.4b}$$

Next, we perturb the homogenous deformation by a state of infinitesimal displacement $\tilde{x}_i(\mathbf{X})$ to obtain an inhomogeneous deformation,

$$x_i(\mathbf{X}) = x_i^0(\mathbf{X}) + \tilde{x}_i(\mathbf{X}). \tag{5.5}$$

The corresponding additional deformation gradient $\tilde{F}_{iK}$ and nominal stress $\tilde{S}_{iK}$ caused by the perturbations are,

$$\tilde{F}_{iK} = \frac{\partial \tilde{x}_i(\mathbf{X})}{\partial X_K}, \tag{5.6}$$

$$\tilde{S}_{iK} = \frac{\partial^2 W(\mathbf{F})}{\partial F_{iK} \partial F_{jL}} \tilde{F}_{jL}\,. \tag{5.7}$$

The perturbed nominal stress needs to satisfy the force balance equations,

$$\frac{\partial(\tilde{S}_{iK})}{\partial X_K} = 0. \tag{5.8}$$

A combination of Eqs (5.6)-(5.8) gives the governing equations for the infinitesimal displacement $\tilde{x}_i(\mathbf{X})$. The boundary conditions for the perturbations are,

$$\tilde{x}_1(X_1, H) = 0, \tag{5.9a}$$

$$\tilde{x}_2(X_1, H) = 0, \tag{5.9b}$$

$$\tilde{S}_{12}(X_1, 0) = 0, \tag{5.9c}$$

$$\tilde{S}_{22}(X_1, 0) = 0. \tag{5.9d}$$

In this article, we assume the elasticity of the elastomer can be described by Neo-Hookean model, with the free energy density W b**F**) [174]:

$$W(\mathbf{F}) = \frac{\mu}{2} F_{iK} F_{iK} - \pi(\det(\mathbf{F}) - 1). \tag{5.10}$$

where μ is the small-deformation shear modulus and $\pi(\mathbf{X})$ is the Lagrange multiplier to enforce the constraint of incompressibility.

To solve the perturbation field, we assume,

$$\tilde{x}_1(X_1, X_2) = f_1(X_2)\sin(mX_1), \tag{5.11a}$$

$$\tilde{x}_2(X_1, X_2) = f_2(X_2)\cos(mX_1). \tag{5.11b}$$

Substituting Eq (5.11) into Eqs (5.6)-(5.8), we obtains that

$$f_2^{IV} - m^2\left(1+\frac{1}{(\lambda^{Pre})^4}\right) f_2'' + \frac{m^4}{(\lambda^{Pre})^4} f_2 = 0. \tag{5.12}$$

The differentiation of f_2 is over X_2 and m is the wavenumber in Eq (5.11) and it relates to the wavelength λ of the wrinkle by $\lambda=2\pi/m$. The ordinary differential Eq (5.12), accompanied with the boundary condition, leads to an eigenvalue problem, of which the trivial solution represents the homogeneous state, while the nontrivial solutions correspond to the wrinkling state. The eigenvalue that determines the onset condition of wrinkling can be obtained by solving

$$\det\begin{bmatrix} e^{mH} & -e^{-mH} & \frac{1}{(\lambda^{Pre})^2} e^{\frac{mH}{(\lambda^{Pre})^2}} & -\frac{1}{(\lambda^{Pre})^2} e^{\frac{-mH}{(\lambda^{Pre})^2}} \\ e^{mH} & e^{-mH} & e^{\frac{mH}{(\lambda^{Pre})^2}} & e^{\frac{-mH}{(\lambda^{Pre})^2}} \\ 1+(\lambda^{Pre})^4 & 1+(\lambda^{Pre})^4 & 2 & 2 \\ \frac{\alpha\lambda^{Pre}}{mH}+2 & \frac{\alpha\lambda^{Pre}}{mH}-2 & \frac{\alpha\lambda^{Pre}}{mH}+\frac{1+(\lambda^{Pre})^4}{(\lambda^{Pre})^2} & \frac{\alpha\lambda^{Pre}}{mH}-\frac{1+(\lambda^{Pre})^4}{(\lambda^{Pre})^2} \end{bmatrix} = 0. \tag{5.13}$$

The critical strain $\varepsilon_{\text{critical}}$, defined as the strain at which nontrivial solutions exist in Eq (5.12) for a given gravity α, is plotted in Fig. 5.2a. Biot's classical result of the wrinkling in an elastomer under compression are recovered for α=0. With the increase of gravity, less compressive strain is needed to induce wrinkles on the surface of the elastomer. Gravity may even induce wrinkles with certain wavelength on the surface of a pre-stretched elastomer (e.g when α>7). The reason that gravity can facilitate the formation of wrinkles is the gravitational potential of the solid can be reduced through surface wrinkling [178].

In Fig. 5.2a, we can also find that wrinkles with small wavelength are not affected by the presence of gravity. The results can be understood using the following scaling analysis: when the wavelength of wrinkles is much smaller than the thickness of the elastomer, the wavelength λ is the only relevant length scale. As a consequence, the dimensionless parameter reflecting the importance of gravity changes to $\rho g H/\mu$, which is small when the wavelength is small.

As shown in Fig. 5.2a, for a certain gravity, critical strain for wrinkles depends on their wavelength. There exists one wavelength of wrinkle requiring smallest compressive strain (or largest tensile strain), which is defined as the critical mode. Wavelength of critical mode is plotted as a function of gravity in Fig. 5.2b. The red-cross in Fig. 5.2b is the recent experimental measurement of the wrinkle wavelength on the surface of a soft gel only under the action of gravitational force [5].

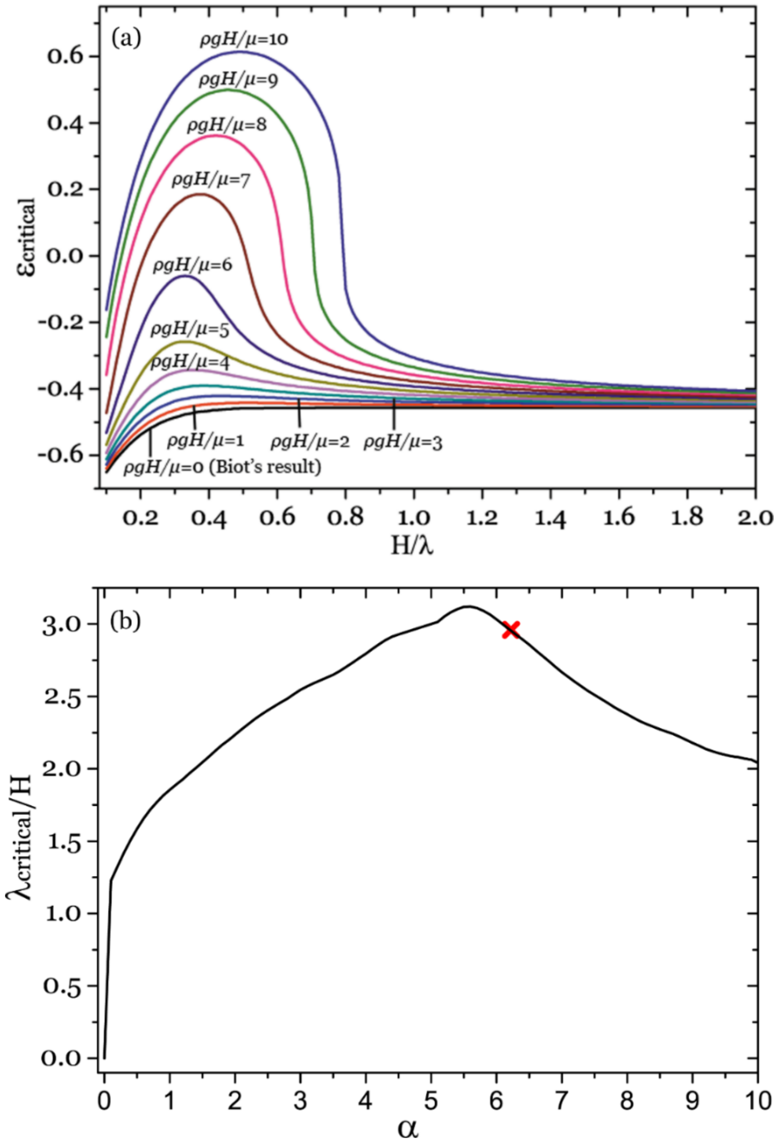

Figure 5.2: (a) Critical strains f0r wrinkles with different wavelength for different gravitational forces. (b) Wavelength of critical mode of wrinkles as a function of gravity. Red Cross point is from Mora *et. al* [178].

5.3 Crease analysis

As discussed at the beginning of this article, the surface of a compressed elastomer forms creases instead of wrinkles when the gravitational force is negligible. Our recent researches on creases have shown that the strain for the onset of creases cannot be predicted by linear perturbation analysis [181, 182]. Instead, a combination of numerical calculations and energetic analysis, adopted in the previous studies, precisely predicted the strain for the onset of the crease[95].

Before detailed analysis, using similar scaling analysis for the wrinkles with small wavelength, we expect that the gravitational force will have negligible effects on the onset of creases, because the crease size is the only relevant length scale, which is infinitesimal for incipient creases. The prediction is verified in the following numerical analyses.

To obtain the strain for the onset of creases, following Hong et.al. [95], we calculate the free energy difference ΔU between an elastomer with homogenously deformation and the one with a prescribed crease of small depth L, using FEM simulation (as shown in Fig. 5.3 insert). The free energy of the elastomer is equal to the summation of the elastic energy and the gravity potential of the elastomer. For an incipient crease, its depth is the only length scale, so

$$\Delta U = \mu L^2 f(\varepsilon,\alpha) . \tag{5.14}$$

where the dimensionless number $f(\varepsilon,\alpha)$ is to be calculated and is a function of applied strain ε and the dimensionless gravity α. If $\Delta U>0$, the homogeneously deformed elastomer has lower free energy. If $\Delta U<0$, the crease state has lower free energy. Consequently, the critical condition for the onset of crease is

$$f(\varepsilon,\alpha) = 0. \tag{5.15}$$

As shown in Fig.5.3, which clearly indicates that the effects of gravity on the strain of the onset of creases is negligible.

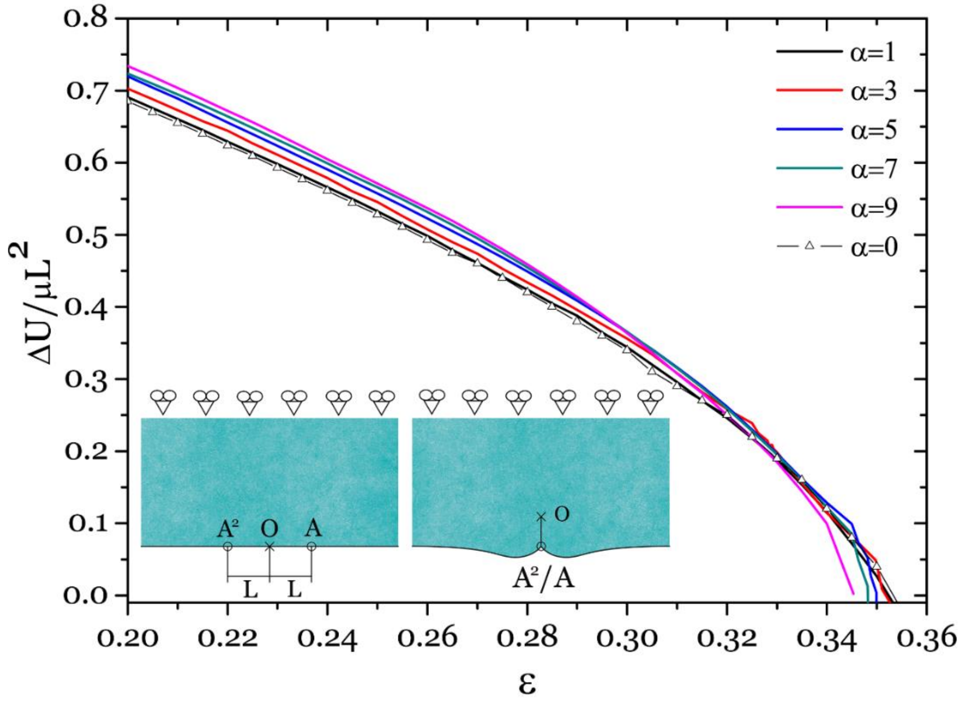

Figure 5.3: Free energy different between an elastomer with homogenous deformation and the one with crease with infinitesimal depth under different gravitational forces. The numerical results show that he effects of gravitational force on the formation of creases are negligible.

The critical conditions for the onset of creases and the critical mode of wrinkles are both plotted in Fig. 5.4. When the strain is larger than the critical strain for both creases and wrinkles, the elastomer will deform homogeneously with keeping its surface flat. The surface of elastomer will form creases or wrinkles, when the strain is smaller than the critical strain for the onset of creases or wrinkles (whichever is larger). Base on the calculation, we can divide Fig. 5.4 into three domains, which are homogenous deformation, creasing state and wrinkling state respectively. When gravity is small (α<3.8) and the compression strain exceeds 35%, creasing instability is formed. When gravity is large (α>3.8), wrinkling instability develops prior to the creasing instability with an increasing critical strain.

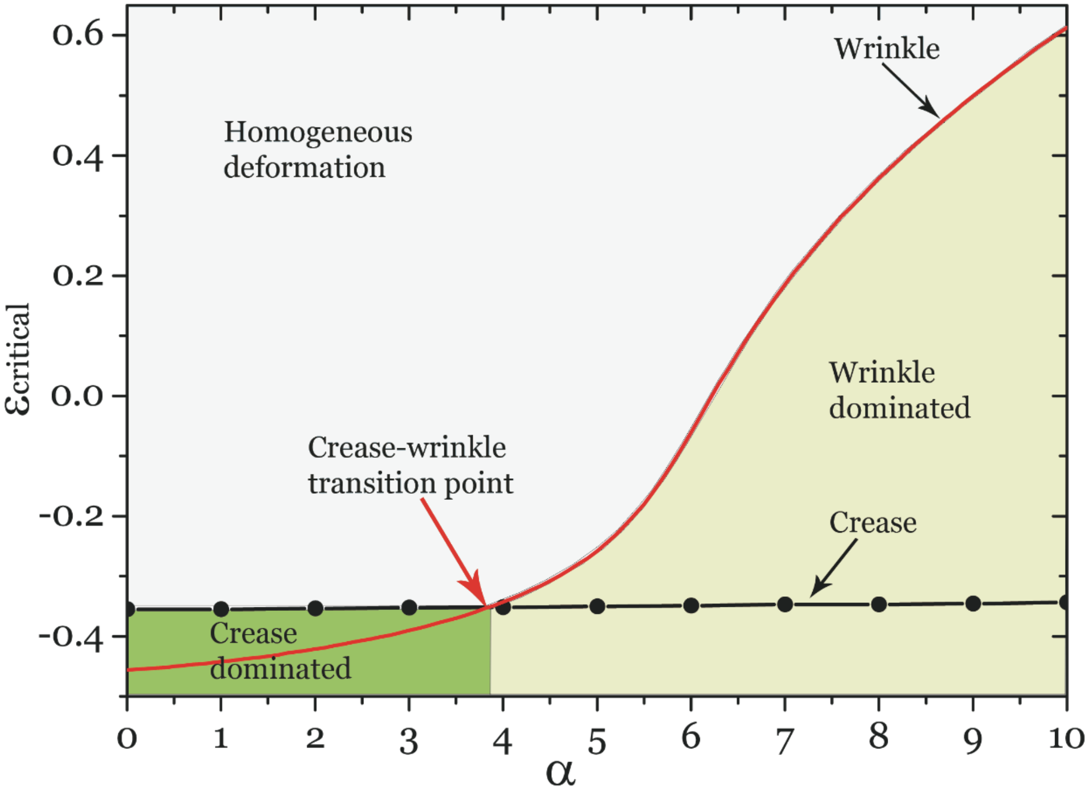

Figure 5.4: Comparison of the critical strain of the onset of wrinkles and crease under gravity. The two critical conditions intersect at α~3.8, indicating the possible transition between crease and wrinkle. When α<3.8, crease is the surface instability mode when an elastomer is under compression. For α>3.8, wrinkle is the surface instability mode.

5.4 Conclusion

In summary, surface instability of a soft elastic solid has been recently intensively studied, when the solid is subject to either compression or gravitational force. In the article, we investigate surface instability of a soft elastic solid under both pre-stretch and gravity using analytical analyses and numerical simulations. We found that the magnitude of gravity may determine the selection of surface instability mode when the soft solid is under compression. When the gravity is small, a compressed surface develops to crease instability. When the gravity is large, wrinkle is formed prior to the crease. The transition between crease instability and wrinkle instability is governed by magnitude of gravity. It has been shown that wrinkling of a uniform elastomer is extremely unstable and very difficult to observe [183]. In the article, we demonstrate that large gravitational force may stabilize the wrinkles on the surface of an elastomer under compression.

Chapter 5, in full appears in the paper "Gravity induced crease-to-wrinkle transition in soft materials", *Applied Physics Letters*106, no. 4 (2015): 041907, by X. Liang and S. Cai. The dissertation author was the primary investigator and author of this paper.

Chapter 6 Conclusion

Mechanical instabilities in soft materials are ubiquitous in nature and engineering applications. When subjected to a sufficiently large compression, the electric voltage, the gravity force or impact loadings, soft materials may undergo mechanical instabilities in various types. The instability modes can be either linear or nonlinear, depending on the form of perturbation when the instability set in. Due to the high stretchability of soft materials, new types of highly nonlinear instability are realized recently, which require us to have a deeper understanding of the mechanical instabilities in soft materials.

We started with the shape bifurcations in a spherical dielectric elastomer balloon under the actions of internal pressure and electric voltage. Using linear perturbation analysis, we demonstrate that a spherical dielectric elastomer balloon may bifurcate to a non-spherical shape under certain electromechanical loading conditions. By numerically solving the governing equations of the dielectric elastomer balloon with axisymmetric deformation and under different electromechanical loading conditions, we obtain both spherical deformation and non-spherical deformation solutions for the balloon. Our calculations further show that shape difference between two adjacent spherical and non-spherical deformation modes can be greatly enhanced by increasing the electrical voltage. The non-spherical deformation of the dielectric elastomer balloon in-turn induce large electric field concentration and stress/stretch concentration in certain area of the balloon, which may lead to the failure of the system. In addition, we conduct stability analysis of the dielectric elastomer balloon in different equilibrium configurations by evaluating its second variation of free energy under arbitrary perturbations. Our analyses indicate that under pressure-control and voltage-control mode, non-spherical deformation of the dielectric elastomer balloon is energetically unstable. However, under charge-control or ideal gas mass-control mode, non-spherical deformation of the balloon is energetically stable.

Since the DE balloon structures are normally obtained through mounting an elastomer membrane on an air chamber, which is coved by carbon grease over the top and bottom surface as soft electrodes. The membrane deforms into a balloon shape after air is pumped into the chamber while the boundary of the membrane remained fixed. Similar to the spherical DE balloon under the internal pressure and electric voltage, snap-through instability in such DE balloon was observed due to the non-monotonic relationship between the internal pressure and the volume of the balloon, which has been harnessed to achieve giant voltage-triggered deformation. In addition to the snap-through instability, with an applied voltage, a new electromechanical instability mode with a localized bulging-out in the balloon has been recently observed in experiments. However, the reported phenomenon has not been well explained. Through numerical computation, we obtain the relation between the volume of the balloon and its internal pressure, when the balloon is subjected to different voltages. We find out that when the applied voltage is small, the pressure vs. volume diagram of a balloon can be represented by an N-like curve, which is similar to the conventional hyperelastic balloon only subjected internal pressure; when the voltage is larger than a critical value, new instability modes in the balloon emerge, which have a localized bulging-out, similarly to the shape observed in the experiments. Based on our numerical calculations, we show that the bulging-out modes recently observed in a DE balloon can be an equilibrium configuration. Such a bulging-out shape does not rely on any specific material or geometrical defects. In addition, the prediction of the bulging-out configuration does not require any modifications of the DE balloon model. We further show that the DE balloon with a bulging-out shape can be realized in the experiment by gradually increasing the applied voltage while fixing the total amount of air enclosed in the balloon. We believe the bulging-out instability modes of a DE balloon are related to the non-convexity of the free energy density function of DE when the applied voltage is high. We finally show that prestretch as well as the material parameter (J_{lim}) can affect the voltage required for triggering the emergence of the bulging-out instability of a DE balloon.

Next we show the mechanical instability in a bulk of elastomer by everting an elastomeric tube. A cylindrical elastomer tube can stay in an everted state without any external forces, which is under an equilibrium state. If the thickness is small, an everted tube, except for the regions close to its free ends, maintains cylindrical shape; if the thickness is larger than a critical value, cross-section of the everted tube becomes noncircular, which is caused by mechanical instability. Although eversion-induced mechanical instability in an elastomer tube has been reported several decades before, a satisfying explanation of the phenomenon is still unavailable. In previous studies, linear or weakly nonlinear analyses have been usually adopted to predict the critical thickness of the tube for the eversion-induced instability. The discrepancy between the prediction and experiment is significant. In this article, based on experiments and theoretical analyses, we show that crease formation on the inner surface of an everted tube is the mechanical instability mode, which cannot be captured by linear stability analyses. Instead, a combination of energetic analyses and numerical simulations of finite deformation in an everted tube enables us to correctly predict both critical tube thickness for the onset of creases and profile of the noncircular cross-section of an everted tube with large thickness. The analyses we conduct in this article can be easily extended to investigate eversion-induced mechanical instability of other structures.

Creasing and wrinkling instability are two distinct surface instability modes characterized by localized singular folds and continuous smooth undulations, respectively. When a block of elastomer is compressed, crease instability is normally happen prior to the wrinkle instability, as the critical strain required the onset of crease is smaller than the one of wrinkle. We investigate surface instability of a soft elastic solid under both pre-stretch and gravity using analytical analyses and numerical simulations. We found that the magnitude of gravity may determine the selection of surface instability mode when the soft solid is under compression. When the gravity is small, a compressed surface develops to crease instability. When the gravity is large, wrinkle is formed prior to the crease. The transition between crease instability and wrinkle instability is governed by magnitude of gravity. We demonstrate that large gravitational force may stabilize the wrinkles on the surface of an elastomer under compression, and change the surface instability from crease to wrinkle.

Mechanical instability in soft materials is a fast growing research area due to the recent progress in materials science, biology and engineering. This dissertation hopes to provide some insights of both linear and nonlinear instabilities in different types of soft materials under various loading conditions and contribute to applications of soft materials in a board research areas.

Bibliography

[1] S. Kim, C. Laschi, B. Trimmer, Soft robotics: a bioinspired evolution in robotics, Trends in biotechnology 31(5) (2013) 287-294.

[2] E. Ruppert, R. Fox, R. Barnes, Echinodermata, Invertebrate Zoology 7th Edition. Brooks Cole Thompson, Belmont (2004) 872-929.

[3] I. Straehler-Pohl, C.L. Widmer, A.C. Morandini, Characterizations of juvenile stages of some semaeostome Scyphozoa (Cnidaria), with recognition of a new family (Phacellophoridae), Zootaxa 2741(1) (2011) 1-37.

[4] R. Pfeifer, F. Iida, J. Bongard, New robotics: Design principles for intelligent systems, Artificial life 11(1-2) (2005) 99-120.

[5] D. Rus, M.T. Tolley, Design, fabrication and control of soft robots, Nature 521(7553) (2015) 467.

[6] N.W. Bartlett, M.T. Tolley, J.T. Overvelde, J.C. Weaver, B. Mosadegh, K. Bertoldi, G.M. Whitesides, R.J. Wood, A 3D-printed, functionally graded soft robot powered by combustion, Science 349(6244) (2015) 161-165.

[7] X. Liu, H. Yuk, S. Lin, G.A. Parada, T.C. Tang, E. Tham, C. de la Fuente‐Nunez, T.K. Lu, X. Zhao, 3D Printing of Living Responsive Materials and Devices, Advanced Materials (2017).

[8] A.S. Gladman, E.A. Matsumoto, R.G. Nuzzo, L. Mahadevan, J.A. Lewis, Biomimetic 4D printing, Nature materials 15(4) (2016) 413.

[9] D. Trivedi, C.D. Rahn, W.M. Kier, I.D. Walker, Soft robotics: Biological inspiration, state of the art, and future research, Applied bionics and biomechanics 5(3) (2008) 99-117.

[10] S. Wolf, A. Albu-Schäffer, S. Haddadin, G. Hirzinger, From actively compliant lightweight robots to intrinsically compliant system, Citeseer, 2008.

[11] R.F. Shepherd, F. Ilievski, W. Choi, S.A. Morin, A.A. Stokes, A.D. Mazzeo, X. Chen, M. Wang, G.M. Whitesides, Multigait soft robot, Proceedings of the national academy of sciences 108(51) (2011) 20400-20403.

[12] M.T. Tolley, R.F. Shepherd, B. Mosadegh, K.C. Galloway, M. Wehner, M. Karpelson, R.J. Wood, G.M. Whitesides, A resilient, untethered soft robot, Soft robotics 1(3) (2014) 213-223.

[13] S.M. Felton, M.T. Tolley, C.D. Onal, D. Rus, R.J. Wood, Robot self-assembly by folding: A printed inchworm robot, Robotics and Automation (ICRA), 2013 IEEE International Conference on, IEEE, 2013, pp. 277-282.

[14] T. Sekitani, U. Zschieschang, H. Klauk, T. Someya, Flexible organic transistors and circuits with extreme bending stability, Nature materials 9(12) (2010) 1015.

[15] J.W. Lee, R. Xu, S. Lee, K.-I. Jang, Y. Yang, A. Banks, K.J. Yu, J. Kim, S. Xu, S. Ma, Soft, thin skin-mounted power management systems and their use in wireless thermography, Proceedings of the National Academy of Sciences 113(22) (2016) 6131-6136.

[16] S. Xu, Y. Zhang, L. Jia, K.E. Mathewson, K.-I. Jang, J. Kim, H. Fu, X. Huang, P. Chava, R. Wang, Soft microfluidic assemblies of sensors, circuits, and radios for the skin, Science 344(6179) (2014) 70-74.

[17] S. Xu, Z. Yan, K.-I. Jang, W. Huang, H. Fu, J. Kim, Z. Wei, M. Flavin, J. McCracken, R. Wang, Assembly of micro/nanomaterials into complex, three-dimensional architectures by compressive buckling, Science 347(6218) (2015) 154-159.

[18] Q.T. Nguyen, Y. Hwang, A.C. Chen, S. Varghese, R.L. Sah, Cartilage-like mechanical properties of poly (ethylene glycol)-diacrylate hydrogels, Biomaterials 33(28) (2012) 6682-6690.

[19] D.B. Kolesky, K.A. Homan, M.A. Skylar-Scott, J.A. Lewis, Three-dimensional bioprinting of thick vascularized tissues, Proceedings of the National Academy of Sciences 113(12) (2016) 3179-3184.

[20] G. Villar, A.D. Graham, H. Bayley, A tissue-like printed material, Science 340(6128) (2013) 48-52.

[21] S. Bauer, S. Bauer‐Gogonea, I. Graz, M. Kaltenbrunner, C. Keplinger, R. Schwödiauer, 25th anniversary article: a soft future: from robots and sensor skin to energy harvesters, Advanced Materials 26(1) (2014) 149-162.

[22] Q. Wang, X. Zhao, Beyond wrinkles: Multimodal surface instabilities for multifunctional patterning, MRS Bulletin 41(2) (2016) 115-122.

[23] Z. Suo, Theory of dielectric elastomers, Acta Mechanica Solida Sinica 23(6) (2010) 549-578.

[24] N. Goulbourne, E. Mockensturm, M. Frecker, A nonlinear model for dielectric elastomer membranes, Journal of Applied Mechanics 72(6) (2005) 899-906.

[25] A. Dorfmann, R. Ogden, Nonlinear electroelasticity, Acta Mechanica 174(3-4) (2005) 167-183.

[26] R.M. McMeeking, C.M. Landis, Electrostatic forces and stored energy for deformable dielectric materials, Journal of Applied Mechanics 72(4) (2005) 581-590.

[27] Z. Suo, X. Zhao, W.H. Greene, A nonlinear field theory of deformable dielectrics, Journal of the Mechanics and Physics of Solids 56(2) (2008) 467-486.

[28] C. Trimarco, On the Lagrangian electrostatics of elastic solids, Acta Mechanica 204(3-4) (2009) 193.

[29] K. Sekimoto, Thermodynamics and hydrodynamics of chemical gels, Journal de Physique II 1(1) (1991) 19-36.

[30] J. Dolbow, E. Fried, H. Ji, Chemically induced swelling of hydrogels, Journal of the Mechanics and Physics of Solids 52(1) (2004) 51-84.

[31] S. Baek, A. Srinivasa, Diffusion of a fluid through an elastic solid undergoing large deformation, International Journal of non-linear Mechanics 39(2) (2004) 201-218.

[32] W. Hong, X. Zhao, J. Zhou, Z. Suo, A theory of coupled diffusion and large deformation in polymeric gels, Journal of the Mechanics and Physics of Solids 56(5) (2008) 1779-1793.

[33] M. Doi, Gel dynamics, Journal of the Physical Society of Japan 78(5) (2009) 052001-052001.

[34] S.A. Chester, L. Anand, A coupled theory of fluid permeation and large deformations for elastomeric materials, Journal of the Mechanics and Physics of Solids 58(11) (2010) 1879-1906.

[35] S. Nemat-Nasser, J.Y. Li, Electromechanical response of ionic polymer-metal composites, Journal of Applied Physics 87(7) (2000) 3321-3331.

[36] W. Hong, X. Zhao, Z. Suo, Large deformation and electrochemistry of polyelectrolyte gels, Journal of the Mechanics and Physics of Solids 58(4) (2010) 558-577.

[37] S. Baek, A. Srinivasa, Modeling of the pH-sensitive behavior of an ionic gel in the presence of diffusion, International Journal of Non-linear Mechanics 39(8) (2004) 1301-1318.

[38] H. Li, R. Luo, E. Birgersson, K. Lam, Modeling of multiphase smart hydrogels responding to p H and electric voltage coupled stimuli, Journal of Applied Physics 101(11) (2007) 114905.

[39] R. Marcombe, S. Cai, W. Hong, X. Zhao, Y. Lapusta, Z. Suo, A theory of constrained swelling of a pH-sensitive hydrogel, Soft Matter 6(4) (2010) 784-793.

[40] S. Cai, Z. Suo, Mechanics and chemical thermodynamics of phase transition in temperature-sensitive hydrogels, Journal of the Mechanics and Physics of Solids 59(11) (2011) 2259-2278.

[41] B. Li, Y.-P. Cao, X.-Q. Feng, H. Gao, Mechanics of morphological instabilities and surface wrinkling in soft materials: a review, Soft Matter 8(21) (2012) 5728-5745.

[42] J. Genzer, J. Groenewold, Soft matter with hard skin: From skin wrinkles to templating and material characterization, Soft Matter 2(4) (2006) 310-323.

[43] D.H.N. Spence, The zonation of plants in freshwater lakes, Advances in ecological research, Elsevier1982, pp. 37-125.

[44] P.S. Stevens, Patterns in Nature (Boston: Little Brown, 1974), Gy6rgy Doczi, The Power of Limits: Proportional Harmonies in Nature, Art and Architecture (Boston: Shambhala, 1981).

[45] L. Wang, C.E. Castro, M.C. Boyce, Growth strain-induced wrinkled membrane morphology of white blood cells, Soft Matter 7(24) (2011) 11319-11324.

[46] K.D. Walton, Å. Kolterud, M.J. Czerwinski, M.J. Bell, A. Prakash, J. Kushwaha, A.S. Grosse, S. Schnell, D.L. Gumucio, Hedgehog-responsive mesenchymal clusters direct patterning and emergence of intestinal villi, Proceedings of the National Academy of Sciences 109(39) (2012) 15817-15822.

[47] M.B. Amar, F. Jia, Anisotropic growth shapes intestinal tissues during embryogenesis, Proceedings of the National Academy of Sciences 110(26) (2013) 10525-10530.

[48] E. Hannezo, J. Prost, J.-F. Joanny, Instabilities of monolayered epithelia: shape and structure of villi and crypts, Physical Review Letters 107(7) (2011) 078104.

[49] E. Hohlfeld, L. Mahadevan, Unfolding the sulcus, Physical review letters 106(10) (2011) 105702.

[50] T. Tallinen, J.S. Biggins, L. Mahadevan, Surface sulci in squeezed soft solids, Physical review letters 110(2) (2013) 024302.

[51] J. Yin, G.J. Gerling, X. Chen, Mechanical modeling of a wrinkled fingertip immersed in water, Acta biomaterialia 6(4) (2010) 1487-1496.

[52] M. Kücken, A. Newell, A model for fingerprint formation, EPL (Europhysics Letters) 68(1) (2004) 141.

[53] Q. Wang, X. Zhao, A three-dimensional phase diagram of growth-induced surface instabilities, Scientific reports 5 (2015) 8887.

[54] X. Chen, J. Yin, Buckling patterns of thin films on curved compliant substrates with applications to morphogenesis and three-dimensional micro-fabrication, Soft Matter 6(22) (2010) 5667-5680.

[55] J. Song, H. Jiang, Y. Huang, J. Rogers, Mechanics of stretchable inorganic electronic materials, Journal of Vacuum Science & Technology A: Vacuum, Surfaces, and Films 27(5) (2009) 1107-1125.

[56] J.Y. Chung, A.J. Nolte, C.M. Stafford, Surface wrinkling: a versatile platform for measuring thin - film properties, Advanced Materials 23(3) (2011) 349-368.

[57] S. Yang, K. Khare, P.C. Lin, Harnessing surface wrinkle patterns in soft matter, Advanced Functional Materials 20(16) (2010) 2550-2564.

[58] N. Bowden, S. Brittain, A.G. Evans, J.W. Hutchinson, G.M. Whitesides, Spontaneous formation of ordered structures in thin films of metals supported on an elastomeric polymer, Nature 393(6681) (1998) 146.

[59] T. Kato, Perturbation theory for linear operators, Springer Science & Business Media2013.

[60] G.W. Stewart, Matrix perturbation theory, (1990).

[61] R.W. Ogden, Non-linear elastic deformations, Courier Corporation1997.

[62] Y. Cao, J.W. Hutchinson, Wrinkling phenomena in neo-Hookean film/substrate bilayers, Journal of applied mechanics 79(3) (2012) 031019.

[63] B. Audoly, A. Boudaoud, Buckling of a stiff film bound to a compliant substrate—Part I:: Formulation, linear stability of cylindrical patterns, secondary bifurcations, Journal of the Mechanics and Physics of Solids 56(7) (2008) 2401-2421.

[64] J. Nowinski, Surface instability of a half-space under high two-dimensional compression, Journal of The Franklin Institute 288(5) (1969) 367-376.

[65] Q. Wang, X. Zhao, Phase diagrams of instabilities in compressed film-substrate systems, Journal of applied mechanics 81(5) (2014) 051004.

[66] A.M. Van der Heijden, WT Koiter's elastic stability of solids and structures, Cambridge University Press Cambridge2008.

[67] M.A. Biot, Surface instability of rubber in compression, Applied Scientific Research, Section A 12(2) (1963) 168-182.

[68] M.A. Biot, Interfacial instability in finite elasticity under initial stress, Proc. R. Soc. Lond. A, The Royal Society, 1963, pp. 340-344.

[69] E. Cerda, L. Mahadevan, Geometry and physics of wrinkling, Physical review letters 90(7) (2003) 074302.

[70] Z. Huang, W. Hong, Z. Suo, Nonlinear analyses of wrinkles in a film bonded to a compliant substrate, Journal of the Mechanics and Physics of Solids 53(9) (2005) 2101-2118.

[71] X. Chen, J.W. Hutchinson, Herringbone buckling patterns of compressed thin films on compliant substrates, Journal of applied mechanics 71(5) (2004) 597-603.

[72] K.D. Danov, P.A. Kralchevsky, S.D. Stoyanov, Elastic Langmuir layers and membranes subjected to unidirectional compression: wrinkling and collapse, Langmuir 26(1) (2009) 143-155.

[73] S. Cai, D. Breid, A.J. Crosby, Z. Suo, J.W. Hutchinson, Periodic patterns and energy states of buckled films on compliant substrates, Journal of the Mechanics and Physics of Solids 59(5) (2011) 1094-1114.

[74] J. Groenewold, Wrinkling of plates coupled with soft elastic media, Physica A: Statistical Mechanics and its Applications 298(1-2) (2001) 32-45.

[75] H. Jiang, D.-Y. Khang, J. Song, Y. Sun, Y. Huang, J.A. Rogers, Finite deformation mechanics in buckled thin films on compliant supports, Proceedings of the National Academy of Sciences 104(40) (2007) 15607-15612.

[76] J. Song, H. Jiang, Z. Liu, D. Khang, Y. Huang, J. Rogers, C. Lu, C. Koh, Buckling of a stiff thin film on a compliant substrate in large deformation, International Journal of Solids and Structures 45(10) (2008) 3107-3121.

[77] B. Li, S.-Q. Huang, X.-Q. Feng, Buckling and postbuckling of a compressed thin film bonded on a soft elastic layer: a three-dimensional analysis, Archive of Applied Mechanics 80(2) (2010) 175.

[78] J.-Y. Sun, S. Xia, M.-W. Moon, K.H. Oh, K.-S. Kim, Folding wrinkles of a thin stiff layer on a soft substrate, Proc. R. Soc. A, The Royal Society, 2012, pp. 932-953.

[79] T. Li, C. Keplinger, R. Baumgartner, S. Bauer, W. Yang, Z. Suo, Giant voltage-induced deformation in dielectric elastomers near the verge of snap-through instability, Journal of the Mechanics and Physics of Solids 61(2) (2013) 611-628.

[80] H. Alexander, Tensile instability of initially spherical balloons, International Journal of Engineering Science 9(1) (1971) 151-160.

[81] A. Needleman, Inflation of spherical rubber balloons, International Journal of Solids and Structures 13(5) (1977) 409-421.

[82] D. Haughton, R. Ogden, On the incremental equations in non-linear elasticity—II. Bifurcation of pressurized spherical shells, Journal of the Mechanics and Physics of Solids 26(2) (1978) 111-138.

[83] Y.-C. Chen, T.J. Healey, Bifurcation to pear-shaped equilibria of pressurized spherical membranes, International Journal of Non-Linear Mechanics 26(3-4) (1991) 279-291.

[84] Y. Fu, Y. Xie, Stability of pear-shaped configurations bifurcated from a pressurized spherical balloon, Journal of the Mechanics and Physics of Solids 68 (2014) 33-44.

[85] R.W. Ogden, Large deformation isotropic elasticity–on the correlation of theory and experiment for incompressible rubberlike solids, Proc. R. Soc. Lond. A, The Royal Society, 1972, pp. 565-584.

[86] V. Feodos' ev, On equilibrium modes of a rubber spherical shell under internal pressure: PMM vol. 32, no. 2, 1968, pp. 339–344, Journal of Applied Mathematics and Mechanics 32(2) (1968) 335-341.

[87] R.T. Shield, On the stability of finitely deformed elastic membranes, Zeitschrift für angewandte Mathematik und Physik ZAMP 23(1) (1972) 16-34.

[88] Y. Fu, Y. Xie, Stability of localized bulging in inflated membrane tubes under volume control, International Journal of Engineering Science 48(11) (2010) 1242-1252.

[89] S. Kyriakides, C. Yu-Chung, On the inflation of a long elastic tube in the presence of axial load, International journal of solids and structures 26(9-10) (1990) 975-991.

[90] A. Gent, Elastic instabilities in rubber, International Journal of Non-Linear Mechanics 40(2-3) (2005) 165-175.

[91] A. Goriely, M. Destrade, M. Ben Amar, Instabilities in elastomers and in soft tissues, The Quarterly Journal of Mechanics & Applied Mathematics 59(4) (2006) 615-630.

[92] C. Keplinger, T. Li, R. Baumgartner, Z. Suo, S. Bauer, Harnessing snap-through instability in soft dielectrics to achieve giant voltage-triggered deformation, Soft Matter 8(2) (2012) 285-288.

[93] A. Gent, I. Cho, Surface instabilities in compressed or bent rubber blocks, Rubber Chemistry and Technology 72(2) (1999) 253-262.

[94] A. Ghatak, A.L. Das, Kink instability of a highly deformable elastic cylinder, Physical review letters 99(7) (2007) 076101.

[95] W. Hong, X. Zhao, Z. Suo, Formation of creases on the surfaces of elastomers and gels, Applied Physics Letters 95(11) (2009) 111901.

[96] F. Weiss, S. Cai, Y. Hu, M. Kyoo Kang, R. Huang, Z. Suo, Creases and Wrinkles on the Surface of a Swollen Gel, Journal of Applied Physics 114(7) (2013) 073507.

[97] X. Liang, S. Cai, Gravity induced crease-to-wrinkle transition in soft materials, Applied Physics Letters 106(4) (2015) 041907.

[98] S. Cai, D. Chen, Z. Suo, R.C. Hayward, Creasing instability of elastomer films, Soft Matter 8(5) (2012) 1301-1304.

[99] X. Liang, S. Cai, New electromechanical instability modes in dielectric elastomer balloons, International Journal of Solids and Structures (2017).

[100] Q. Wang, L. Zhang, X. Zhao, Creasing to cratering instability in polymers under ultrahigh electric fields, Physical review letters 106(11) (2011) 118301.

[101] Q. Wang, M. Tahir, L. Zhang, X. Zhao, Electro-creasing instability in deformed polymers: experiment and theory, Soft Matter 7(14) (2011) 6583-6589.

[102] R.A. Toupin, The elastic dielectric, Journal of Rational Mechanics and Analysis 5(6) (1956) 849-915.

[103] L.D. Landau, Lifshits EM Electrodynamics of Continuous Media, Course Theor. Phys 8 (1960) 15.

[104] A.C. Eringen, On the foundations of electroelastostatics, International Journal of Engineering Science 1(1) (1963) 127-153.

[105] H. Tiersten, On the nonlinear equations of thermo-electroelasticity, International Journal of Engineering Science 9(7) (1971) 587-604.

[106] L. Dorfmann, R.W. Ogden, Instabilities of an electroelastic plate, International Journal of Engineering Science 77 (2014) 79-101.

[107] T.J. Wagner, D. Vella, Floating carpets and the delamination of elastic sheets, Physical review letters 107(4) (2011) 044301.

[108] R. Vermorel, N. Vandenberghe, E. Villermaux, Impacts on thin elastic sheets, Proceedings of the Royal Society of London A: Mathematical, Physical and Engineering Sciences, The Royal Society, 2009, pp. 823-842.

[109] D.G. Vaughn, J.W. Hutchinson, Bucklewaves, European Journal of Mechanics-A/Solids 25(1) (2006) 1-12.

[110] E. Ferri, E. Antinucci, M. He, J. Hutchinson, F. Zok, A. Evans, Dynamic buckling of impulsively loaded prismatic cores, Journal of Mechanics of Materials and Structures 1(8) (2006) 1345-1365.

[111] N. Sridhar, D. Srolovitz, Z. Suo, Kinetics of buckling of a compressed film on a viscous substrate, Applied Physics Letters 78(17) (2001) 2482-2484.

[112] N. Sridhar, D. Srolovitz, B. Cox, Buckling and post-buckling kinetics of compressed thin films on viscous substrates, Acta Materialia 50(10) (2002) 2547-2557.

[113] S. Im, R. Huang, Evolution of wrinkles in elastic-viscoelastic bilayer thin films, Journal of applied mechanics 72(6) (2005) 955-961.

[114] R. Huang, Kinetic wrinkling of an elastic film on a viscoelastic substrate, Journal of the Mechanics and Physics of Solids 53(1) (2005) 63-89.

[115] R. Huang, Z. Suo, Wrinkling of a compressed elastic film on a viscous layer, Journal of Applied Physics 91(3) (2002) 1135-1142.

[116] H. Wang, M. Lei, S. Cai, Viscoelastic deformation of a dielectric elastomer membrane subject to electromechanical loads, Journal of Applied Physics 113(21) (2013) 213508.

[117] J. Zhu, S. Cai, Z. Suo, Nonlinear oscillation of a dielectric elastomer balloon, Polymer International 59(3) (2010) 378-383.

[118] M. Moscardo, X. Zhao, Z. Suo, Y. Lapusta, On designing dielectric elastomer actuators, Journal of Applied Physics 104(9) (2008) 093503.

[119] H. Wang, S. Cai, F. Carpi, Z. Suo, Computational model of hydrostatically coupled dielectric elastomer actuators, Journal of Applied Mechanics 79(3) (2012) 031008.

[120] X. Zhao, W. Hong, Z. Suo, Electromechanical hysteresis and coexistent states in dielectric elastomers, Physical review B 76(13) (2007) 134113.

[121] J. Huang, T. Li, C.C. Foo, J. Zhu, D.R. Clarke, Z. Suo, Giant, voltage-actuated deformation of a dielectric elastomer under dead load, Applied Physics Letters 100(4) (2012) 041911.

[122] R. Kornbluh, Technology Application-Dielectric Elastomer Artificial Muscle for Actuation, Sensing, Generation, and Intelligent Structures, Materials Technology 19(4) (2004) 216-223.

[123] J.W. Kwak, H.J. Chi, K.M. Jung, J.C. Koo, J.W. Jeon, Y. Lee, Y. Ryew, H.R. Choi, A face robot actuated with artificial muscle based on dielectric elastomer, Journal of mechanical science and technology 19(2) (2005) 578-588.

[124] R. Pelrine, R.D. Kornbluh, Q. Pei, S. Stanford, S. Oh, J. Eckerle, R.J. Full, M.A. Rosenthal, K. Meijer, Dielectric elastomer artificial muscle actuators: toward biomimetic motion, SPIE's 9th Annual International Symposium on Smart Structures and Materials, International Society for Optics and Photonics, 2002, pp. 126-137.

[125] G. Palli, G. Berselli, On the control of a dielectric elastomer artificial muscle with variable impedance, ASME 2013 Conference on Smart Materials, Adaptive Structures and Intelligent Systems, American Society of Mechanical Engineers, 2013, pp. V001T03A042-V001T03A042.

[126] F. Carpi, G. Frediani, D. De Rossi, Opportunities of hydrostatically coupled dielectric elastomer actuators for haptic interfaces, SPIE Smart Structures and Materials+ Nondestructive Evaluation and Health Monitoring, International Society for Optics and Photonics, 2011, pp. 797618-797618-9.

[127] D.L. Henann, S.A. Chester, K. Bertoldi, Modeling of dielectric elastomers: Design of actuators and energy harvesting devices, Journal of the Mechanics and Physics of Solids 61(10) (2013) 2047-2066.

[128] K. Pope, A. Tews, M.I. Frecker, E. Mockensturm, N.C. Goulbourne, A.J. Snyder, Dielectric elastomer laminates for active membrane pump applications, Smart Structures and Materials, International Society for Optics and Photonics, 2004, pp. 60-67.

[129] N. Goulbourne, M.I. Frecker, E.M. Mockensturm, A.J. Snyder, Modeling of a dielectric elastomer diaphragm for a prosthetic blood pump, Smart structures and Materials, International Society for Optics and Photonics, 2003, pp. 319-331.

[130] N.C. Goulbourne, M.I. Frecker, E. Mockensturm, Electro-elastic modeling of a dielectric elastomer diaphragm for a prosthetic blood pump, Smart Structures and Materials, International Society for Optics and Photonics, 2004, pp. 122-133.

[131] A.E. Bowers, J.M. Rossiter, P.J. Walters, I.A. Ieropoulos, Dielectric elastomer pump for artificial organisms, SPIE Smart Structures and Materials+ Nondestructive Evaluation and Health Monitoring, International Society for Optics and Photonics, 2011, pp. 797629-797629-7.

[132] S.-i. Son, D. Pugal, T. Hwang, H.R. Choi, J.C. Koo, Y. Lee, K. Kim, J.-D. Nam, Electromechanically driven variable-focus lens based on transparent dielectric elastomer, Applied optics 51(15) (2012) 2987-2996.

[133] D. Liang, Z.-F. Lin, C.-C. Huang, W.-P. Shih, Tunable lens driven by dielectric elastomer actuator with ionic electrodes, Micro & Nano Letters 9(12) (2014) 869-873.

[134] G.-K. Lau, T.-G. La, L.-L. Shiau, A.W.Y. Tan, Challenges of using dielectric elastomer actuators to tune liquid lens, Proc. of SPIE Vol, pp. 90561J-1.

[135] T. Hwang, H.-Y. Kwon, J.-S. Oh, J.-P. Hong, S.-C. Hong, Y. Lee, H.R. Choi, K.J. Kim, M.H. Bhuiya, J.-D. Nam, Transparent actuator made with few layer graphene electrode and dielectric elastomer, for variable focus lens, Applied Physics Letters 103(2) (2013) 023106.

[136] S. Rudykh, K. Bhattacharya, Snap-through actuation of thick-wall electroactive balloons, International Journal of Non-Linear Mechanics 47(2) (2012) 206-209.

[137] D.M. Haughton, R.W. Ogden, On the incremental equations in non-linear elasticity — II. Bifurcation of pressurized spherical shells, Journal of the Mechanics and Physics of Solids 26(2) (1978) 111-138.

[138] R. Ogden, Large deformation isotropic elasticity-on the correlation of theory and experiment for incompressible rubberlike solids, Proceedings of the Royal Society of London. A. Mathematical and Physical Sciences 326(1567) (1972) 565-584.

[139] A.M. van der Heijden, WT Koiter's elastic stability of solids and structures, Cambridge University Press Cambridge2009.

[140] F. Carpi, D. De Rossi, R. Kornbluh, R.E. Pelrine, P. Sommer-Larsen, Dielectric elastomers as electromechanical transducers: Fundamentals, materials, devices, models and applications of an emerging electroactive polymer technology, Elsevier2011.

[141] R. Kornbluh, Dielectric elastomer artificial muscle for actuation, sensing, generation, and intelligent structures, Materials Technology 19(4) (2004) 216-223.

[142] D. Liang, Z.-F. Lin, C.-C. Huang, W.-P. Shih, Tunable lens driven by dielectric elastomer actuator with ionic electrodes, IET Micro & Nano Letters 9(12) (2014) 869-873.

[143] G.-K. Lau, T.-G. La, L.-L. Shiau, A.W.Y. Tan, Challenges of using dielectric elastomer actuators to tune liquid lens, Proc. SPIE, 2014, p. 90561J.

[144] L.D. Landau, EM Lifshitz Electrodynamics of continuous media, Course of Theoretical Physics 8 (1960) 15.

[145] X. Liang, S. Cai, Shape bifurcation of a spherical dielectric elastomer balloon under the actions of internal pressure and electric voltage, Journal of Applied Mechanics 82(10) (2015) 101002.

[146] A. Gent, A new constitutive relation for rubber, Rubber chemistry and technology 69(1) (1996) 59-61.

[147] S. Wang, M. Decker, D.L. Henann, S.A. Chester, Modeling of dielectric viscoelastomers with application to electromechanical instabilities, Journal of the Mechanics and Physics of Solids 95 (2016) 213-229.

[148] D. Haughton, R. Ogden, On the incremental equations in non-linear elasticity—I. Membrane theory, Journal of the Mechanics and Physics of Solids 26(2) (1978) 93-110.

[149] J.-S. Plante, S. Dubowsky, Large-scale failure modes of dielectric elastomer actuators, International journal of solids and structures 43(25) (2006) 7727-7751.

[150] X. Zhao, Z. Suo, Theory of dielectric elastomers capable of giant deformation of actuation, Physical review letters 104(17) (2010) 178302.

[151] S.M. Ha, W. Yuan, Q. Pei, R. Pelrine, S. Stanford, Interpenetrating Polymer Networks for High - Performance Electroelastomer Artificial Muscles, Advanced Materials 18(7) (2006) 887-891.

[152] G. Kofod, The static actuation of dielectric elastomer actuators: how does pre-stretch improve actuation?, Journal of Physics D: Applied Physics 41(21) (2008) 215405.

[153] M. Wissler, E. Mazza, Modeling of a pre-strained circular actuator made of dielectric elastomers, Sensors and Actuators A: Physical 120(1) (2005) 184-192.

[154] J. Huang, T. Li, C. Chiang Foo, J. Zhu, D.R. Clarke, Z. Suo, Giant, voltage-actuated deformation of a dielectric elastomer under dead load, Applied Physics Letters 100(4) (2012) 041911.

[155] R. Pelrine, R. Kornbluh, Q. Pei, J. Joseph, High-speed electrically actuated elastomers with strain greater than 100%, Science 287(5454) (2000) 836-839.

[156] Y.-X. Xie, J.-C. Liu, Y. Fu, Bifurcation of a dielectric elastomer balloon under pressurized inflation and electric actuation, International Journal of Solids and Structures 78 (2016) 182-188.

[157] X. Zhao, Z. Suo, Method to analyze electromechanical stability of dielectric elastomers, Applied Physics Letters 91(6) (2007) 061921.

[158] A. Dorfmann, R. Ogden, Nonlinear electroelastostatics: incremental equations and stability, International Journal of Engineering Science 48(1) (2010) 1-14.

[159] S. Höhn, A.R. Honerkamp-Smith, P.A. Haas, P.K. Trong, R.E. Goldstein, Dynamics of a Volvox embryo turning itself inside out, Physical review letters 114(17) (2015) 178101.

[160] K.S. Freeman, G.A. Lewbart, W.P. Robarge, C.A. Harms, J.M. Law, M.K. Stoskopf, Characterization of eversion syndrome in captive Scyphomedusa jellyfish, American journal of veterinary research 70(9) (2009) 1087-1093.

[161] G. Lewbart, Invertebrate medicine, Wiley Online Library2006.

[162] T. Mizuno, Y. Takewa, H. Sumikura, K. Ohnuma, T. Moriwaki, M. Yamanami, T. Oie, E. Tatsumi, M. Uechi, Y. Nakayama, Preparation of an autologous heart valve with a stent (stent‐biovalve) using the stent eversion method, Journal of Biomedical Materials Research Part B: Applied Biomaterials 102(5) (2014) 1038-1045.

[163] R.C. Darling, P.S. Paty, D.M. Shah, B.B. Chang, R.P. Leather, Eversion endarterectomy of the internal carotid artery: technique and results in 449 procedures, Surgery 120(4) (1996) 635-640.

[164] D. Haughton, A. Orr, On the eversion of incompressible elastic cylinders, International journal of non-linear mechanics 30(2) (1995) 81-95.

[165] D. Haughton, A. Orr, On the eversion of compressible elastic cylinders, International journal of solids and structures 34(15) (1997) 1893-1914.

[166] M.S. Pour, Y. Fu, WKB method with repeated roots and its application to the buckling analysis of an everted cylindrical tube, SIAM Journal on Applied Mathematics 62(6) (2002) 1856-1871.

[167] O.H. Varga, Stress-strain behavior of elastic materials; selected problems of large deformations, (1966).

[168] P. Chadwick, E. Haddon, Inflation-extension and eversion of a tube of incompressible isotropic elastic material, IMA Journal of Applied Mathematics 10(2) (1972) 258-278.

[169] J. Ericksen, Inversion of a perfectly elastic spherical shell, ZAMM‐Journal of Applied Mathematics and Mechanics/Zeitschrift für Angewandte Mathematik und Mechanik 35(9‐10) (1955) 382-385.

[170] S.S. Antman, The eversion of thick spherical shells, Archive for Rational Mechanics and Analysis 70(2) (1979) 113-123.

[171] R.S. Rivlin, Large elastic deformations of isotropic materials. VI. Further results in the theory of torsion, shear and flexure, Philosophical Transactions of the Royal Society of London A: Mathematical, Physical and Engineering Sciences 242(845) (1949) 173-195.

[172] S. Baek, T. Pence, Inhomogeneous deformation of elastomer gels in equilibrium under saturated and unsaturated conditions, Journal of the Mechanics and Physics of Solids 59(3) (2011) 561-582.

[173] C. Truesdell, Rational thermodynamics: a course of lectures on selected topics, McGraw-Hill1969.

[174] L.R.G. Treloar, The physics of rubber elasticity, Oxford University Press, USA1975.

[175] D. Chen, J. Yoon, D. Chandra, A.J. Crosby, R.C. Hayward, Stimuli‐responsive buckling mechanics of polymer films, Journal of Polymer Science Part B: Polymer Physics 52(22) (2014) 1441-1461.

[176] B. Ng, W. Reid, An initial value method for eigenvalue problems using compound matrices, Journal of Computational Physics 30(1) (1979) 125-136.

[177] Q. Wang, X. Zhao, Creasing-wrinkling transition in elastomer films under electric fields, Physical Review E 88(4) (2013) 042403.

[178] S. Mora, T. Phou, J.-M. Fromental, Y. Pomeau, Gravity driven instability in elastic solid layers, Physical review letters 113(17) (2014) 178301.

[179] G.A. Houseman, P. Molnar, Gravitational (Rayleigh–Taylor) instability of a layer with non-linear viscosity and convective thinning of continental lithosphere, Geophysical Journal International 128(1) (1997) 125-150.

[180] J. Du, X. Chen, X. Liang, G. Zhang, J. Xu, L. He, Q. Zhan, X.-Q. Feng, S. Chien, C. Yang, Integrin activation and internalization on soft ECM as a mechanism of induction of stem cell differentiation by ECM elasticity, Proceedings of the National Academy of Sciences 108(23) (2011) 9466-9471.

[181] S. Cai, K. Bertoldi, H. Wang, Z. Suo, Osmotic collapse of a void in an elastomer: breathing, buckling and creasing, Soft Matter 6(22) (2010) 5770-5777.

[182] L. Jin, S. Cai, Z. Suo, Creases in soft tissues generated by growth, EPL (Europhysics Letters) 95(6) (2011) 64002.

[183] Y. Cao, J.W. Hutchinson, From wrinkles to creases in elastomers: the instability and imperfection-sensitivity of wrinkling, Proc. R. Soc. A, The Royal Society, 2012, pp. 94-115.